A COMPUTATIONAL APPROACH TO THE MECHANISM OF LIGHT-DRIVEN REACTIONS IN SOLUTION

Victor Miguel Fernández Alvarez

UNIVERSITAT ROVIRA i VIRGILI

A COMPUTATIONAL APPROACH TO THE MECHANISM OF LIGHT-DRIVEN REACTIONS IN SOLUTION

Victor Miguel Fernández Alvarez

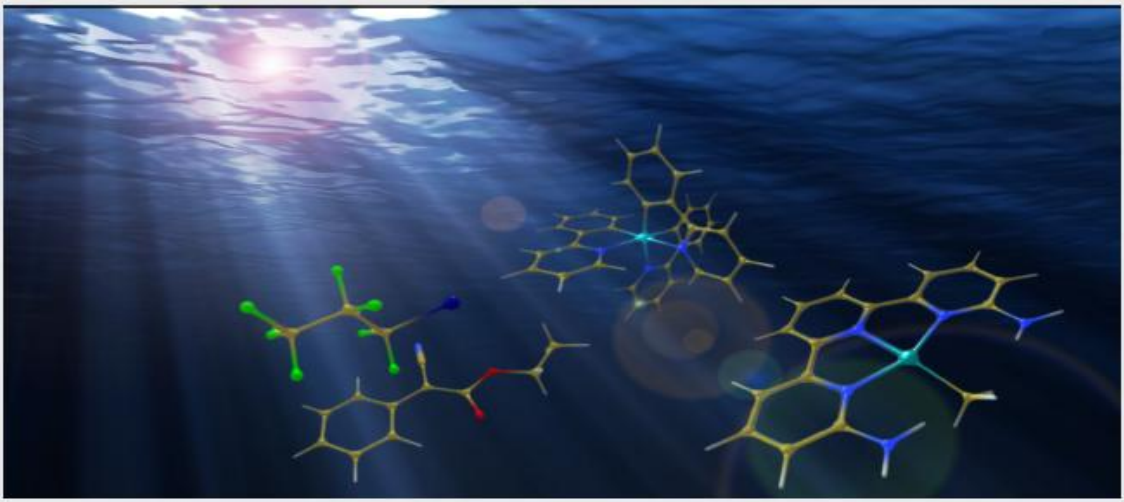

DOCTORAL THESIS

2017

UNIVERSITAT ROVIRA I VIRGILI
A COMPUTATIONAL APPROACH TO THE MECHANISM OF LIGHT-DRIVEN REACTIONS IN SOLUTION
Victor Miguel Fernández Alvarez

UNIVERSITAT ROVIRA I VIRGILI
A COMPUTATIONAL APPROACH TO THE MECHANISM OF LIGHT-DRIVEN REACTIONS IN SOLUTION
Victor Miguel Fernández Alvarez

Victor Miguel Fernández Alvarez

A COMPUTATIONAL APPROACH TO THE MECHANISM OF LIGHT-DRIVEN REACTIONS IN SOLUTION

DOCTORAL THESIS

Supervised by

Prof. Feliu Maseras

Institute of Chemical Research of Catalonia

UNIVERSITAT ROVIRA I VIRGILI

Tarragona

2017

UNIVERSITAT ROVIRA I VIRGILI
A COMPUTATIONAL APPROACH TO THE MECHANISM OF LIGHT-DRIVEN REACTIONS IN SOLUTION
Victor Miguel Fernández Alvarez

ICIQ - Institut Català d'Investigació Química
Avgda, Països Catalans 16,
43007 Tarragona (Spain)

Prof. Feliu Maseras, Group Leader at the Institute of Chemical Research of Catalonia,

I STATE that the present study, entitled "A Computational Approach to the Mechanism of Light-Driven Reactions in solution" presented by Victor Miguel Fernndez Alvarez for the award of the degree of Doctor, has been carried out under my supervision in my group at the Institute of Chemical Research of Catalonia and that it fulfils all the requirements to be eligible for the International Doctor Distinction.

Tarragona, January 23^{rd}, 2017

Doctoral Thesis Supervisor

Prof. Feliu Maseras

UNIVERSITAT ROVIRA I VIRGILI
A COMPUTATIONAL APPROACH TO THE MECHANISM OF LIGHT-DRIVEN REACTIONS IN SOLUTION
Victor Miguel Fernández Alvarez

The elaboration of this Doctoral Thesis would not have been possible without the help of many. First and foremost I would like to thank my supervisor Feliu Maseras, for providing invaluable support and help during these 4 years. He placed his trust in me and accepted me into his group well before he had any good reason to do so. Under his supervision I was able to work with freedom and independence, and yet he was never too busy for a discussion, and was always willing to offer a healthy combination of motivation and pragmatism.

My time at ICIQ was a wonderful experience, and that is mostly due to the people with whom I shared it. I would like to thank Dr. Maria Besora for her help on countless occasions, in particular for showing me how to look at problems with perspective rather than panic. Thanks to Prof. Núria Lopez and Prof. Carles Bo for their advice and kindness, and special thanks to Núria Vendrell. I cannot overstate how many times she helped me with everything involving administrative issues, and for that I am very grateful.

I also want to salute all the colleagues and friends I was fortunate enough to meet at ICIQ during my PhD years. I received tremendous help and advice from many of them, and I am thankful for the good times spent together, from my lunchmates to my ping pong partners, to the Geoguessr crew and their unrealistic record scores. I also want to thank the close friends I made in Tarragona, Mariano and Anahid for their support and for sharing this adventure with me.

I want to extend my thanks to Prof. Keiji Morokuma for his hospitality during my stay in his group in the summer of 2014. During this time I learned many things and got to meet great people. In particular I would like to thank Dr. WMC Sameera, for helping me with virtually everything while I was there, and for sharing good

times during my stay. In addition, I would like to thank the other members of the group at FIFC for making my stay even more enjoyable, with ramen days and strange yet fun Japanese visual metal concerts.

I would also like to thank Prof. John E. McGrady, for allowing me to visit his group in 2015, and for being an excellent host. I greatly enjoyed the experience of working in a different field despite my absolute lack of experience on it. While in the Oxford group I met some fantastic folks, whom I would like to thank for their support and hospitality. In particular I would like to thank Dr. Vaida Arciăuskaitė and Stephan Vogelius for their friendship and hospitality and for kayaking with me in the Thames.

Finally, I want to thank those closest to me. My family for all the support, encouragement and sacrifices that allowed me to be where I am now. To say that I would not be here without their help would be a gross understatement. And of course my partner for making every setback endurable, every problem manageable, and every success worth the trouble.

UNIVERSITAT ROVIRA I VIRGILI
A COMPUTATIONAL APPROACH TO THE MECHANISM OF LIGHT-DRIVEN REACTIONS IN SOLUTION
Victor Miguel Fernández Alvarez

Contents

List of Figures

List of Tables

UNIVERSITAT ROVIRA I VIRGILI
A COMPUTATIONAL APPROACH TO THE MECHANISM OF LIGHT-DRIVEN REACTIONS IN SOLUTION
Victor Miguel Fernández Alvarez

Abstract

Recent years have witnessed a renaissance of light-driven approaches to synthetic chemistry. The need for more sustainable strategies and better atom economy for chemical production, together with impressive advances in the field of solar energy, has prompted synthetic chemists to study new and more efficient photochemical transformations for synthetic purposes. In addition to new direct photoactivated reactions, the use of polypyridyl Ru or Ir complexes has been successfully imported from solar energy research into the field of photocatalysis with a plethora of examples available in the literature.

With the rise of new synthetic strategies, comes the need for mechanistic studies which can help rationalize the outcomes and thus enable improvements in the design of future reaction schemes. In this regard, computational chemistry has proven time and again to be a powerful tool to gain mechanistic information to support experimental evidence. In particular, the computation of reaction pathways using Density Functional Theory (DFT) methods is an established method for the study of mechanisms in solution. However, there has been a notable absence in the literature of computational studies on the mechanism of photoactivated reactions of synthetic interest, and especially of photocatalyzed reactions.

In this thesis we set out to study the reaction mechanism of several high impact reactions activated by light irradiation, whether directly or via a photocatalyst. To this end we used a combination

of DFT methods, kinetic models and time-dependent DFT calculations. A background for this work is found in chapter 1, where we present an overview of the progress that has been made in the area, including the remarkably few DFT-based studies reported, whereas chapter 2 describes the theoretical tools used throughout the thesis.

Chapter 3 covers photoactivated reactions studied in collaboration with synthetic experimental groups, and is divided in two parts. In Part I, the perfluoroalkylation of arylacetates was studied. The experimental quantum yield was rationalized, and the origin of selectivity was elucidated. In addition, the different reactivity observed for similar substrates was found to depend on steric repulsion from the electron withdrawing groups.

In Part II of the same chapter, the insertion of dioxygen into the Pt(II)-methyl bond was studied. The generation of singlet oxygen was elucidated, as well as the formation of the methylperoxo product. In addition, the different reactivity of disubstituted terpyridine Pt complexes towards oxygen insertion was found to depend on the substituents in the ligand, and their ability to enable methyl migration versus deactivation of the excited state.

In Chapter 4 we studied two reactions photocatalyzed by polypyridyl iridium complexes. Part I describes the study of the C-H arylation of amines, where the different yields of similar substrates were reproduced and rationalized using kinetic models. Reactivity was found to depend on the competition between productive electron transfer and back electron transfer to restore reactants. Moreover, the counterion of the base was found to play a part in the arylation of substrates with low reduction potential.

Finally, in Part II of chapter 4 the trichloromethylation of acylpyridines was studied. Enantiomeric excess was reproduced and

rationalized on the basis of steric repulsions from the chiral ligand, which only affect the formation of one enantiomer. In addition, several hypothetical catalysts were sampled in order to determine the optimal enantiomeric excess, as well as their behavior with different substrates.

Chapter 1

Introduction

The Synthetic Value of Light

For over 200 years, synthetic chemists have tried to efficiently harvest sunlight as a source of energy for the controlled production of valuable chemicals. The rationale behind this quest is that compared to thermal methods, photochemical reactions allow for the generation of kinetically and/or thermodynamically disfavoured products.[1] In addition, this pursuit has been partially motivated by the realisation that the sun is effectively an inexhaustible source of energy.[2] The advantage of using free solar energy constitutes one reason why synthetic photochemistry is often considered a *green* and sustainable methodology. Moreover, strategies involving artificial light sources are also considered sustainable. For instance, light absorption localized within a chromophore can be controlled with the wavelength, and terminated safely by simply turning off the light

source.

Despite its apparent advantages, light-driven synthesis was an underdeveloped field for many decades for several reasons. Many organic molecules require high energy UV photons to reach the excited state which are not abundant in sunlight once it penetrates the atmosphere. Sunlight at the surface is roughly only 3-5% ultraviolet.[3] Furthermore, the use of strong light has a number of undesired consequences. Not only is it harmful to humans, but it can also damage reactor materials, dramatically increasing the cost. Another problem is the quantum efficiency of photochemical reactions, as it is heavily affected by dominant photophysical deactivation pathways.[4] These can be fluorescence, phosphorescence, or nonradiative internal conversion, and all restore the ground state original species. These processes are commonly summarized in a Jablonski diagram (Figure 1.1).[5]

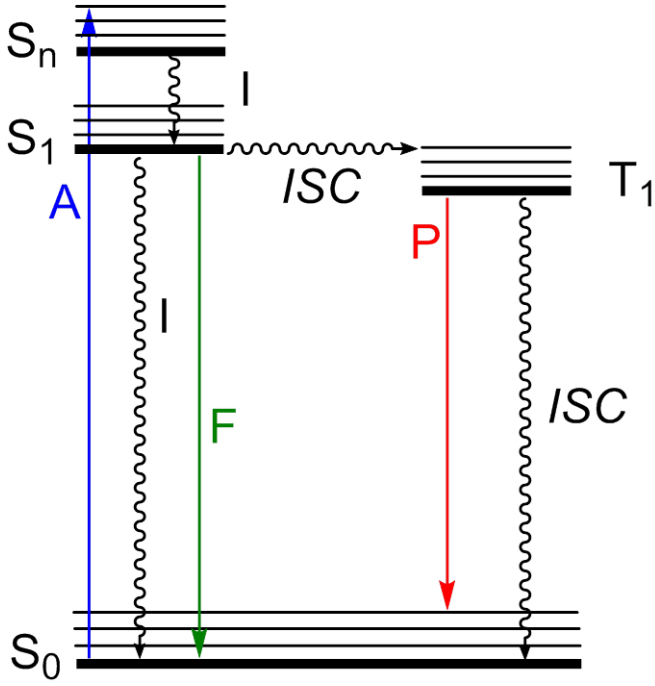

Figure 1.1: Typical Jablonski Diagram.

Normally, absorption (A) of a photon from the singlet ground state S_0 to the S_n state relaxes via internal conversion (I) to the S_1 state. Internal conversion then restores the ground state without emitting a photon, and fluorescence (F) emits a lower energy photon than the one absorbed. In addition, intersystem crossing (ISC) can lead to the triplet state (T_1) which can emit a photon to display phosphorescence (P) or undergo a subsequent ISC to restore the ground state. Normally, only T_1 has a sufficient lifetime to efficiently undergo chemical transformations, thus all other photophysical processes effectively reduce reactivity. In addition to photophysical deactivation, prolonged exposure to high energy light can degrade photochemically unstable products, lowering the yield and leading to the generation of undesired species.

The Advent of Photocatalysis

To overcome the limitations of photochemical synthesis, organic chemists took inspiration from the use of transition metal complexes to transform solar energy into electrochemical potential. They correctly rationalized that these complexes could be used to catalyze useful and unique reactions in organic synthesis. In particular, polypyridyl metal complexes like $Ru(ppy)_3^{2+}$ had been the main subject of extensive research for the development of a wide range of solar energy conversion strategies, and to understand fundamental aspects of excited state dynamics and electronic structure.[6, 7]

The recent surge in interest for photocatalytic strategies was sparked by two simultaneous publications in 2008, both using $Ru(ppy)_3^{2+}$ as the photocatalyst.[8] Yoon *et al.* reported the [2+2] cycloaddition of bis(enone) activated by visible light.[9] Previously reported strategies for this reaction using copper[10] and cobalt[11] catalysts had found that activation of the cycloaddition was initiated by one-electron reduction of the enone, evidencing the formation of a radical anionic enone intermediate during the process.[12] Thus, the opportunity of an effective photocatalytic strategy was apparent. Figure 1.2 shows the general scheme of the reaction.

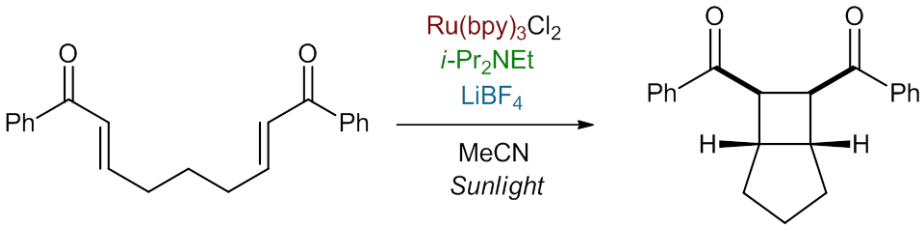

Figure 1.2: $Ru(bpy)_3^{2+}$ catalyzed cycloaddition of bis(enone).

Several features are interesting about this pioneering method. The reaction requires the presence of a sacrificial reducing agent (*i*-Pr_2NEt). This indicates that the reduction potential of $Ru(bpy)_3^{2+*}$ is not high enough to transfer an electron to the enone, thus the electron donor is effectively $Ru(bpy)_3^{+}$ after photoinduced electron transfer from the sacrificial reductant. In addition, the reaction only proceeds in the presence of an additive ($LiBF_4$), which acts as a Lewis acid and activates one-electron reduction of the enone. This particular feature bears some relevance in one of the mechanistic studies presented in this dissertation. Yet despite the necessity for additional species in the reaction, this light-driven strategy proved highly efficient reaching 94% yield in one hour under sunlight, evidencing the great potential of photocatalysis in organic synthesis.

The second work was published by MacMillan *et al.* and consisted in combining photocatalysis with asymmetric organocatalysis.[13] The study was inspired by the use of bulky amine catalysts to enable enantioselective α-alkylation of aldehides.[14, 15] This reaction involves the formation of a π-rich enamine intermediate which can attack an electron-deficient partner and form a C-C bond in a two-electron pathway. The rational for coupling these two fields was to imitate photoredox enzymatic catalysis, which replaces high energy two-electron barriers with low energy one-electron steps.[16] The authors used $Ru(bpy)_3^{2+}$ as the photocatalyst which can transfer an electron to the C-Br bond and generate bromide and a terminal alkyl radical, that can easily form a one-electron C-C bond with the enamine intermediate.

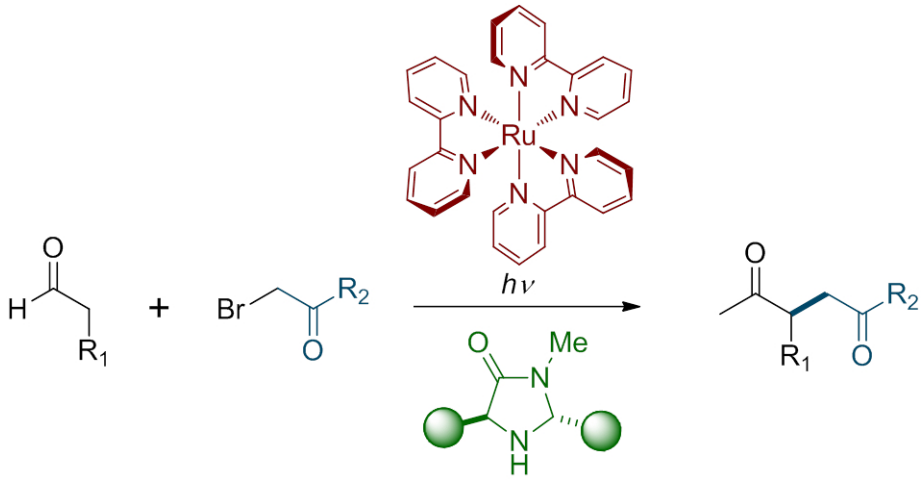

Figure 1.3: $Ru(bpy)_3^{2+}$ catalyzed asymmmetric alkylation of aldehides.

Like the [2+2] cycloaddition discussed above, this alkylation strategy required the formation of the reduced $Ru(bpy)_3^{2+}$ in order to generate the aklyl radical. However, in this setup there is no sacrificial reductant. Instead, the alkylated enamine radical acts as the reducing agent, closing the redox cycle. The formation of the alkyl radical precludes the alkylation of the enamine. Thus, the reaction requires a minimal fraction of the photocatalyst to be reduced by an external agent. In addition, this publication applied DFT calculations to rationalize the high enantioselectivity provided by the amine organocatalyst (90-96% ee), where the enamine intermediate was found to be formed selectively in an orientation that facilitates enantioselective C-C bond formation.

In the following years, a wide range of metal complexes have been studied as photocatalysts for applications in synthesis, the vast majority of which are ruthenium and iridium complexes. The most intensely studied photocatalyst for both synthetic and light-

harvesting purposes has been $Ru(ppy)_3^{2+}$ (bpy = 2,2-bipyridine),[17] with $Ir(ppy)_3$ being a close second.[18] Both of these complexes exhibit broad absorption bands in the visible range that result in long-lived triplet states. The photogenerated triplet form of these complexes, as is the case for most photocatalysts, has higher oxidation and reduction potentials than their ground state counterparts, making them viable oxidants as well as reductants. Thus, the most frequent use of these species for synthetic purposes has been to initiate chemical processes by single electron transfer (SET) to an organic molecule, driving one electron reduction or oxidation of electron-deficient or electron-rich substrates, respectively. The type of photocatalysis which involves photoinduced electron transfer (PET) is normally referred to as photoredox catalysis.

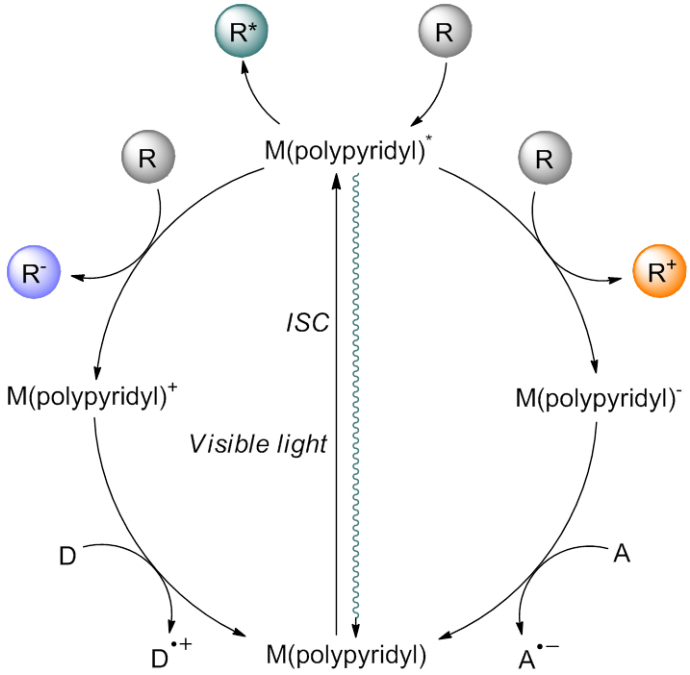

Figure 1.4: Different pathways of photocatalysis.

Alternatively to PET, a photocatalyst can directly transfer energy to a suitable organic substrate. As with direct light absorption, the resulting excited substrate has a completely different chemical behavior than its ground state form and can engage in otherwise non-viable reactions. Figure 1.4 shows the different possible uses for a photocatalyst. These are reductive quenching (orange), oxidative quenching (purple), and energy transfer (green). A photoredox process is often restarted by a sacrificial electron donor (D) or acceptor (A) to the original ground state. The most intuitive mechanism for energy transfer would be absorption by the organic substrate of a photon emitted by the excited complex. However, energy transfer rarely takes place via radiative pathways.[17] The two most common non-radiative transfer processes are through-space (Förster) or through-bond (Dexter) mechanisms (figure 1.5).[19, 20]

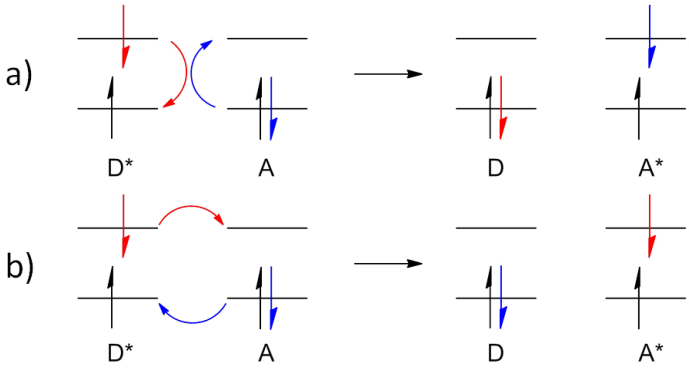

Figure 1.5: Förster (a) and Dexter (b) mechanisms of energy transfer.

Förster transfer takes place via coupling of the transition dipole moments of the excited catalyst and the ground state substrate, which can take place through distances as far as 100 Å.[21] On the other hand, the Dexter mechanism consists basically of two simulta-

neous electron transfer and requires orbital overlap between donor and acceptor. Energy transfer strategies however, are relatively rare compared to photoredox processes and will not be discussed further in this work.

Computational Mechanistic studies in Photocatalysis

The recent surge of light-driven synthetic strategies has spawned a wide array of new previously unattainable reactions.[2] Therefore, considerable experimental effort has been devoted to elucidating the mechanisms of such new transformations.[22, 23] However, despite the enormous synthetic potential displayed by these methods, there is a severe scarceness of computational mechanistic studies available in this field. This is rather remarkable, considering computational methods, particularly Density Functional Theory (DFT) methods, are an established and useful tool for the elucidation reaction mechanisms in solution.[24, 25, 26] DFT calculations have been used for specific purposes in mechanistic studies on photocatalysis,[22, 27, 28, 29] but rarely for the calculation of a complete reaction mechanism. This is in part justified by the intrinsic complexity of the electronic excited states involved. A proper quantum-mechanical description of a process in the excited state requires ab initio multiconfigurational methods,[30] which become too computationally demanding for most systems of practical use. In fact, to the best of our knowledge no DFT mechanistic studies on photocatalysis were published by early 2013, at the start of the work presented in this thesis. Since then however, some noteworthy

examples haven been reported.

In 2014, Manners *et al.* reported the iron-catalyzed light-driven dehydrogenation of amine boranes.[31] The authors found that complexes $[CpFe(CO)_2]_2$ and $CpFe(CO)_2I$ could catalyze the dehydrocoupling/dehydrogenation of $Me_2NH{\cdot}BH_3$ to generate $[Me_2N{\cdot}BH_2]_2$ under light irradiation in MeCN. Experimental analysis indicated that $[CpFe(CO)_2]_2$ becomes $Cp_2Fe_2(CO)_3(MeCN)$ under irradiation, which in turn forms Fe nanoparticles that act as heterogeneous catalyst for dehydrogenation via a $Me_2N{=}BH_2$ intermediate. On the other hand, $CpFe(CO)_2I$ proceeds through a different pathway which was studied both experimentally and by DFT methods. Irradiation of $CpFe(CO)_2I$ results in the photodissociation of either iodide or CO, followed by coordination of $Me_2NH{\cdot}BH_3$ and metal-mediated formation of a linear intermediate $Me_2NHBH_2NMe_2BH_3$. A second metal-mediated step releases the cyclic product. Figure 1.6 shows the two pathways studied in this work.

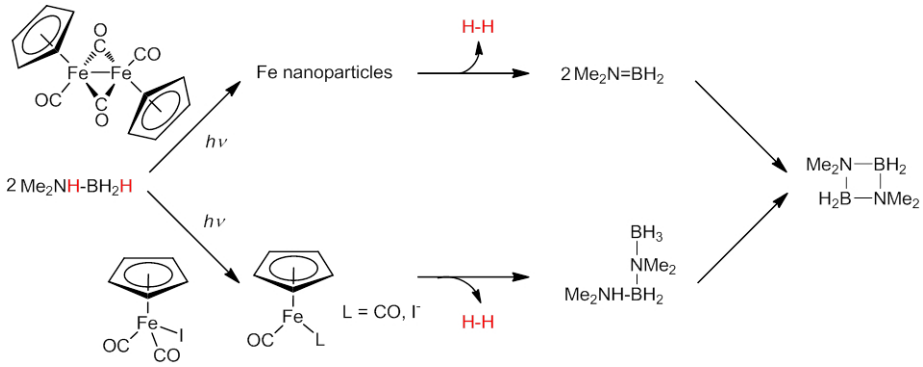

Figure 1.6: Fe-catalyzed dehydrogenation of amine boranes.

The report includes the computation of a free energy profile of plausible minima involved in the pathway catalyzed by $CpFe(CO)_2I$, following photodissociation of a ligand from the catalyst. Although

the bulk of the mechanistic investigation was done experimentally, the use of ground state DFT to build a free energy profile and obtain useful information on a photoactivated process evidenced the value of computational insights beyond the mere computation of absorption spectra or redox potential calculations.

A fully computational mechanistic study on a photoactivated process using DFT methods was recently reported by Ganglong *et al.*[32] The authors studied the mechanism for the photooxidation of $Ru(bpy)_2(TMBiimH_2)$ (where $TMBiimH_2$ = 4,5,4,5-tetramethyl-2,2-biimidazole). Figure 1.7 shows the mechanism calculated in this report.

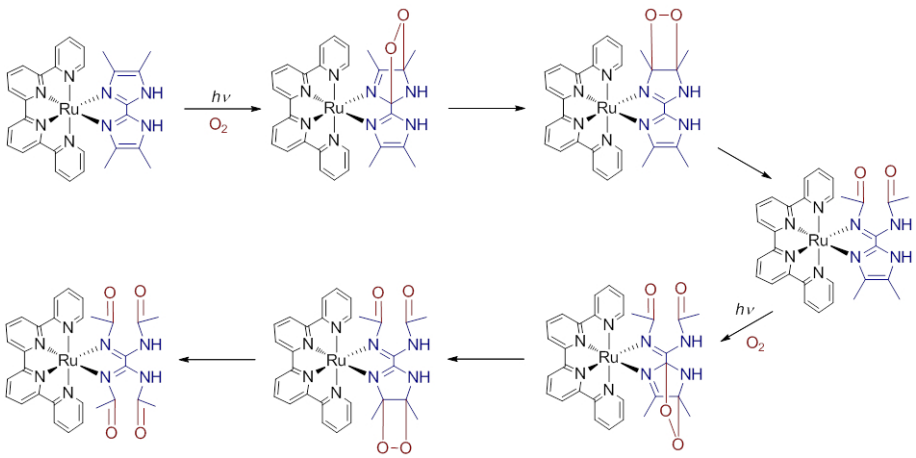

Figure 1.7: Reaction mechanism for photooxidation of $Ru(bpy)_2(TMBiimH_2)$.

The authors propose that molecular oxygen is transformed into singlet oxygen by energy transfer from the triplet excited state complex. This claim is made on the basis that energy transfer from the excited triplet Ru complex to triplet molecular dioxygen to afford ground state catalyst and singlet oxygen is thermodynamically fa-

vored. In addition, calculations support a simultaneous formation of both carbonyl groups rather than the stepwise pathway predicted experimentally.

Photoredox catalyzed reactions generate organic radicals, sometimes simultaneously,[2] which is an issue DFT-focused computational chemists have generally avoided. The reason is that combination of free radicals to form a σ bond cannot be properly described with a single determinant description like the one provided by DFT methods. This point will be elaborated in more detail in Chapter 2. However, useful information can still be obtained from DFT calculations on open-shell systems. Hansen *et al.*[33] reported a thorough computational study on site-selectivity in photocatalyzed C-H functionalization. They used a combination of Natural Bond Orbital (NBO), Quantum Theory of Atoms in Molecules (QTAIM), and frontier orbital analysis to qualitatively evaluate the most favored sites for selective methylation by PET-generated methyl radical. In addition, they computed the free energy profile for the photocatalyzed methylation of industrially relevant molecules. Figure 1.8 shows the general scheme of the reaction studied.

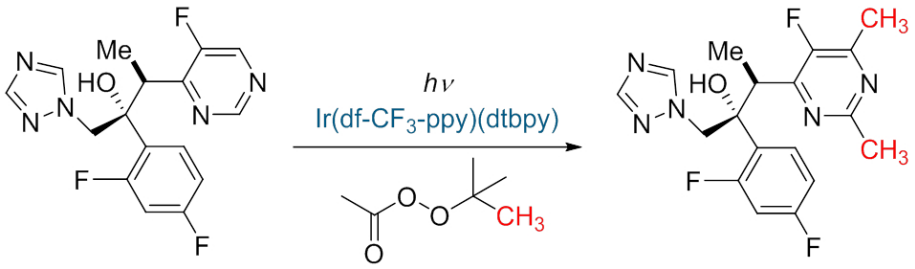

Figure 1.8: Ir-photocatalyzed C-H methylation of heteroatomic voriconazole.

The authors studied the PET from the Ir(df-CF_3-ppy)(dtbpy)$^+$

catalyst (where dtbpyH = 4,4-bis(1,1-dimethylethyl)-2,2-bipyridine and df-CF_3-ppyH = 3,5-difluoro-2-[5-(trifluoromethyl)-2-phenylpyridine) to the alkylperoxyacetate that results in the generation of methyl radical. They studied the absorption spectrum of an optimized reaction complex in which alkylperoxyacetate was in the vicinity of the photocatalyst via time-dependent DFT (TD-DFT) calculations, which showed a small contribution to spin density from the alkylperoxyacetate, suggesting electron transfer from the excited state complex to the radical generator. Remarkably, this work constitutes an attempt to model single electron transfer from a photocatalyst using strictly DFT methods, as part of a mechanistic study.

In 2016, Xiao *et al.* published a thorough experimental and computational investigation into the $Ru(bpy)_3^{2+}$-catalyzed N-radical cascade reaction of hydrazones via oxidative deprotonation.[34] The reaction takes place under visible light irradiation and proceeds selectively towards oxidative deprotonation only in the presence of TEMPO mediation. DFT methods were used to elucidate the role of TEMPO in the formation of the desired product through a free energy profile in which radical combination was considered a process with a negligible barrier.

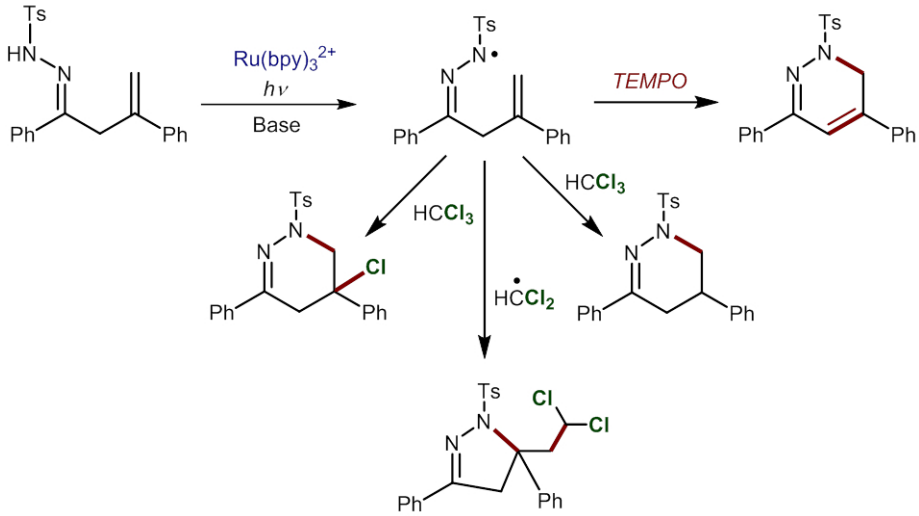

Figure 1.9: Ru-catalyzed N-radical cascade reaction of hydrazones.

The authors found that without TEMPO as the radical mediator, the photogenerated hydrazone radical could be chlorinated or protonated to yield undesired products. In addition radical combination could take place between oxidized hydrazone and dichloromethyl radical formed oxidative quenching by chloroform to restore the photocatalyst.

One of the most promising uses for photoredox catalysis is to enable one electron reduction of metal catalysts.[35, 36] This dual catalysis approach enables a metal catalyst to reach the target oxidation state necessary to effectively activate a chemical process.[37] As for dual catalysis strategies studied computationally, Kozlowski *et al.* published a fully DFT-based mechanistic investigation into the Ni-catalyzed cross-coupling of photoredox generated radicals.[38] The authors found that addition of the photogenerated radical can take place in different stages of the cycle to Ni(0) or Ni(II), and both pathways converge to the same Ni(III) intermediate. This is followed

by irreversible reductive elimination to yield the cross-coupling product. Figure 1.10 shows the two possible reaction mechanisms studied in this work.

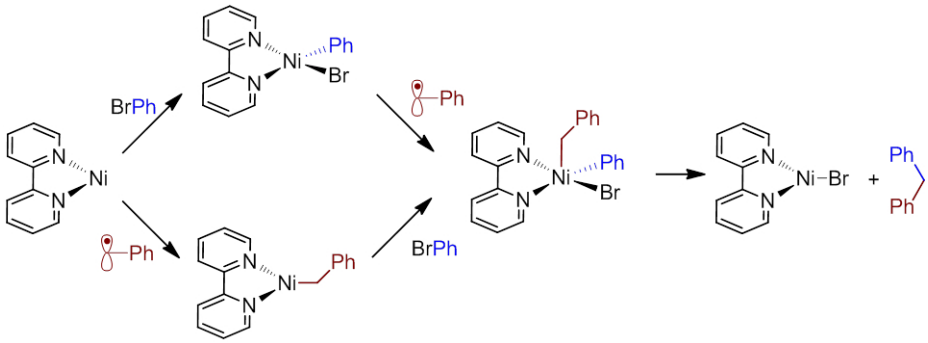

Figure 1.10: Ni-catalyzed cross-coupling of photoredox generated radicals.

In a purely thermal reaction, oxidative addition of phenyl bromide would take place after the barrierless addition of the benzyl radical. However, benzyl radical is produced photochemically and is present in a much lower concentration than phenyl bromide. Also, the barrier for oxidative addition is not particularly high (18.4 kcal.mol^{-1}). Thus, a simple barrier comparison would fail to take into account the large difference in concentration between benzyl radical and phenyl bromide, hence the authors leave both options open.

Objectives

With the recent renaissance of interest in visible light as the energy source for the efficient and selective promotion of chemical transformations, the need for computational mechanistic insights is apparent. In this computational thesis we set out to study the reaction mechanism of new relevant processes driven by visible light to understand the factors that affect reactivity, selectivity and efficiency in light-driven processes of synthetic relevance. By doing so, we hope to contribute to future efforts not only in understanding the important details of these reactions, but also in the design of more efficient strategies in terms of atom and energy economy, and of sustainability in general.

In particular, we studied the mechanism of four photoactivated reactions. These studies are divided in two groups. The first group consists of processes in which visible light directly activates the reactants without the presence of a photosenzitizer. These projects were carried out in collaboration with experimental synthetic groups and are presented in Chapter 3. The second group involves reactions initiated by photoredox catalysis, in which a cyclometallated iridium photocatalyst generates organic radicals via single electron transfer. The study of these reactions is covered in Chapter 4.

In addition to fully elucidating the mechanistic factors governing these processes, we tackled specific aspects of photoactivated homogeneous reactions that are challenging and often avoided by computational chemists, such as outer-sphere electron transfer and the comparison of pathways involving concentrations differing by several orders of magnitude.

Chapter 2

Theory

Electronic Structure and Energy Evaluation

A myriad of theoretical techniques have been developed to calculate properties of molecular systems. Most of them have as a central purpose the estimation of the relative energy of a given chemical structure. When addressing a particular case, the choice of the method is crucial, as increasing accuracy generally involves increasing computational cost (*i.e.*, machine time necessary to obtain the desired information). Thus, a balance is required between how accurate the result has to be, and how long it will take for the calculation to finish. Generally, the best method is the one that provides results accurate enough to be useful, in the least amount of time.

In the case of reactions in homogeneous phase, the most widely

used strategy to obtain computational insights on the mechanism is the comparison of Gibbs free energies obtained using Density Functional Theory (DFT) methods. There are several reviews and books describing in detail the derivation and construction of DFT methods,[39] and since the work presented in this thesis involves exclusively the application of these methods to address chemistry problems, only an overview and brief description of the method will be presented.

The grounds of DFT were set by Hohenberg, Kohn, and Sham in the mid 1960s.[40, 41] The theory states that there is an exact and unique functional ($F[\rho(\mathbf{r})]$) that relates the ground state electron density of any molecular system ($\rho(\mathbf{r})$) to the ground state energy. This functional can be written as the sum of all contributions to the energy, as shown in equation 2.1.

$$E[\rho(\mathbf{r})] = T_s[\rho(\mathbf{r})] + J[\rho(\mathbf{r})] + E_{XC}[\rho(\mathbf{r})] + E_{Ne}[\rho(\mathbf{r})] \tag{2.1}$$

where $T_s[\rho(\mathbf{r})]$ is the kinetic energy of the electrons in an isoelectronic noninteracting system, $J[\rho(\mathbf{r})]$ is the classical part of the Coulomb electron-electron repulsion, $E_{Ne}[\rho(\mathbf{r})]$ is the interaction between electrons and nuclei, and $E_{XC}[\rho(\mathbf{r})]$ is called the exchange-correlation energy, and includes quantum mechanical parts of the potential energy (self-interaction correction, exchange and correlation holes) and part of the kinetic energy not covered in the $T_s[\rho(\mathbf{r})]$ term.[39]

The exact form of $E_{XC}[\rho(\mathbf{r})]$ however, is unknown. This implies

that we rely on approximations to the exact $E_{XC}[\rho(\mathbf{r})]$ for all DFT calculations. Such approximations to the exchange-correlation part of the functional (ν_{XC}) can be classified by the strategy employed in their construction. The simplest approximation to ν_{XC} is the Local Density Approximation (LDA) and as its name indicates, relies only on the electron density $\rho(\mathbf{r})$ at each point in space. A much better approach is to include the gradient of the density ($\nabla\rho(\mathbf{r})$) at each point to the form of the approximate ν_{XC}. This strategy is referred to as Generalized Gradient Approximation (GGA).

Since ν_{XC} is responsible for exchange effects and they are usually much larger than their correlation counterparts, one strategy for approximate functionals was to include a portion of Hartree Fock (HF) exchange into GGA functionals. The inclusion of HF exchange can correct some of the self-exchange present in GGA functionals. Strategies that include partial (or total) inclusion of HF exchange into the GGA approximation are called hybrid functionals.

One additional improvement incorporated recently to approximate ν_{XC} is the inclusion of dispersion interactions. These interactions require a description of correlation far away from the nuclei at vanishing density, which make it difficult to model correctly. A partial introduction of dispersion is accomplished through parameterization. Notably, the M06 suit of functionals by Truhlar et al.[42] have been heavily parameterized to account for dispersion interactions. Particularly, the M06 functional has been used in some of the work presented in this thesis. This method is a meta-GGA (i.e. also includes the spin kinetic energy density $\nabla^2(\rho)$ in ν_{XC}) hybrid functional that has been designed for reactivity in organometallic systems.

Another alternative for the description of dispersion corrections

is to use the empirical Becke-Johnson equation damping functions (equation 2.2).[43]

$$E_D = -\sum ij f_{damp} \cdot \left(\frac{C_{6,ij}}{R_{ij}^6} + \frac{C_{8,ij}}{R_{ij}^8} + \frac{C_{10,ij}}{R_{ij}^{10}} + ... \right) \tag{2.2}$$

where f_{damp} is a dumping function that keeps dispersion interactions at long and middle range, and frequently only the first term is used by averaging atomic C_6 parameters. This description can easily be added to any DFT calculation.[44, 45]

One of the difficulties of designing a good functional is the description of interactions at long range. Corrections to the density description in LDA (GGA, meta-GGA) remain local, despite frequently being labelled as non-local because they are based on the localized model exchange-correlation holes. The exact exchange-correlation hole is fully non-local however. This becomes a problem in the asymptotic region of molecular systems, where self-interaction error causes the decay in ν_{XC} to be exponential rather than $-1/r$. As a consequence, TD-DFT calculations involving charge-transfer states fail miserably, especially those involving separated molecules.[46] In order to overcome this limitation, strategies to correct the long-range decay error have been designed.[47, 48]. In some of the work presented in this thesis, the ω-B97x-D long-range corrected functional was used as it also includes damped dispersion corrections.

Continuum Solvation Model

The relative energy of chemical species, and consequently their reactivities, are greatly affected by the medium. Therefore, an adequate description of solvent interactions is crucial for the study of reaction mechanisms in solution. The addition of explicit solvent models quickly becomes too computationally demanding, not only as the system under study becomes too large, but also because the presence of many different conformations means finding a minimum is a considerable challenge.

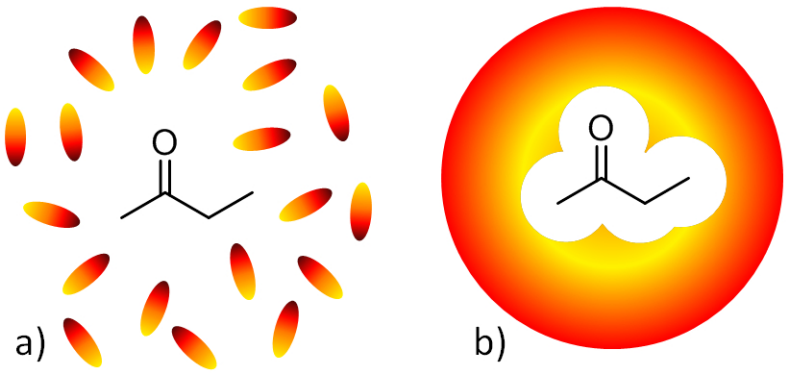

Figure 2.1: Representation of a discrete solvent (a) and a continuum solvent model (b).

The standard approach to avoid dealing with discrete solvent molecules is to consider the solvent a dielectric continuous medium that represents solvent dipole moment-induced polarity. This strategy is called the Polarizable Continuum Method (PCM).[49, 50] In a PCM approach, the molecular system is placed in a cavity surrounded by a field with the dielectric constant of the real solvent. Figure 2.1 shows a representation of the continuum solvent model.

The shape of the cavity typically consists of interlocked spheres centered around the outer nuclei of the molecular system. To obtain the energy in solution, the KS-energy of the molecular system is calculated in the presence of the solvent field, which in turn modifies the properties of the field. This process is repeated iteratively until both the field and the molecular system remain unchanged. The iterative process is referred to as Self-Consistent Reaction Field (SCRF). This treatment is usually applied by solving the non-homogeneous Poisson equation for electrostatics by means of the Integral-Equation-Formalism (IEF-PCM).[51, 52]

In order to account for more than just electrostatic contribution covered in the IEF-PCM formalism, other methods have been developed to include other interactions. Among them, the SMD model (the D stands for Dispersion, and SM for Solvation Model) has been designed and parameterized to describe dispersion interactions between the molecular system and the first layer of solvent molecules.[53] As a result, this approach causes greater distortion of the geometry than IEF-PCM. On the other hand, since SMD has been parameterized to reproduce solvation energies rather than geometries, there is no guarantee that geometries obtained in SMD are more accurate than those optimized in IEF-PCM.

ONIOM Partition

Sometimes the size of a system becomes too computationally demanding for a full DFT calculation. However, computationally cheaper methods like force field may be insufficient for the description of complex systems and are unable to describe the formation

or breakup of bonds, making the inadequate for simulating chemical reactions. Fortunately, for such cases there are methods that allow the computation of a system at two or more different levels of theory. The region that requires a high level description can be calculated at a higher level than the rest of the system. This approach is more accurate than using a model system that sacrifices all interactions from the surroundings.[54, 55] To this end, many quantum mechanics / molecular mechanics (QM/MM) strategies have been developed.[56, 57, 58] In a nutshell, in QM/MM approaches a portion of the molecule is described using Molecular Mechanics, while the rest is assigned to a more demanding method. Among these strategies is the ONIOM method,[59] which is the QM/MM strategy used in this thesis. The ONIOM partition is an established method which has been successfully applied to study both reactivity and system properties.[60, 61, 62, 63] In the ONIOM approach, the real system is partitioned into two fragments. The first fragment consists of the atoms composing the most important part of the system under study, and this fragment is described at the QM level. The rest of the system is described at the MM level. Equation 2.3 shows the scheme of the partition between high and low level within the ONIOM approach:

$$E_{tot}(QM/MM) = E_{MM}(Real) + E_{QM}(Model) - E_{MM}(Model) \tag{2.3}$$

where the subscripts refer to the level of theory applied, and the parenthesis refer to the region of the system being described. Figure

2.2 shows the ONIOM partition scheme represented as spheres.

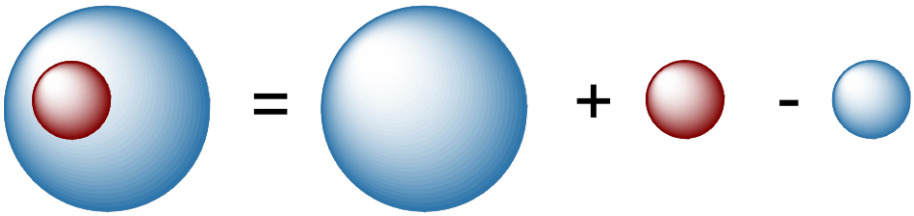

Figure 2.2: Representation of the ONIOM partition scheme.

The ONIOM scheme indicates that the entire system is calculated exclusively at the MM level, and only the model system is calculated at the computationally expensive level. One consequence of this is that all interactions that involve the outside system (including those that describe interactions between the model system and the outside part) are described at the MM level, which is particularly important for non-covalent interactions such as van der Waals forces. Once the partition is defined, any fragment in the outer layer that is bonded to the model system is replaced by a hydrogen in the QM calculation. Therefore, the layers are often divided across a single C-C bond to avoid large errors in the partition.

Light Absorption and Excited States

DFT is a ground-state theory, which means it does not provide information on the excited states reached upon absorption of a photon. In fact, the photophysical and photochemical processes that result from electronic excitations can only be properly described using high level wavefunction-based methods.[64, 65] However, as mentioned in Chapter 1 these methods become too computationally

demanding for most systems of interest. Such a limitation constitutes a major challenge for mechanistic studies on photoactivated reactions, as the efficiency of light-driven reactions depends strongly on the photochemical properties of the chromophores involved. Fortunately, there are computationally affordable tools that can provide reasonably accurate information on vertical one-electron excitations.

By far the most widely used method for the computation of excited states in molecular systems is Time-Dependent DFT (TD-DFT).[66, 67] This approach to excited states is based on the Runge-Gross (RG) theorem.[68] which is the time-dependent analogue to the Hohenberg-Kohn theorem. In this sense, the RG theorem states that for a given initial wavefunction, there exists a time-dependent external potential of the system that uniquely relates to its time-dependent density. The time-dependent approach lacks the general minimization principle of its DFT counterpart, making the proof of TD-DFT significantly more involved.[39] Therefore, here we will only provide a brief overview of the principles behind the method. A more detailed account can be found in the book by Burke and Gross.[66]

In a general and rather superficial way, it can be shown that the frequency-dependent average polarizability $\alpha(\omega)$ describes the effect of a time-dependent field of energy (frequency) ω(t) on the dipole moment of a system. Equation 2.4 shows how $\alpha(\omega)$ relates to the electronic spectrum of a system with excitation energies $E_I - E_0$ for each state I, summed over all excited states.

$$\alpha(\omega) = \sum_I \frac{f_I}{\omega_I^2 - \omega^2} \tag{2.4}$$

This equation shows spikes (poles) for all excitation energies as the fraction diverges when $\omega = \omega_I$. The residues (f_I) correspond to the oscillator strength of each transition. This dimensionless parameter is directly related to the transition dipole strength and it provides information on the intensity (molar extinction coefficients) of the excitation.[69] In the TD-DFT framework, the differences between KS orbital energies are used as a first approximation to the excitation energies followed by a systematic shifting towards the true values. Normally, only the low energy excited states are desired, so the calculation is usually restricted to a few excitations. However, computational strategies converge by minimizing $E_I - E$ for all states requested. So the more excitations included, the more accurate the description. In light of this, the selection of an adequate exchange-correlation functional is crucial for an accurate TD-DFT description, since the orbital energies, especially those of highly lying states, are very sensitive to the decay of the exchange-correlation potential at long distances.[66]

Broken Symmetry SCF

Frequently in reactions involving light-absorption there are systems in which not all electrons of opposite spin are paired. These cases can only be correctly described by a multiconfigurational approach to the wavefunction using high level computational methods. Yet, the unrestricted Kohn-Sham (UKS) formalism can provide energies that are accurate enough. In this approach spin-density functionals are used to obtain the best (energetic) possible description

of the physics involved.[39] The drawback is that the resulting spin densities are formally incorrect, as the KS orbitals obtained from an unrestricted calculation are not eigenfunctions of the spin. In these cases, the unrestricted solution leads to the breaking of the spin symmetry, as it is contaminated by higher multiplicity states. However, because UKS allows for the spin symmetry to be broken, the greater flexibility allows the energies of open-shell results in much better energies than those obtained with a restricted approach, even if the latter shows more realistic densities. Therefore, this is usually the preferred method for the calculation of systems with unpaired opposite-spin electrons.

Intersystem Crossing

Frequently in reactions involving excited states, there is more than one spin state involved. Among the internal conversion mechanisms involved in the decay of excited states, the transition from the singlet excited state to a lower energy triplet state is the most common pathway to initiate photochemistry.[70] This is due to the slower decay of triplet states compared to singlets, as relaxation of the former is spin-forbidden. The longer lifetime of triplet intermediates allows them to undergo chemical transformations that would be uncompetitive compared to relaxation in the same spin state. The transition from one N-dimensional spin state to another takes place across a *seam* of N-1 dimensions. The lowest energy point in the seam surface is called the Minimum Energy Crossing Point (MECP) and plays a similar role to transition states in reactions involving one electronic state.[71]

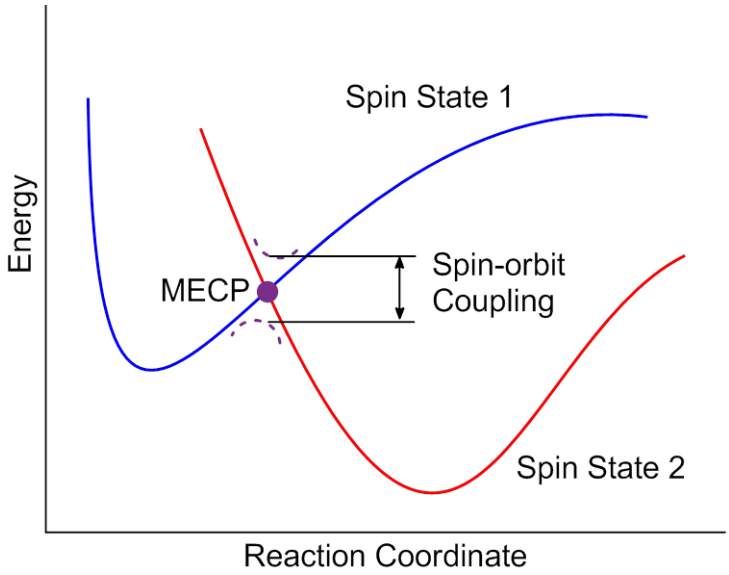

Figure 2.3: Marcus diagram for an exoergic outer-sphere SET.

Formally all spin transitions are forbidden due to orthogonality of the spin part of the wavefunction. Intersystem Crossing (ISC) can only take place due to relativistic effects, mainly spin-orbit coupling. The strength of the coupling determines the probability of spin transition and ultimately the rate of ISC.[70] Figure 2.3 shows a typical diagram for a spin transition. Being a relativistic property, spin-orbit coupling is stronger in heavier atoms and weaker in lighter ones. In the case of weak spin-orbit coupling, the MECP energy is a good estimate of the energy cost of the crossing, and the rate associated.

In the work presented in this thesis, the computation of ISC was limited to transitions involving molecular fragments that contain exclusively light atoms. For this reason, the MECP was used as an estimate of the energy barrier of the spin-transition. The chosen method for the computation of MECP was first introduced by

Harvey et al.[72] and is itself a variation of the algorithm originally proposed by Schlegel et al.[73] In this approach, the MECP energy consists of computing the energies E_i and corresponding gradients (∂E_i / ∂q) with respect to the nuclear coordinates, of both potential energy surfaces (PES). This results in two effective gradients f and g. Both gradient vectors are orthogonal, and go to zero at the MECP where the energy gradients of both surfaces are parallel. Around the MECP, f is perpendicular (orthogonal) to the crossing hyperline, while g is parallel and points towards the minimum. Equations 2.5 and 2.6 show both gradients:

$$f = (E_1 - E_2)\left[\frac{\partial E_1}{\partial q} - \frac{\partial E_2}{\partial q}\right] = (E_1 - E_2)x_1 \tag{2.5}$$

$$g = \frac{\partial E_1}{\partial q} - \frac{x_1}{|x_1|}\left[\frac{\partial E_1}{\partial q} \cdot \frac{x_1}{|x_1|}\right] \tag{2.6}$$

The geometry of the MECP is then optimized following the sum of f and g via a steepest descent algorithm. In the modification implemented by Harvey et al. The energy difference is calculated at the full level of theory, and the gradients at a lower lever to speed up the search. The idea behind the approximation is that energies are more level-sensitive than geometries, thus a lower level optimization that uses high-level energy difference as convergence criteria should proved a good estimate of the MECP. This approach is similar to the widely used computation of high-level single point energies at stationary points optimized at a lower level.

Quantum Yield in Photoactivated Chain Reactions

One of the experimental properties used to study the efficiency of photoactivated reactions is the quantum yield (ϕ).[74] It is expressed by equation 2.7, where $N_{product}$ is the amount of product molecules formed, and $N_{photons}$ is the amount of photons absorbed by the system.

$$\phi_{exp} = \frac{N_{product}}{N_{photons}} \tag{2.7}$$

This parameter provides information on the percentage of molecular excitations that result in the desired chemical reaction. In reactions that can only reach the desired product via direct activation by light, the quantum yield is ≤ 1. A process which approaches unity is considered a highly efficient one. However, photoinduced generation of free radicals can also initiate a chain reaction.[75] In this case, quantum yield is greater than 1, sometimes by several orders of magnitude.

The computation and prediction of quantum yields using DFT methods constitutes a challenge, since there is no way to determine the amount of photons absorbed. The absorbance of a molecule is determined by Beer-Lambert law and its relation to oscillator strength is not straightforward.[76, 77] In the case of chain reactions the assumption can be made that all absorbed photons lead to the desired product. This is a gross approximation considering how

reactive free radicals are, and it certainly does not provide quantitative information on the quantum yield. However, chain reactions with low quantum yield indicate a competition between chain propagation and direct activation, and here DFT methods can play a role in qualitatively reproducing the competition. If a computational model for the mechanism predicts the formation of the product via both direct activation (termination) and chain propagation, then quantum yield can be expressed by equation 2.8:

$$\phi_{calc} = \frac{N_p + N_t}{N_t} \tag{2.8}$$

where N_p stands for the amount of product molecules formed via the propagation pathway, and N_t corresponds to the amount of product formed via the termination pathway. ϕ_{calc} relates to ϕ_{exp} in that $N_p + N_t = N_{product}$, and $N_t = N_{photons}$ if all absorbed photons are converted to the desired product, which is accurate enough in a reaction with a high yield and only one chromophore.

Selectivity

A chemical reaction can be viewed as a reorganization of the connectivity in a particular molecular system. That is, the formation and/or breakup of one or more chemical bonds. Each group of simultaneous changes in the connectivity during such a transformation is referred to as a reaction step, and All reaction steps directly connect

two intermediates via an energy barrier. A sequential description of these steps constitutes a reaction pathway.[78]

Typically, there are several reaction pathways that connect reactants to products. These can either be shifts in the order of the reorganization steps, or conformational variations of one or more of those steps. To follow a pathway, the reactants must overcome the energy barrier corresponding to said pathway. The energy barrier is normally defined as the largest energy difference between a transition state and a previous intermediate, in a particular direction. The most plausible pathway is thus the one with the lowest energy barrier. However, a portion of the molecules in the reactants follow other pathways as well.

If more than one pathway with similar energy barriers results in a different irreversible product, all of those products are present at the end of the reaction. The relative abundance of each product (or the share of reactants that follows each pathway) is described by a Boltzmann distribution,[79] which can be interpreted as the probability P_i of a particular state i (in this case a transition state which irreversibly leads to one product) with energy ΔG_i to be populated by a molecule at a given temperature T. The relation is shown in equation 2.9, where R is the gas constant, and $Q(T)$ is the partition function that encompasses the contributions from all possible states.

$$P_i = \frac{e^{-\Delta G_i/(RT)}}{Q(T)} \tag{2.9}$$

According to Transition State Theory (TST), there are three possible outcomes for a system described by this equation, depend-

ing on the energy of the molecule. If the molecule has energy $\Delta G < \Delta G_i$, the state i is never populated and the product is not formed. On the other hand, if $\Delta G > \Delta G_i$ the extra kinetic energy causes the system to keep moving in the direction of the reaction coordinate, and the product is generated for all cases. Finally, if $\Delta G = \Delta G_i$ the transition state is populated with zero remaining kinetic energy. In this case there is a 50% chance of returning to reactants or generating the product. The exponential dependence on the energy means that as ΔG_i increases, there is an exponentially lower probability of populating i at a particular T. Going back to the case with multiple products, if $\Delta G_j < \Delta G_i$ then P_j is greater than P_i by a factor proportional to $e^{-(\Delta G_j - \Delta G_i)}$. For example, two competing processes with energy barriers that differ by 2.5 kcal.mol^{-1} generate both products in a 20:1 ratio, or 95% selectivity towards the product with the lower energy barrier.

In the particular case of enantioselectivity, the two enantiomers have the same energy and span from the same precursor in the reaction scheme. Thus, like in the case of other irreversible reactions with multiple products, selectivity can only be governed by the kinetics of the system. In this sense, the transition states leading to these enantiomers are diastereomeric, hence they have different energies. The origin of enantioselectivity is that the pathway leading to one enantiomer (1) goes through a TS higher in energy than the one leading to the other enantiomer (2). Therefore, the ratio (r) (which must include all the pathways leading to each enantiomer) is expressed by equation 2.10

$$r = \frac{\sum_i e^{-\Delta G_{1i}/(RT)}}{\sum_i e^{-\Delta G_{2i}/(RT)}} \tag{2.10}$$

Finally, enantiomeric excess (ee) can be obtained from r as it is the relative amount of one enantiomer over the other by an r-ratio, expressed in percentage.

Kinetic Models

As mentioned above, for a simple mechanism it is easy to get an idea of the kinetics involved in the reaction by comparing energy barriers. However, for processes involving non-straightforward kinetics such as loops, ramifications, or large differences in initial concentrations, the use of kinetic models may be crucial to understand experimental results.[80] The construction of a kinetic model involves separating the overall mechanism into elementary steps. For this separation to be accurate, all relevant side reactions and deactivation paths must be included. However, fringe processes with very high energy barriers can be neglected as they are expected to have a low impact on the overall outcome. The rate of each step is calculated as the variation in concentration of the product versus time, and the concentration of the product is the concentration of the reactants times a constant called the rate constant.

In the framework of the work presented in this thesis, the rate constants for all elementary steps were calculated using Eyring's equation (equation 2.11).[81] Here the activation energies were determined as the difference in free energy between the transition state corresponding to a particular state, and the previous intermediate connected to it.

$$k_{rate} = \frac{k_B T}{h} e^{-\Delta G^{\ddagger}/(k_B T)} \tag{2.11}$$

Where k_{rate} is the rate constant, k_B is the Boltzmann constant, T is the temperature, and h is Planck's constant. Thus, to build the kinetic model it is necessary to know the activation energy (i.e. the energy barrier) of all elementary steps. To illustrate how the simulation is carried out, consider the following reaction mechanism for the conversion of **A** to **D**. Figure 2.4 shows the energy profile corresponding to this hypothetical reaction.

$$\mathbf{A} \rightleftharpoons \mathbf{B} + \mathbf{C} \longrightarrow \mathbf{D}$$

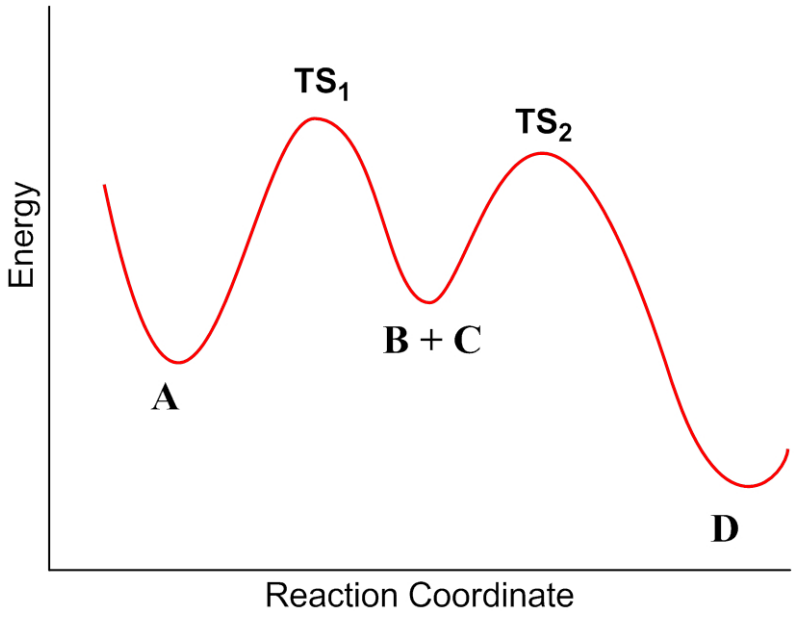

Figure 2.4: Free energy profile of the **A** $\longrightarrow$ **D** reaction.

The reaction step from **A** to **B** + **C** is marked as an equilibrium since the energies of both states are comparable. This is not the case for the generation of **D**, as the reverse barrier is too high to return to the intermediate state. In this simple case there are three rate equations to consider. (1) The dissociation of **A** into **B** and **C**, (2) the addition of **B** and **C** to restore **A**, and (3) formation of **D** from **C** and/or **B**. Each of these equations has a rate constant associated which can be calculated using the energy barrier for each step (e.g. k_{-1} is calculated using the energy difference between $\mathbf{TS}_1$ and **C** + **B**).

1. $\mathbf{A} \xrightarrow{k_1} \mathbf{B} + \mathbf{C}$
2. $\mathbf{B} + \mathbf{C} \xrightarrow{k_{-1}} \mathbf{A}$
3. $\mathbf{B} + \mathbf{C} \xrightarrow{k_2} \mathbf{D}$

With the elementary step equations, it is simply a problem of solving the differential rate equations for all species involved to obtain the profile of their concentrations in time. Normally these equations are solved using algorithms. In the work presented in this thesis, concentration profiles were computed using Acuchem software.[82] Kinetic simulations were carried out to obtain information on reaction mechanisms that do not follow a simple kinetic behavior. For example, in Chapter 3 a kinetic model is built to account for the large difference in the concentration of two key photogenerated intermediates, whereas in Chapter 4 kinetic simulations are used to evaluate the yield of reactions involving loops affected by light absorption.

In the particular case of SETs, estimation of the rate constant is considerably less straightforward. This is because the pre-

exponential factor for non-adiabatic SET is not k_BT/h. In fact, it is only equal to Eyring's equation in cases where the coupling between D and A is very high (i.e. intramolecular SETs). For cases where coupling is very weak, like bimolecular outer-sphere transfers, the pre-exponential factor is smaller by some orders of magnitude.[83] In the kinetic simulations presented in this thesis, the pre-exponential factor for SETs was considered $0.01*k_BT/h$.

Free Energies in Solution

Electronic structure programs calculate thermodynamic properties (enthalpy, Gibbs free energy, entropy, etc.) at some default standard state concentration (pressure) and temperature. In the case of Gaussian09 this is 1 atm and 298 K. According to ideal gas law the concentration at these conditions is 0.040874 M. The usual reference state however is 1M. So free energy calculations need to account for the cost of converting from one concentration to the other. Equation 2.12 shows the straightforward conversion from ideal gas to 1M.

$$\Delta G_{1M} = -nRTln\left(\frac{0.040874M}{1M}\right) \tag{2.12}$$

This results in 1.893 kcal.mol^{-1} for each molecule. If the number of molecules in the process (n) is conserved, the conversions cancel out since the free energy of a process is calculated by subtracting the energy of both states involved. For any other process however,

the correct free energy needs to be corrected by adding $1.893\Delta n$ 1.893 kcal.mol^{-1}. This conversion is frequently neglected in computational works as the aim is to obtain qualitative information and large entropic error is expected in addition/dissociation processes. However, when quantitative agreement is expected, the conversion becomes necessary.

Marcus Theory of Electron Transfer

Many light-driven processes involve bimolecular one-electron oxidation/reduction. These single electron transfer (SET) steps are fundamentally different from most elementary steps in the sense that no bond is formed or broken during the process. That is, both the electron donor (D) and the acceptor (A) maintain their connectivity throughout the SET. Such a process is referred to as outer-sphere electron transfer, as it differs from bond-alter SETs in that the "inner sphere" of the reactants remains unchanged. In fact, the reaction coordinate for an SET is the rearrangement of the nuclei, electrons and solvent molecules in the immediate vicinity of D and A. For this reason, the standard treatment of locating a transition state through a well defined negative eigenvalue in the Hessian matrix, related to a vibration of the reaction coordinate is impossible.

To estimate the energy barrier for a SET, a brilliantly simple method was originally developed by Rudolph Marcus in the mid 20th century.[84, 85] Marcus theory states that for a donor-acceptor pair, the activation energy of the SET can be estimated by finding the crossing point of two intersecting parabolas centered on each stage of the reaction (reactants and products). The two parabolas

correspond to the equilibrium geometries of both stages. Unlike in most chemical processes where an energy profile consists of a single reaction coordinate containing both products and reactants, outer-sphere SET is not adiabatic, hence the use of two parabolas to describe both energy surfaces. Figure 2.5 shows a diagram for an exoergic SET in which the activation energy ($\Delta G^{\ddagger}$) is represented.

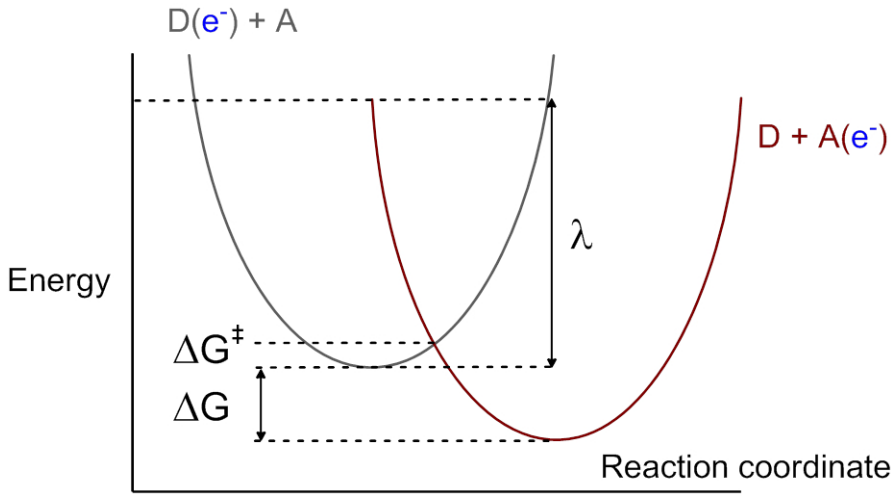

Figure 2.5: Marcus diagram for an exoergic outer-sphere SET.

The vertical crossing point between the parabolas shown in figure 2.5 can be calculated using equation 2.13, where ΔG is the free energy difference between reactants and products, and λ is the reorganization energy of all nuclei involved in the SET, including solvent molecules. That is, the energy cost of every change the system undergoes as a result of SET without actually transferring the electron. Marcus theory also predicts that, as ΔG becomes more negative the energy barrier for SET decreases until virtually disappearing (when the parabola corresponding to the products intersects the reactants at the minimum). However, for very large energy differences, an

energy barrier reappears as the products parabola intercepts the reactants to the left of the minimum, indicating that very exoergic SETs are not barrierless. This phenomenon is known as the Marcus Inverted Region.[84]

$$\Delta G^{\ddagger} = \frac{(\Delta G + \lambda)^2}{4\lambda} \tag{2.13}$$

The energy barrier for outer-sphere SETs usually depends strongly on the reorganization energy of the solvent molecules around the reactants. Normally, photoinduced SETs take place when D and A are relatively close ($\leq$ 15 Å).[86, 87] However, the reactants cannot be at very short distances since SETs at close range usually lead to fast recombination of charges (back SET) resulting in no net transfer.[88] In the case of photoinduced electron transfer (PET), recombination is always an issue that affects overall efficiency, as back SET yields the lower energy ground state photocatalyst rather than the MLCT excited one. As a consequence, ΔG is always large and negative resulting in fast SET in the Marcus inverted region.

Extensive computational work has been carried out on the kinetics of electron transfer.[89] Most of the studies have focused on protein chemistry,[90] photovoltaic cells,[91] and semiconductors.[92] DFT-based methods have been developed to calculate the pre-exponential electronic coupling term,[93] and extensive theoretical work has been devoted to the nature of the donor-acceptor precursor in strongly coupled inner-sphere transfer,[94] including photoinduced electron transfer.[95] However, most estimations of the energy

barrier involve molecular dynamics.[96, 92]

In the particular case of bimolecular outer-sphere electron transfer, our approximation was to calculate the reorganization energy for the separated reactants as the SET can take place at distances as far as 10 Å.[88] The reorganization energy was computed separately for each component (nuclear reorganization (λ_N) and solvent reorganization (λ_S). λ_N was obtained by calculating energy cost of distorting the geometry of the reactants to that of the products. Equation 2.14 shows the scheme for the computation of λ_N where the subscript corresponds to the equilibrium geometry used for the calculation. That is, E_E represents the electronic structure of E at its equilibrium geometry, while E_G represents the electronic structure of E at the equilibrium geometry of G.

$$\lambda_N = D(e^-)_D + A_{A(e^-)} - D(e^-)_{D(e^-)} + A_A \qquad (2.14)$$

This component of the total λ is by far the smallest one.[84] The solvent reorganization energy (λ_S) is considerably larger and was computed at using the continuum solvent model described above. In figure 2.5, λ is shown as the energy difference between the electronic configuration of the reactants with the nuclear coordinates and solvation of products, and the electronic configuration of the reactants with the nuclear configuration and solvent of the reactants. Therefore, λ_S can be considered the energy difference between the reactants with the solvation of the products, and the reactants with the solvation of the reactants, at the same geometry. This method

to obtain the solvent reorganization energy has been used successfully to reproduce experimental results.[97, 98] Equation 2.15 shows the calculation scheme for λ_S where the superscript in square brackets represents the equilibrium continuum solvent cage. That is, $E^{[E]}$ represents the electronic configuration of E surrounded by the optimized continuum solvent cage of E, at the equilibrium geometry.

$$\lambda_S = D(e^-)^{[D]} + A^{[A(e^-)]} - D(e^-)^{[D(e^-)]} + A^{[A]} \quad (2.15)$$

This simple method for estimation of the SET energy barrier has two potential sources of error. The first one is that it completely neglects the distance between the reactants, by calculating the λ_S parameter essentially at infinity. The justification for this is that the continuum solvent cage with change more dramatically in the near vicinity of D and A. This assumption is supported by experimental evidence, as the near solvent molecules shift much more dramatically than the outer ones.[86] The other major approximation is in the use of PCM to describe the change in the solvation cage which is the dominant contribution to λ. Therefore, in the work presented in this thesis we only use energy barriers obtained with this method to make qualitative interpretations of our results, or to make comparisons between two or more SETs which are expected to be more reliable due to error cancellation.

Chapter 3

Photoactivated Reactions

Part I - Perfluoroalkylation of Arylacetates

In recent years, significant effort has been put into the development of efficient strategies for the addition of functional groups containing fluorine. The introduction of perfluoroalkyl groups dramatically alters the properties of organic compounds, and thus constitutes a technique often used to enhance the biological activity of drug candidates in medicinal chemistry.[99, 100] Traditional methodologies employed stoichiometric amounts of transition metal compounds to promote cross-coupling processes.[101] These strategies have been replaced by catalytic alternatives based on copper and palladium-based systems increasing the effectiveness of the process. These methods however, do not perform direct functionalization, instead they go through halides or boronic acid precursors.[102, 103] Direct paths are more desirable and usually involve the formation

of perfluoroalkyl radicals which react with arenes via homolytic aromatic substitution (HAS) thanks to their strong eletrophilic character.[104, 105, 106] However, thermal generation of these radicals often require harsh reaction conditions.[107, 108, 109]
Recently, perfluoroalkyl radicals have been generated under mild conditions using photoredox catalysis.[110] Melchiorre *et al.* went one step further by getting rid of the photoredox catalyst, metallic or otherwise, by generating the perfluoroalkyl radical directly. [111] They managed to accomplish this by forming electron donor-acceptor (EDA) complexes.[112, 113] These adducts have a visible light charge transfer (CT) excitation in which an electron is transferred from the donor to the acceptor forming two radicals. The reaction is illustrated in figure 3.1, and involves an α-cyanoarylacetate (**1**) as the donor and perfluoroalkyl iodide (**2**) as the acceptor.

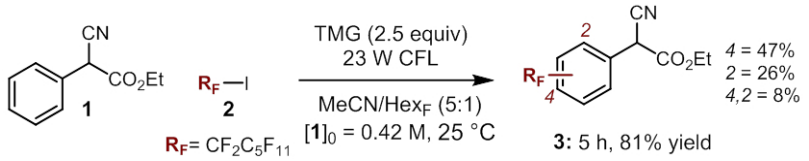

Figure 3.1: General scheme of the perfluoroalkyaltion reaction.

The absorption of visible light by the EDA forms the perfluoroalkyl radical which can attack the aryl ring in the acetate via HAS and yield the fluorinated arylacetate product (**3**).
Despite the relevance of this approach in the search for efficient perfluoroalkylation, many aspects of the mechanism were still largely unknown. There were two main aspects that made the computational study of this reaction interesting from a mechanistic point of view. One was the availability of a variety of experimental mechanistic data. The other was the existence of experimental observations

that remained unexplained.

Reaction Mechanism

The perfluoroalkylation proceeds regioselectively at the *para* and *ortho* positions in the aromatic ring in **1** in a 2:1 ratio. A quantum yield of 3.8 was determined at λ=400nm, which suggests a radical chain mechanism as the main pathway. The preliminary mechanistic proposal (figure 3.2) was based on the aromatic substitution initiated by the photochemical activity of the EDA complex **II**. This EDA complex consists in the aggregation of the enolate **I**, which is formed after deprotonating **1**, and **2**. A light-driven single electron transfer (SET) taking place between the fragments of **II** releases the radical $\mathbf{R}_F{}^{\bullet}$ which then reacts with **I** to form the cyclohexadienyl radical anion **III**. SET from **III** to **2** propagates the chain reaction and results in neutral intermediate **IV**, which is then deprotonated to yield the product **3**.

However, there were some aspects of the mechanism that were not clear. Some experimental findings were difficult to explain, such as the regioselectivity of the reaction towards the aromatic ring, while the predictable formation of the α-carbonyl perfluoroalkylated adduct **4** was not observed (figure 3.3-a). In addition, the observed quantum yield of 3.8 was relatively low for HAS reactions, hinting at a competing termination pathway. Another obscure aspect was the reason why the process is completely inhibited by small changes in the reactant, such as replacements of the cyano by NO_2 (figure 3.3-b). Moreover, α-*para*-nitrophenylacetate **5** behaves in opposite

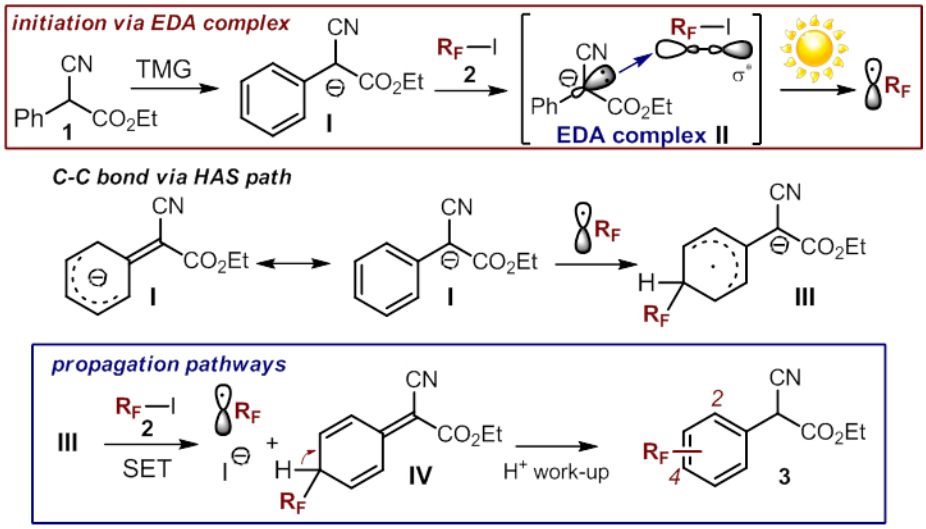

Figure 3.2: Preliminary radical chain mechanism.

manner under the same reaction conditions, with the α-carbonyl perfluoroalkylation being the only observed product (figure 3.3-c), the origin of this change in regioselectivity was unclear.

In order to answer these questions we carried out a thorough DFT investigation on the reaction. We chose a model system in which the perfluoroalkyl iodide was C_3F_7I (**2a**) to avoid unnecessary conformational issues, while α-cyanoaphenylacetate was used as the donor. Calculations were carried out using the ω-B97x-D functional[47] with continuum solvent contributions from the Polarizable Continuum Model (PCM) as implemented in Gaussian09.[114] TD-DFT calculations were performed using the basis set SDD(P) with a diffuse function for I, and 6-311++G(d,p) for light atoms, while geometry optimizations were calculated with the SDD basis set for I and 6-31+G(d) for light atoms.[115, 116, 117, 118] Microkinetic models were evaluated using the Acuchem software.[119]

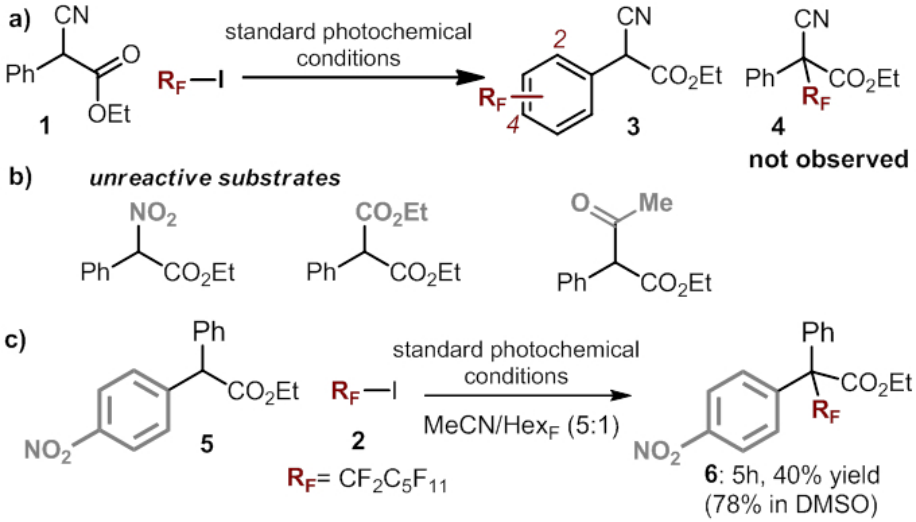

Figure 3.3: Additional experimental evidence on the perfluoroalkylation of different substrates.

The first step in the calculated mechanism is the formation of the EDA complex **II**, which is an adduct between $\mathbf{R}_F\mathbf{I}$ and **I** at 5.9 kcal.mol^{-1} above separated reactants. Our TD-DFT calculations found a HOMO-LUMO charge transfer (CT) excitation with a maximum at 386 nm, which corresponds to SET from the anionic fragment to electron-deficient perfluoroalkyl. The HOMO of **II** (figure 3.4-a) is completely localized in the enolate fragment of the EDA, while the LUMO (figure 3.4-b) is localized in the perfluoroalkyl iodide fragment. Moreover, it corresponds to an anti-bonding σ orbital in the C-I bond region, indicating a dissociative transition.

Optimization of the open-shell singlet state within the TD-DFT framework failed due to the presence of other excited states with similar energies. This prompted us to estimate the behavior of the excited EDA through the analogous triplet state. Optimization of the triplet EDA corresponds to a productive SET (*i.e.*, one in which

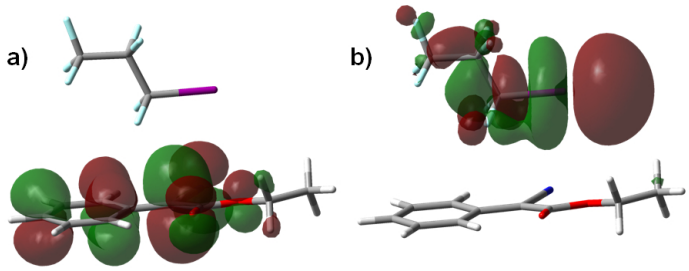

Figure 3.4: HOMO and LUMO of EDA complex **II**.

the spin of the transferred electron has been inverted and the donor and acceptor drift away, rather than transferring the electron back). Geometry optimization of the triplet state leads to the barrierless breakdown of the EDA into three fragments: the radical enolate **V**, the radical perfluoroalkyl $\mathbf{R}_F^{\bullet}$, and iodide.

Propagation/Termination Dichotomy

The computed reaction mechanism is summarized in figure 3.5. Following the breakdown of complex **II** there is a bifurcation into two mechanistically relevant pathways. $\mathbf{R}_F^{\bullet}$ can combine with **V** to form intermediate **IV**, which can easily lose a proton to restore aromaticity and yield the HAS product **3**. This mechanism corresponds to the *termination* path, as all radicals formed by direct light activation are combined into a single product, requiring the absorption of a second photon to restart the reaction. The barrier for the radical combination is beyond the capability of DFT methods, as it involves the multiconfigurational superposition of an open-shell singlet with a closed shell one. However, combination of two free radicals is often diffusion controlled, and barriers are sel-

dom significant.[120] Therefore, we assumed radical combination to be an easy diffusion-controlled process.

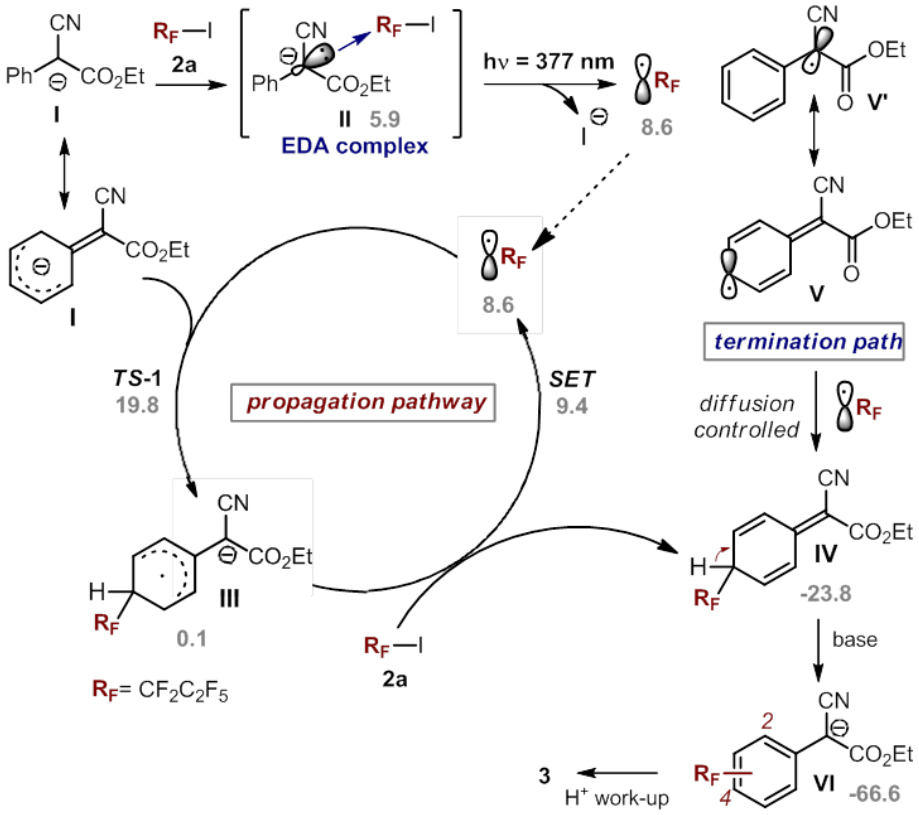

Figure 3.5: Calculated mechanism of the propagation/termination dichotomy. Free energies (gray color) in kcal.mol^{-1}.

The other possible pathway consists in the radical trapping of $\mathbf{R}_F{}^{\bullet}$ by **I** to form the anionic intermediate **III**, through the corresponding transition state ***TS*-1**. This stage constitutes the selectivity determining step, as the radical will form a C-C bond with one of the carbon atoms in the aromatic system. At this point, the radical intermediate **III** can transfer an electron to a **2a** molecule to form a new $\mathbf{R}_F{}^{\bullet}$ and the intermediate **IV**. This constitutes the *propa-*

gation path, as a new radical species is formed without absorption of a photon. The barrier for the SET was estimated using Marcus theory according to the scheme described in chapter 2.

The highest energy point in the propagation cycle is in the transition state ***TS*-1** leading to **III**, with an energy 19.8 kcal.mol^{-1} above reactants, representing a barrier of 11.2 kcal.mol^{-1} above $\mathbf{R}_F{}^{\bullet}$. The competition between the chain propagation manifold (11.2 kcal.mol^{-1} barrier) and the termination pathway (diffusion-controlled) determines the quantum yield of the overall process.

If the competition between propagation and termination only depended on the comparison of the highest free energy points, as it is often the case for competing processes in homogeneous catalysis,[121] the conclusion would be that radical combination dominates with no chain propagation observed. This scenario implies a quantum yield of $\leq$1, which would be in sharp disagreement with the experimental quantum yield of 3.8. However, the treatment of comparing high energy points fails to take into account the large difference in the concentrations of the species involved.

The radical species $\mathbf{R}_F{}^{\bullet}$ is common to both termination and propagation pathways. Therefore, its concentration has no impact on the competition. The enolate **I** on the other hand, which is the key intermediate in the chain propagation path, is formed by a quantitative deprotonation of substrate **1**, whereas the radical intermediate **V** is a transient species in very small concentration, produced by visible light absorption of the EDA.[122] In order to take concentration differences into account and estimate a theoretical quantum yield, we carried out a kinetic simulation.[123] The method for estimating the quantum yield from the kinetic simulation is described in chapter 2. The model was based on the following equations:

1. $\mathbf{1} \xrightarrow[\text{base}]{k_{H1}} \mathbf{I}$
2. $\mathbf{I} + \mathbf{2a} \xrightarrow{k_1} \mathbf{II}$
3. $\mathbf{II} \xrightarrow{k_{-1}} \mathbf{I} + \mathbf{2a}$
4. $\mathbf{II} \xrightarrow{k_\nu} \mathbf{V} + \mathbf{R}_F{}^\bullet + I^-$
5. $\mathbf{V} + \mathbf{R}_F{}^\bullet \xrightarrow{k_{diff}} \mathbf{IV}$
6. $\mathbf{R}_F{}^\bullet + \mathbf{I} \xrightarrow{k_2} \mathbf{III}$
7. $\mathbf{III} + \mathbf{2a} \xrightarrow{k_{ET}} \mathbf{IV} + \mathbf{R}_F{}^\bullet + I^-$
8. $\mathbf{IV} \xrightarrow[\text{base}]{k_{H2}} \mathbf{VI}$

Whenever possible, the rate constant for each step was determined using Eyring's equation with the calculated energy barrier as the activation energy. The rate constant for the photodissociation (k_ν) involves several radiative and nonradiative processes that are beyond the scope of this work, as they would require very high level calculations. We took the approach of adjusting the dissociation constant value to the available experimental data. Thus, it was adjusted so that the reaction would fit 85% conversion in 5 hours. This adjustment was considered valid since the target experimental parameter was the quantum yield and not the conversion.

As previously stated, we were not able to compute the barrier for the radical combination. However, the rate constant for diffusion controlled radical combinations in acetonitrile is known to vary from 2x10^9 M^{-1}s^{-1} to 1x10^{10} M^{-1}s^{-1}.[120] Therefore, the simulation was carried out using both the upper and lower bounds of the rate constant for step 5 (k_{diff}).

The calculated quantum yield, which strongly depends on said constant, ranged from 3 to 71. These values are in good agreement with the experimental quantum yield (which is 3.8), considering how sensitive this parameter is towards small changes in the energy barriers. Furthermore, the rate constant for the radical combination is expected to resemble the upper bound rather than the lower, since both radicals are formed at very close range after excitation of the EDA. If k_{diff} resembles more closely the experimental upper bound of 1x10^{10} $M^{-1}s^{-1}$, then the calculated quantum yield is closer to 3 rather than 71, which is remarkably close to the experimental value.

Regioselectivity

Melchiorre *et al.* noted that the only product observed was the HAS perfluoroalkylated acetate **3** with a *para/ortho* ratio of 2:1, and no α-carbonyl perfluoroalkylated product **4** was detected (figure 3.3-a). As previously shown, the regioselectivity determining step is the formation of the C-C bond between $\mathbf{R}_F{}^{\bullet}$ and intermediates **V** and **I**.

We calculated the transition states corresponding to the C-C bond formation at the three possible positions to determine the origin of regioselectivity. The free energy barriers for the trapping step from **I** are 11.2, 11.7, and 20.8 kcal.mol^{-1} for *para*-**3**, *ortho*-**3** (HAS products), and **4** (α-carbonyl perfluoroalkylated product), respectively. Figure 3.6 shows the optimized geometries for all transition states.

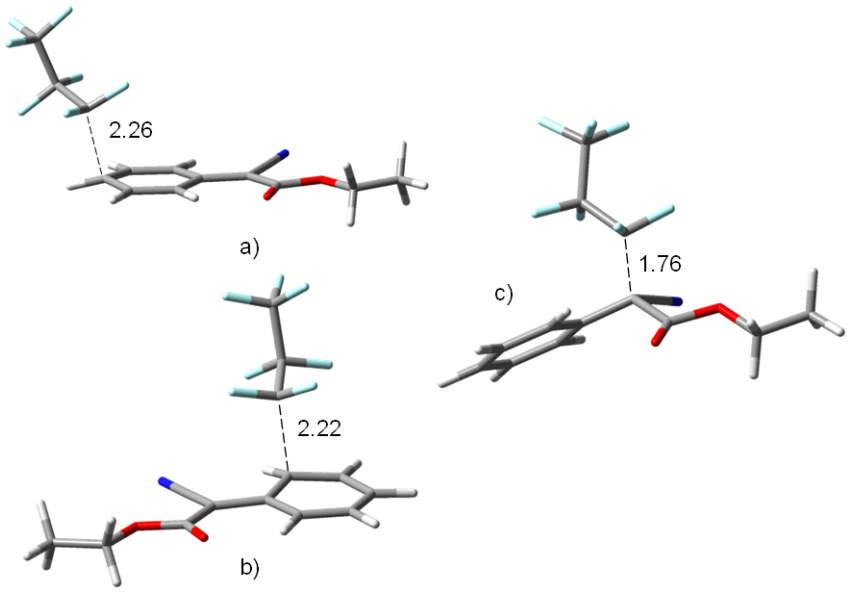

Figure 3.6: Optimized geometries of transition states for radical trapping in the formation of *para*-**3** (a), *ortho*-**3** (b), and **4** (c). Distances in Å.

The calculated barriers are in very good agreement with experimental results, as they correctly reproduce experimental regioselectivity. The origin of said regioselectivity was studied by carrying out a distortion/interaction analysis on the corresponding transition states.[124, 125, 126] The results are shown in table 3.1. This analysis considers potential energies ($\Delta V^{\ddagger}$), which differ from free energies ($\Delta G^{\ddagger}$) in the entropic term but follow the same trend, as entropic penalties are very similar for all cases. Decomposition of ($\Delta V^{\ddagger}$) indicates that the key factor precluding the perfluoroalkylation on the α-carbonyl position is the high cost of deforming the enolate fragment, which is far above the value for both aromatic substitution transition states.

Table 3.1: Distortion/interaction analysis on the transition states for radical trapping. Relative potential and free energies in kcal.mol^{-1}

product	$\Delta V^{\ddagger}$	$\Delta V^{\ddagger}_{dist}(\mathbf{I})$	$\Delta V^{\ddagger}_{dist}(\mathbf{R}_F{}^{\bullet})$	$\Delta V^{\ddagger}_{int}$	$\Delta G^{\ddagger}$
para-**3**	-1.0	3.1	2.5	-6.7	11.2
ortho-**3**	-1.7	3.8	2.8	-8.3	11.7
4	6.6	15.5	6.6	-15.5	20.8

The difference in distortion energies is apparent from the optimized geometries shown in figure 3.7, which display an significant distortion of the planar system in the transition state leading to product **4**, while the geometry deformation to reach product **3** is minimal in comparison. The sum of the angles in a trigonal planar system is 360^o and the enolate fragment in the transition state leading to **3** has internal angles of 356^o, whereas the internal angles of the α-carbon in the transition state leading to **4** are 334^o, evidencing the greater distortion.

The preference for the termination reaction (radical coupling between **V** and $\mathbf{R}_F{}^{\bullet}$) could not be analyzed in the same way because of the impossibility of locating radical coupling transition states in DFT. However, the distortion of the planar system in the enolate radical **V** is expected to be analogous to that in **I**, as the geometries of both species in equilibrium are nearly identical. Moreover, the C-C bond formation involves rearrangement of the carbon in the enolate from sp^2 to sp^3 in both cases. Therefore, the same preference observed for $\mathbf{TS}_1$ is likely to take place in the radical combination step. If this is the case, then both propagation and termination lead to a similar product distribution, hence the observed regioselectivity.

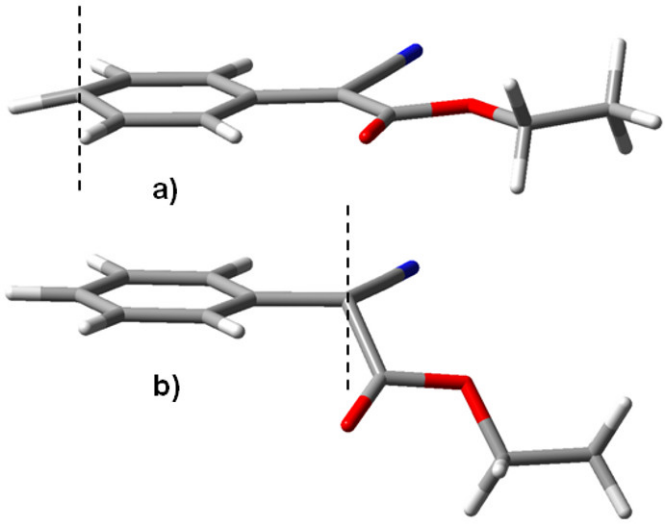

Figure 3.7: Enolate fragment in the transition states corresponding to products *para*-**3** (a), and **4** (b).

Alternative Mechanism for the Termination Pathway

The mechanism shown in figure 3.5 reproduces experimental results satisfactorily. However, we also carried out calculations on a different path. The basis for this pathway is that after the first perfluoroalkylation, the radical anion **III** may reduce radical **V** rather than **2a** (Figure 3.8). This possibility constitutes an additional termination path, and the barrier for the SET to **V** is considerably lower than that of the propagation mechanism (7.4 *vs* 11.4 kcal.mol^{-1}). This alternative termination however, is not competitive in the kinetic model since the concentration of **V** is much lower than that of **2a**; hence the contribution of this pathway to the product is virtually non-existent. Furthermore, it is less efficient than

the original termination pathway due to the presence of a measurable barrier higher than the diffusion controlled process of radical combination.

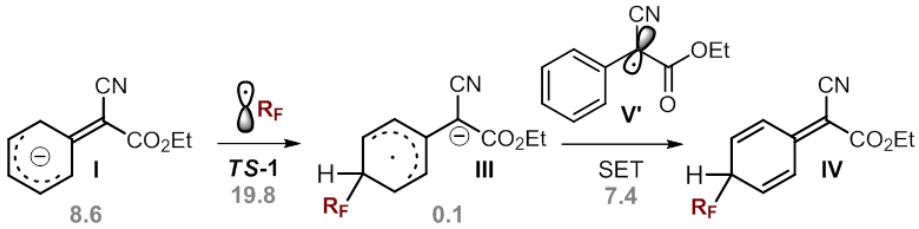

Figure 3.8: Alternative termination pathway. Free energies in kcal.mol^{-1}.

Reactivity of Similar Substrates

Once we had a working model for the mechanism, we tested its ability to reproduce the reactivity of other substrates with similar electron-withdrawing groups, which afforded contrasting experimental results (figure 3.3-b,c). Among the experimentally evaluated substrates, we selected **Ia** and **5** to evaluate their reactivity towards perfluoroalkylation computationally.

The enolate **Ia**, where the cyano moiety has been replaced with a nitro group, remained unreactive under standard reaction conditions. Geometry optimization of this enolate resulted in two energetically comparable conformations (figure 3.9) caused by steric repulsion from the nitro group to the phenyl ring.

TD-DFT calculations performed on the EDA complexes involving these conformations showed that the maximum wavelengths of absorption for both adducts are 266 and 299 nm, respectively. This result indicates that the EDA involving **Ia** does not absorb visi-

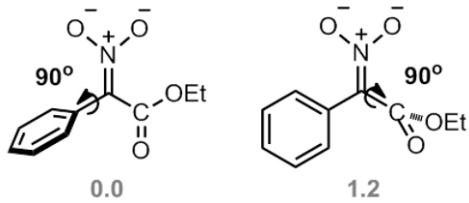

Figure 3.9: Conformations of **Ia**. Free energies in kcal.mol^{-1}.

ble light. If the initial photo-induced electron transfer does not take place, then the entire process is aborted. This significant hypsochromic shift from the EDA involving **I** is due to steric rather than electronic effects. The presence of the nitro group causes steric hindrance and breaks the planar π system, and results in 90^o rotations of the phenyl ring or the acetate group, respectively. This in turn reduces delocalization and increases the HOMO-LUMO gap, shifting the CT absorption band away from the visible range.

The other test for our computational approach was the experiment presented in figure 3.3-c, in which *para*-nitrophenyl acetate **5**, when placed under standard reaction conditions used for **1**, produces the opposite regioselectivity. That is, perfluoroalkylation takes place exclusively on the α-carbonyl and not on the aromatic ring.

Geometry optimization of the acetate **Ib** showed the same 90^o shift of the phenyl observed for **Ia**, However, despite displaying the same distortion of the planar π system, the TD-DFT calculation of enolate **Ib** showed a CT absorption band in the visible region (λ = 388 nm). The presence of a visible band absent from the **Ia** spectrum is due to the fact that the *para*-nitrophenyl is by itself a chromophore, hence this group provides the enolate with sufficient delocalization (and therefore a small HOMO-LUMO gap) to absorb visible light photons.

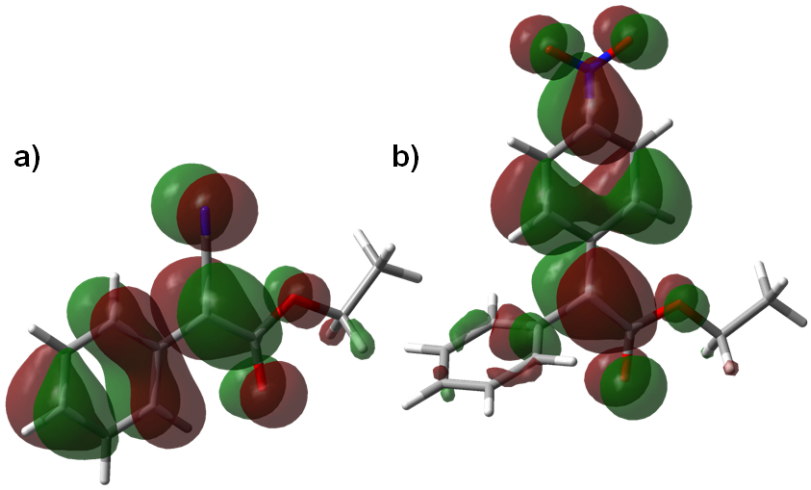

Figure 3.10: HOMO of **I** and **Ib**.

The transition state leading to the HAS product (not observed experimentally) and α-carbonyl product **6** have relative energies of 13.8 and 7.1 kcal.mol^{-1}, respectively, thus reproducing the experimentally observed product distribution. The inversion in regioselectivity compared to substrate **1** can be explained by analyzing the frontier orbitals of both enolates, specifically the HOMO of **I** and **Ib** (figure 3.10). The HOMO of **I** has significant contribution in the *para* and *ortho* positions of the phenyl ring (figure 3.10-a), which is significantly reduced in the case of **Ib** (figure 3.10-b). This small participation of the phenyl ring in the HOMO of **Ib** finds its origin in the same 90^o dihedral rotation of the arene reported above for **Ia**, which leaves the phenyl out of the planar system, and thus out of the high energy π MOs. It is worth noting that the arene in the *para*-nitrophenyl group is not susceptible to trapping $\mathbf{R}_F{}^{\bullet}$, as both *ortho* and *para* positions are affected by the resonance attractor effect of the nitro group, hence the absence of perfluoroalkylated product in the *para*-nitrophenyl ring.

Conclusion

We showed that mostly ground-state DFT calculations can provide useful information, and successfully complement experiments in the elucidation of light-driven synthetic processes. The quantum yield of the reaction, above 1 and yet low for chain processes, was properly rationalized and reproduced after treating the energy barriers emerging from the DFT results with a microkinetic model, which was critical to address the problem of large differences in concentration among key species. In addition, regioselectivity was correctly reproduced and rationalized on the basis of a distortion/interaction analysis, where its origin was identified as the greater deformation of the enolate in the transition state leading to the α-carbonyl product **4** with respect to the HAS product **3**.

Our computational approach was further confirmed by explaining the non-trivial outcomes of seemingly similar substrates, all bearing an electron-withdrawing group in the α position. Specifically, enolate **Ia** (unreactive under standard conditions) was found to lack visible light absorption bands due to steric hindrance from the nitro group, which results in a 90^o dihedral rotation of the methyl group and breaks the planar π system. As a result, the first electron transfer never takes place. In addition, the discordant regioselectivity of enolate **Ib** with respect to **I** was explained on the basis of frontier orbital analysis. This substrate shows the same 90^o dihedral distortion as **Ia**; but it still shows a CT absorption band in the visible range thanks to delocalization of the 4-nitrophenyl group. As a result, the rotation of the phenyl leaves it out of the π system, and therefore has little contribution to the HOMO, compared to the α-carbon, where

the perfluoroalkylation takes place. The use of a kinetic model to obtain information on the selectivity of a process where the standard treatment of comparing energy barriers is insufficient was shown to be a valuable tool, particularly in photoactivated processes, which are prone to involve large differences in concentration.

Part II - Dioxygen Insertion on Pt(II)-Me Bond

Functionalization of the metal-carbon bond is one of the main steps in the catalytic alkane activation process. Yet despite the extensive work on C-H activation reactions,[127, 128, 129] the subsequent functionalization of alkyl ligands into useful products remains a challenge. Therefore, significant effort has been put in recent years to employ readily available agents that can insert into the M-C bond and release the functionalized product.[130, 131, 132] In the case of alkane oxidation reactions involving organometallic Pt(II) and Pd(II) complexes, a range of oxidants have been reported, such as Cl_2,[133] $PhICl_2$, $PhI(OAc)_2$,[134] $(PhIAr)(BF_4)$,[135] $PhI(CCSiMe_3)(OTf)$,[132] RSSR,[136] and $(C_6H_4CMe_2O)ICF_3$.[137] In this regard, the ideal scenario is to insert environmentally benign oxidants such as H_2O_2 or O_2. Evidently, one of the most desirable agents for this task is atmospheric dioxygen, due to its abundance and availability. However, triplet ground state oxygen is generally difficult to trap, as it is relatively unreactive due to the fact that bond formation between ground state dioxygen and organic substrates is spin-forbidden. This restriction imposes the need for a singlet-triplet crossing on the reaction coordinate which reduces the efficiency of the process.[138]

Recently, Britovsek *et al.*[139, 140] reported that a platinum methyl complex containing a diamino-substituted terpyridine ligand inserts dioxygen upon exposure to visible light to give the methylperoxo product (Figure 3.11).

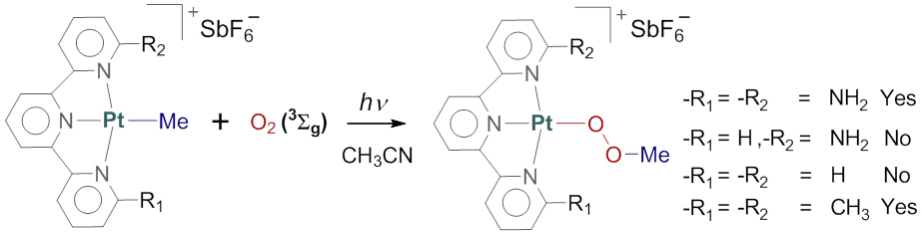

Figure 3.11: General Reaction scheme of the O_2 insertion.

One of the remarkable aspects of this reaction was the strong dependence of the insertion on the substituents in the 6 and 6' positions. Whereas the diamino-substituted complex readily inserted dioxygen, replacing one or both groups with hydrogen made the system unreactive towards insertion. However if the substituents are methyl groups, O_2 insertion does take place under reaction conditions. This reactivity is rather counter-intuitive since, unlike in the diamino-substituted case in which hydrogen bond interactions might facilitate oxygen coordination, the methyl groups represent a hindering factor towards the approach of dioxygen. This interesting aspect of the reactivity prompted us to study the reaction to gain some insights as to why substituents that constitute fundamentally different interactions can both insert dioxygen while the rather innocuous dihydrogen-substituted complex remains unreactive.

One of the most effective strategies to incorporate dioxygen without involving open shell reactivity is to sensitize it to the singlet form via excited state quenching.[141] In this process, the photosensitizer is a transition metal complex with a Metal to Ligand Charge Transfer (MLCT) excitation. This charge transfer is followed by an intersystem crossing (*ISC*) to a long-lived triplet state, which can be quenched by triplet oxygen to yield its singlet form and re-

store the ground state complex. During the evolution of the excited state to its triplet form, a vacant site can be formed in the coordination sphere for singlet oxygen to occupy and produce a stable intermediate.[142] There is evidence of Pt(II) complexes generating singlet oxygen and inserting it into the coordination sphere.[143]

To answer these questions we decided to build a working model of the reaction mechanism using the 6,6'-diaminoterpyridine Pt(II)methyl complex (**1**) as the reactant, and later test said mechanism on the other substrates used experimentally to verify our model and to elucidate the factors driving the reactivity of the system. Calculations were carried out using the M06 functional[42] with continuum solvent contributions from the Polarizable Continuum Model (PCM) as implemented in Gaussian09.[114] Geometry optimizations and TD-DFT calculations were performed using the LANL2DZ basis set with polarization function for Pt and 6-31+G(d) for light atoms (BS1). This is the level of theory for all calculations with the exception of the validation of results presented in table 3.3, where energy calculations on key stationary points were carried out using both the M06 functional and ω-B97x-D functional[47] with the 6-31++G(d) basis set for light atoms and the LANL2TZ(f) for Pt (BS2). [144, 145, 116, 117]

Generation of Singlet Oxygen

The photochemical behavior of planar Pt(II) and Pd(II) complexes with highly delocalized pyridine-type ligands has been studied in detail by computational and experimental methods, evidencing the existence of long-lived triplet states as a product of metal-to-

ligand charge transfer (MLCT) excitations.[146, 147, 148] Therefore, in our study we limited our description of the evolution of the excitation to the formation of the triplet state and subsequent relaxation to a minimum in that surface.

As a first step, we studied the absorption spectrum of **1** via a TD-DFT calculation and found a strong MLCT band with a maximum absorption at 404 nm (f=0.1343) and an even stronger one at 364 nm (f=0.2789) in good agreement with the experimental spectrum of this complex. Square planar Pt(II) complexes are known to generate singlet oxygen $O_2(^1\Delta_g)$ under photochemical conditions, provided they can form an excited triplet state above 95 kJ.mol^{-1} (22.7 kcal.mol^{-1}) to allow sufficient energy transfer to ground state $O_2(^3\Sigma_g)$. The use of this rule for a computational estimation of the capability of a complex to generate singlet oxygen has been reported.[32]

In the terpyridine complexes studied in this work, the substituents force the methyl ligand out of the plane, even in the ground state (figure 3.12). This results in the weakening of the Pt-Me bond, and facilitates the formation of the methylperoxo species. In the case of **1**, the excitation results in a triplet state with an unpaired electron in the Pt center and another in the Pt-Me anti-bonding molecular orbital ($^3\mathbf{R}$). Occupation of the σ^*_{Pt-me} molecular orbital results in a stretching of the Pt(II)-Me bond, from 2.08 to 2.12 Å. In this excited complex the methyl ligand is entirely outside the molecular plane (N-Pt-Me angle is 167 degrees for **1**, 117 for $^3\mathbf{R}$, and 180 degrees for a fully planar system). This leaves a vacant site on the Pt centre for dioxygen to coordinate.

Figure 3.12 shows the optimized geometries of both the singlet ground state and the triplet state of complex **1**. When triplet dioxy-

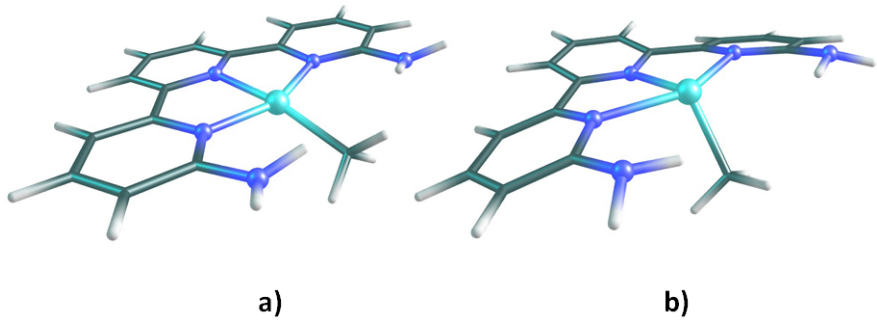

Figure 3.12: Optimized geometry of **1** in the singlet (a) and triplet (b) state.

gen coordinates to the triplet complex, the high energy system can rearrange and relax to an intermediate in which dioxygen displaces the methyl group to the apical position ($\mathbf{Int}_1$). The process of generating singlet oxygen is likely to take place in a stepwise form. This resulting intermediate is a η^2-O_2 complex which is lower in energy than free singlet oxygen. Thus, singlet oxygen generation via this complex is energetically favored. Figure 3.13 shows the stepwise formation of $\mathbf{Int}_1$, where $\mathbf{Int}_0$ corresponds to a short-lived open-shell singlet intermediate in which dioxygen is coordinated η_1.

The quenching process consists in the coordination of $\beta\beta$ dioxygen to the $\alpha\alpha$ complex, this involves the rearrangement cost of the weakened Pt(II)-Me bond to move to the apical position. However, the proper description of the closing of two open-shell singlets is beyond the capabilities of DFT methods, and we are limited to the assumption that this coordination takes place. Our assumption however is supported by indirect evidence, since the triplet state of the complex fulfils the conditions stated above for singlet oxygen generation, and $\mathbf{Int}_1$ is favored over both the excited triplet state (by 23.2 kcal.mol^{-1}) and free singlet oxygen (by 5.1 kcal.mol^{-1}). Thus,

we assumed the formation of $\mathbf{Int}_1$ and proceeded from this point to study the formation of the methylperoxo product.

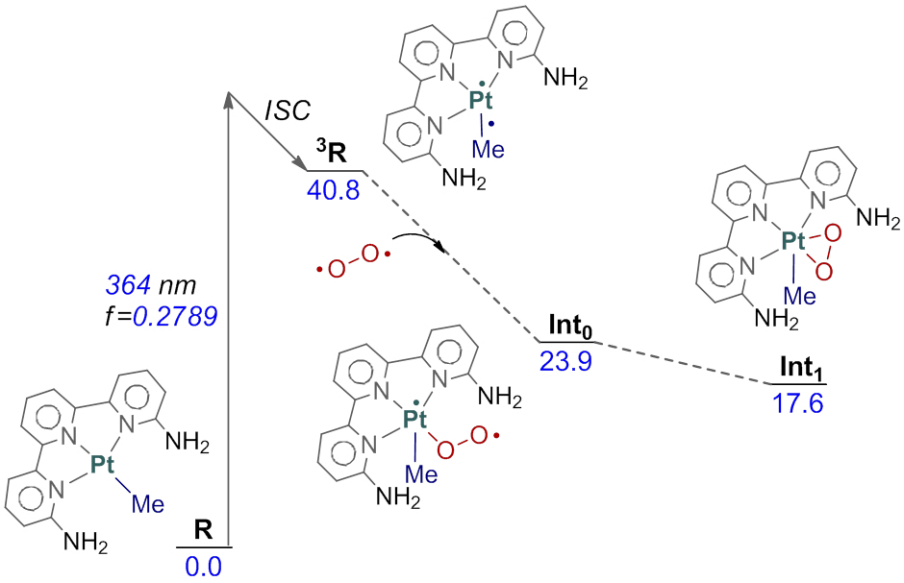

Figure 3.13: Free energy profile for the generation of singlet oxygen. Energies *vs* reactants in kcal.mol^{-1}

Migration of Methyl

The methylperoxo complex can be formed by the migration of the methyl ligand to the η^2-O_2 unit and later rearrangement to the product conformation (figure 3.14). We found a transition state in which the methyl is transferred to the nearest oxygen ($\mathbf{TS}_1$). This migration yields an intermediate in which both the methyl and the platinum are attached to the same oxygen ($\mathbf{Int}_2$). However, this intermediate is very unstable and quickly rearranges to form the methylperoxo product ($\mathbf{P}$). Alternatively, the peroxo ligand can rearrange to a η^1-O_2 configuration in which the terminal oxygen is

closer to the methyl group ($\mathbf{Int}_{1b}$). From this intermediate, the methyl ligand can migrate to the terminal oxygen ($\mathbf{TS}_{1b}$) and yield the methylperoxo, after a rotation on the O-O axis. This direct migration however, involves a higher energy transition state ($\mathbf{TS}_{1b}$). Therefore, it was not further considered as a competing mechanism. In addition, we found a transition state ($\mathbf{TS}_2$) at 48.9 kcal.mol^{-1} in which one arm of the ligand dissociates, and the rearrangement of dioxygen for methyl migration is less constrained. This transition state is not competitive for system **1** as the interaction of both ligands with dioxygen is stabilized by hydrogen bonds.

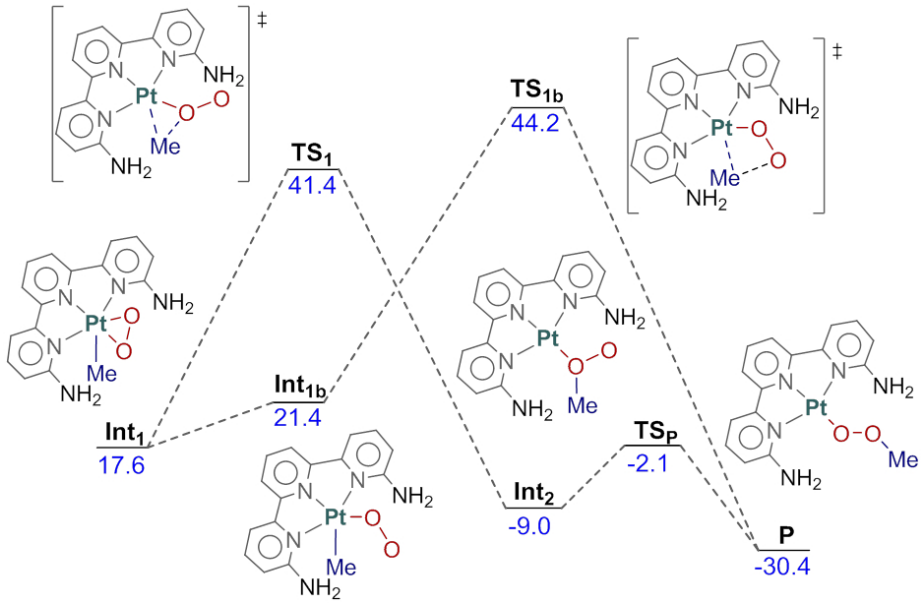

Figure 3.14: Free energy profile for the methyl migration process. Energies *vs* reactants in kcal.mol^{-1}.

Deactivation Processes

The fact that the reaction takes place in the excited state and involves high energy species and transition states, implies that there is a competition with the different unproductive deactivation processes that restore the initial ground state, which may significantly affect the final yield of the reaction. We mentioned before that the dissociation of singlet oxygen is 18.3 kcal.mol^{-1} above $\mathbf{Int}_1$ (35.9 kcal.mol^{-1} above reactants) ($\mathbf{TS}_D$). The dissociation of $O_2(^1\Delta_g)$ relaxes to an adduct between oxygen and the planar ground state complex at 33.3 kcal.mol^{-1} above reactants (**D**). The relaxation of singlet dioxygen in solution has been studied extensively in the past and involves both radiative and non-radiative decay. Therefore, in this work we used the experimental data of the singlet oxygen relaxation constant in acetonitrile ($k_{AcCN} = 1.5\text{x}10^4$ s^{-1}) to determine the energy cost of restoring ground state oxygen.[149] k_{AcCN} was used to obtain an "activation energy" of decay via Eyring's equation.

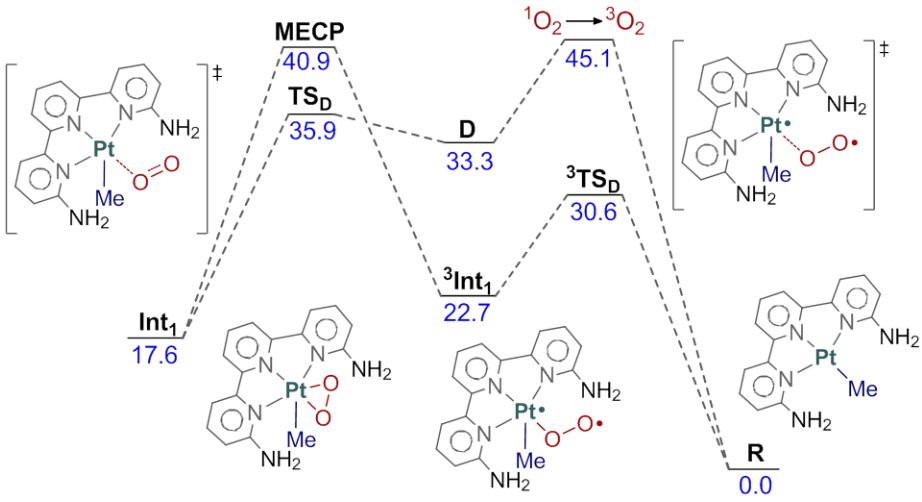

Figure 3.15: Free energy profile for the deactivation paths. Energies *vs* reactants in kcal.mol^{-1}.

In addition to the dissociation path, **Int**$_1$ can also undergo intersystem crossing to the triplet state via minimum energy crossing point (**MECP**) to a η^1-O_2 triplet complex (^{3}**Int**$_1$). This complex can easily release $O_2(^3\Sigma_g)$ through the transition state ^{3}**TS**$_D$ (30.6 kcal.mol^{-1} above reactants) and restore the ground reactant complex (Figure 3.15). Both of these deactivation pathways compete with methyl migration to determine if the formation of the methylperoxo complex takes place efficiently. In the case of complex **1**, the transition state for the migration (**TS**$_1$) is 41.4 *vs* 40.9 kcal.mol^{-1} for the **MECP**. This small difference is within the error of the method, considering we are comparing considerably different points in the potential energy surface. The dissociation of singlet oxygen and later decay is less competitive. According to Eyring equation, a rate constant of 1.5x10^4 s^{-1} corresponds to a barrier of approximately 11.8 kcal mol^{-1}. Therefore, the energy of the dissociation/decay path is $\approx$ 45.1 kcal.mol^{-1} which makes it less competitive than **MECP**.

The full reaction mechanism, including less competitive pathways is presented in figure 3.16. The formation of $\mathbf{Int}_1$ and later migration of methyl to the nearest oxygen is a plausible mechanism for the insertion of dioxygen, and reactivity is determined by competition with intersystem crossing to the ground state.

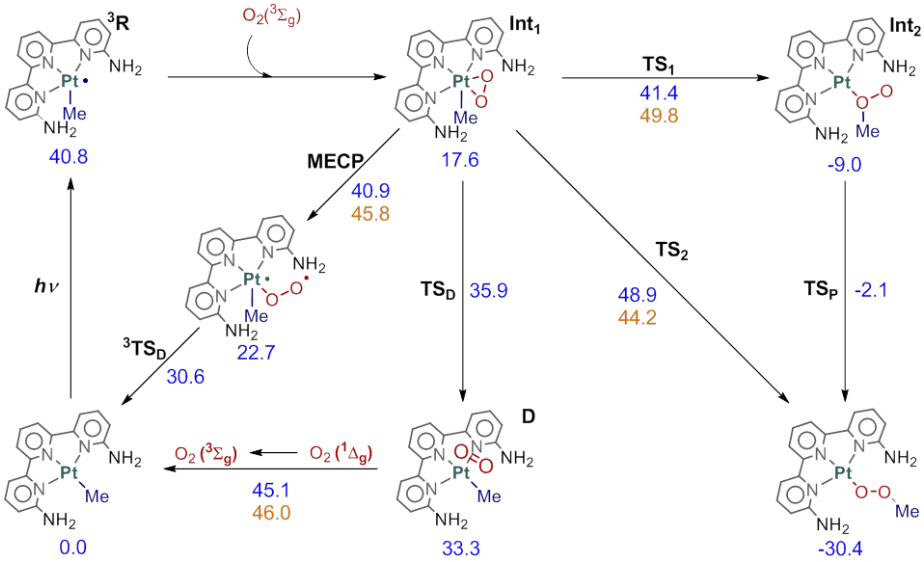

Figure 3.16: Full reaction scheme for complex **1** (blue) and key points for complex **4** (orange). Free energies *vs* reactants in kcal.mol^{-1}.

For system **1**, there are therefore five possible outcomes for the photoexcited intermediate $\mathbf{Int}_1$. The relative energies of the corresponding high energy points are 41.4 kcal.mol^{-1}, 44.2 kcal.mol^{-1} and 48.9 kcal.mol−1 for the productive transition states $\mathbf{TS}_1$, $\mathbf{TS}_1b$, and $\mathbf{TS}_2$; and 40.9 kcal.mol^{-1} and 45.1 kcal.mol^{-1} for the unproductive paths through **MECP** and singlet dioxygen relaxation. The difference of 0.5 kcal.mol^{-1} between $\mathbf{TS}_1$ and **MECP** means that $\approx 31\%$ of the photoexcited systems should evolve towards product, whith

the other 69% returning towards reactants. This results in a net observation of product formation, in agreement with experiment.

The barrier of 23.8 kcal.mol^{-1} corresponding to $\mathbf{TS}_1$ is near the limits of reactions that may take place at room temperature within a reasonable time. However, the fact that $\mathbf{Int}_1$ is the product of a nonradiative photophysical transformation means that most systems will be in an excited vibrational state, which is analogous to being at a higher temperature. Thus, the barrier may be easier to overcome for $\mathbf{Int}_1$ than for an equivalent system in the ground state.

Reactivity of Disubstituted Terpyridine Complexes

In order to check if the mechanism correctly reproduces experimental results, we decided to test our model by calculating the key stages and stationary points in the mechanism on all Pt(II) complexes shown in figure 3.11. These complexes differ only in the substituents on the 6,6' positions of the terpyridine ligand. They are 6-amino terpyridine (**2**), unsubstituted terpyridine (**3**), and 6,6'-dimethyl pyridine (**4**).

As with **1**, we began by studying the photochemical behavior of these complexes using TD-DFT calculations. The vertical spectrum of **2** showed a single MLCT band with strong maximum absorption at 357 nm (f=0.2245) in close agreement with experiments, while **3** showed only a weak π-π^* band at 358 nm (f=0.0227) and a very strong band completely outside of the visible range, at 316 nm (f=0.3996), also in agreement with experiments. This suggests that **3** does not form the excited triplet intermediate under sunlight

conditions, which is a plausible explanation for the fact that it does not insert dioxygen under reaction conditions.

On the other hand, the spectrum of **4** was also reproduced with a somewhat weak MLCT band at 347 nm (f=0.0506) and stronger one, also MLCT, near the visible frontier at 330 nm (f=0.3604).

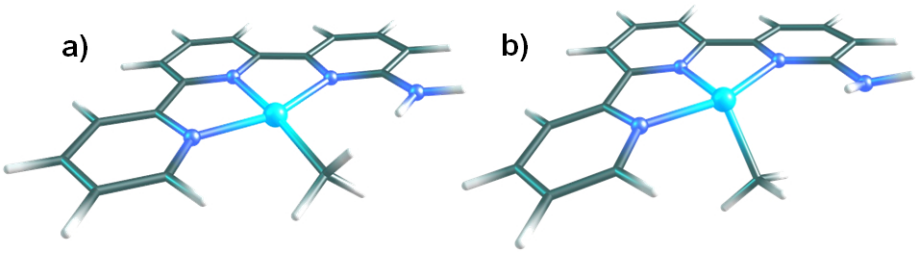

Figure 3.17: Optimized geometry of **2** in the planar triplet state (a) and distorted triplet state (b).

Optimization of the triplet state geometry of these complexes with respect to reactants varies considerably. In the case of **2**, relaxation of ^{3}**R** from the Franck-Condon geometry (*i.e.*, the geometry of the singlet complex) does not distort the square planar system, and the spin density is delocalized in the ligand system rather than the metal-methyl bond (figure 3.17-a). However, the distorted triplet state of this complex can also be located (figure 3.17-b), at a lower energy (45.0 *vs* 49.9 kcal.mol^{-1}). Our methods cannot discriminate which triplet state is formed upon evolution of the excited state. However, it is likely that they exist in equilibrium. Thus, we assumed **2** forms the reactive triplet state and evaluate whether methyl migration takes place.

Triplet state **4** shows the same severe distortion of the plane as **1**, with N-Pt-Me angle of 117 degrees (figure 3.18-a). Finally, the geometry of triplet **3** was also optimized even though the com-

plex shows no MLCT band in the visible range, to observe whether the lack of substituents has an effect on the triplet geometry. The minimized geometry shows an N-Pt-Me angle of 134 degrees (figure 3.18-b), which is significantly distorted but the Pt-Me distance remains unchanged (2.08 Å).

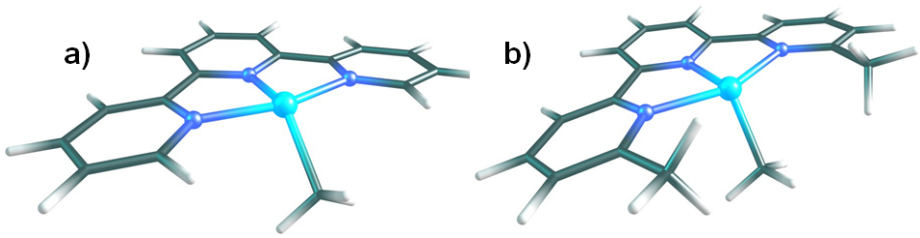

Figure 3.18: Optimized geometry of the triplet state of **3** (a) and **4** (b).

Concerning the energies of triplet state complexes, **1** and **4** have triplet energies of 40.8 and 35.5 kcal.mol^{-1}, respectively, whereas **2** and **3** have higher energies at 45.0 (distorted form) and 45.9 kcal.mol^{-1}, respectively. The fact that these differences in the triplet state geometries and energies of the reacting complexes follow the same trend as their capacity to insert dioxygen might be coincidental, but it can also mean that the formation of $\mathbf{Int}_1$ depends on these factors. As stated above, the proper description of the singlet oxygen generation step is beyond the capabilities of DFT methods, so we treated the formation of $\mathbf{Int}_1$ as a given for complexes **1**, **2** and **4**, and evaluated the effect of these substituents in the migration of methyl. The migration of methyl was also studied for triplet **3** to gain insights into the substituent effects.

The results are collected in table 3.2. In the case of complex **2**, our calculations showed that the **MECP** is largely unaffected by the substitution of one -NH_2 group for hydrogen. However, the

energy of $\mathbf{TS}_1$ increases 2.4 kcal.mol^{-1} with respect to **1**. This energy difference can be rationalized in terms of the configuration dioxygen adopts in $\mathbf{TS}_1$ (figure 3.19-a). Here the η^2 coordination is broken and the oxygen that remains bound to the Pt(II) adopts a tetrahedral configuration with a vacancy for the methyl to occupy. In the case of **1**, this configuration is assisted by hydrogen bonding interactions from both -NH_2 groups (one with each oxygen) which stabilizes the migration. In the case of **2**, the absence of one -NH_2 group predictably raises the energy of $\mathbf{TS}_1$. This trend is followed by **3**, where $\mathbf{TS}_1$ goes up in energy 2.5 kcal.mol^{-1} more due to the absence of the second -NH_2. The energy of **MECP** also increases but this is true of all stationary points involving this complex, as the coordination of dioxygen is less favored in the first place. The energy difference between $\mathbf{TS}_1$ and **MECP** for **3** is rather low (0.8 kcal.mol^{-1}), just a fraction higher than for **1**. This result suggests that **3** might insert dioxygen if the MLCT state is populated under higher energy irradiation.

Table 3.2: Key steps of dioxygen insertion for each complex. Relative free energies in kcal.mol^{-1}

System	Photo[a]	ΔG_{TS}	$\Delta G_{\mathbf{MECP}}$	Diff[b]	Prod[c]	Reacts
$\mathbf{1/TS}_1$	Yes	41.4	40.9	0.5	31:69	Yes
$\mathbf{2/TS}_1$	Yes	43.8	40.8	3.0	1:99	No
$\mathbf{3/TS}_1$	No	45.1	44.3	0.8	19:81	No
$\mathbf{4/TS}_2$	Yes	44.2	45.8	4.0	83:17	Yes

[a] Absorbs visible light; [b] Energy Difference; [c] Distribution of productive excitations;

The case of **4** follows the same trend as all previous complexes. That is, whereas removing hydrogen bonding interactions increases

the energy of $\mathbf{TS}_1$, substitution of -NH_2 groups by methyl cause steric hindering effects on the rearrangement of oxygen, and significantly raise the energy of $\mathbf{TS}_1$ (49.8 kcal.mol^{-1}). This effect is also present in the **MECP** to a lesser extent following the trend shown for the other three complexes.

The results show that the mechanism that describes the reactivity towards insertion of complexes **1** and **2** (*i.e.*, $\mathbf{TS}_1$), fails to explain the fact that complex **4** also inserts dioxygen. $\mathbf{TS}_1$ is above the **MECP** in energy, and also above the dissociation/decay path for this complex (46.0 kcal.mol^{-1}). The direct formation of **P** via $\mathbf{TS}_{1b}$ is also noncompetitive (53.5 kcal.mol^{-1}). However, here $\mathbf{TS}_2$ becomes competitive by relieving the steric repulsion caused by one methyl group in the ligand. The energy of $\mathbf{TS}_2$ for system **4** is 44.2 kcal.mol^{-1} (figure 3.19-b). This transition state is lower in energy than both deactivation pathways, thus it explains the fact that **4** can insert dioxygen under reaction conditions.

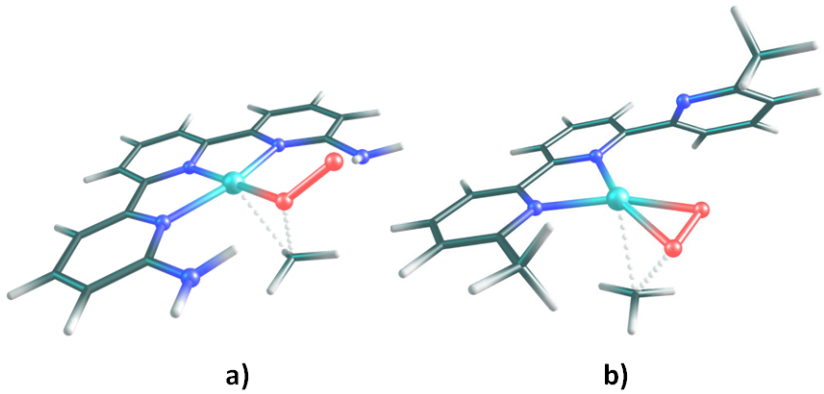

Figure 3.19: Optimized geometries of $\mathbf{TS}_1$ (a) and $\mathbf{TS}_2$ (b).

It is worth noting that $\mathbf{TS}_2$ is higher in energy than $\mathbf{TS}_1$ for all other substrates (48.9 for **1**, 51.2 for **2**, and 55.5 for **3**, all in

kcal.mol^{-1}), hence it is only competitive in the case of **4**. Since the energy differences that define the reactivity of these complexes are sometimes very small, single-point calculations of the key competing steps were calculated using a larger basis set (BS2) to see if the trends are robust. In addition, calculations were repeated using the ω-B97x-D functional with BS2 to see if the trends were method dependent. The results are collected in table 3.3, where both functionals showed the correct trend using the large basis set. Therefore, our mechanism qualitatively reproduces the experimental results.

Table 3.3: Energy difference between $\mathbf{TS}_1/\mathbf{TS}_2$ and **MECP**. Relative free energies in kcal.mol^{-1}

Complex/TS	M06/BS1	M06/BS2	ω-B97x-D/BS2	Inserts O_2
$\mathbf{1}/\mathbf{TS}_1$	0.5	1.0	-0.3	Yes
$\mathbf{2}/\mathbf{TS}_1$	3.0	4.1	8.1	No
$\mathbf{3}/\mathbf{TS}_1$	1.8	4.0	8.1	No
$\mathbf{4}/\mathbf{TS}_2$	-1.6	-0.9	-1.6	Yes

Bimolecular formation of Pt(II)-dioxygen complex

Britovsek *et al.*[139] proposed a mechanism in which two reactant complexes form a Pt$\cdots$Pt dimer which absorbs visible light to form a Pt(III)$\cdots$Pt(III) triplet species (figure 3.20). Here dioxygen can coordinate and later displace the methyl group to the apical position to reach the bimolecular form of $\mathbf{Int}_1$; from this point the formation of the methylperoxo complex is assumed to be straightforward.

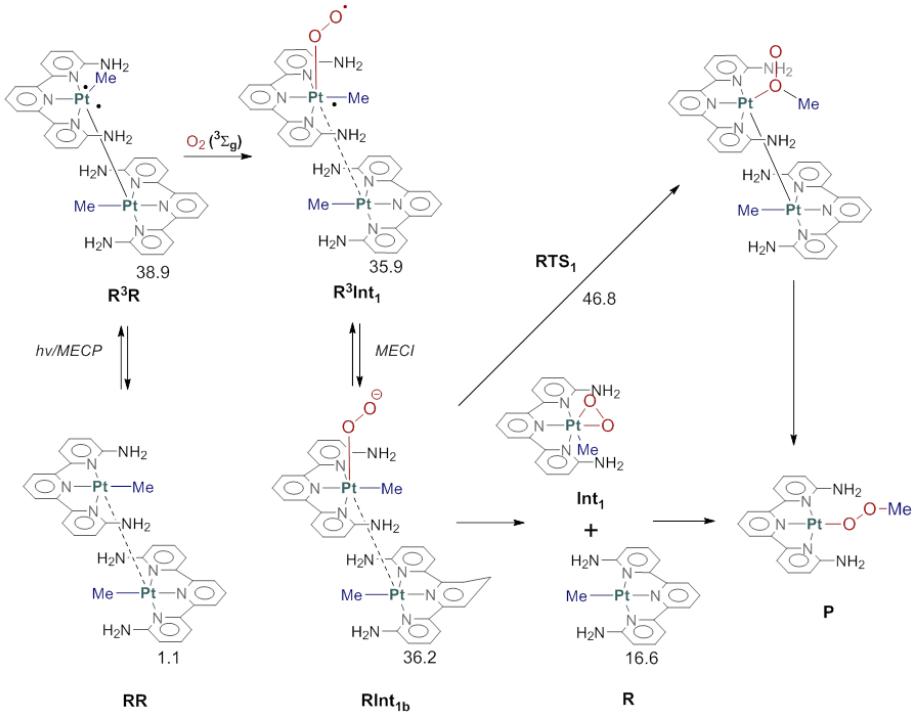

Figure 3.20: Mechanism for the formation of **Int**$_1$ proposed by Britovsek *et al.*

We carried out calculations on this mechanism to see if we could discriminate the most plausible path for the formation of the Pt(II)-O bond. For reasons of computational cost, we reduced the basis set used for light atoms to 6-31G(d). We found a bimolecular system in which the Pt-Pt distance is 3.67 Åat 1.1 kcal.mol^{-1} above separated reactants. TD-DFT calculation on the bimolecular complex showed a similar behavior to that of the monomer, with strong MLCT bands at each Pt center, but no significant charge transfer band involving both fragments. Relaxation of the triplet state led to a dinuclear complex (38.9 kcal.mol^{-1}) with Pt-Pt distance of 2.88 Åwhich basically consists of a triplet complex and a singlet one, with the distorted Pt(II)-Me bond pointing out of the dimer ($\mathbf{R}^3\mathbf{R}$).

The approach of dioxygen to this triplet dimer produces a high energy Pt-O_2 complex (35.9 kcal.mol^{-1} open-shell singlet ($\mathbf{R}^3\mathbf{Int}_1$ and 36.2 kcal.mol^{-1} closed-shell $\mathbf{RInt}_{1b}$). This intermediate can either dissociate to form $\mathbf{Int}_1$ or undergo methyl migration with a significantly higher barrier ($\mathbf{RTS}_1$ at 46.8 kcal.mol^{-1} *vs* $\mathbf{TS}_1$ 41.4 kcal.mol^{-1}). Our methods are not able to discriminate whether the relaxation of the excited state to the triplet form requires the presence of a second complex in the form of a dimer, but once a triplet complex is formed, the presence of a second complex plays no role in the mechanism. In fact, it constitutes a penalty from the entropy cost of having two fragments locked together rather than moving freely. Therefore, we can say that the unimolecular mechanism is a more plausible path for dioxygen insertion that the bimolecular one.

Alternative Mechanism: Direct O-Me bond formation

For the sake of completeness, in addition to the methyl migration shown above, we also studied a mechanism in which triplet dioxygen directly attacks the weakly bonded methyl in the triplet complex. The mechanism bifurcates from the previous one after the formation of $^3\mathbf{R}$, and thus competes with the formation of $\mathbf{Int}_1$. This attack involves an inner-sphere single electron transfer in which the Pt-Me bond undergoes homolytic dissociation. The resulting fragments are a tricoordinated Pt complex and methylperoxo radical. Both fragments can combine without a significant barrier to yield the product directly. Figure 3.21 shows the energy profile of this alternative mechanism for all complexes. This alternative mechanism shows a significantly smaller energy barrier than methyl migration. However, it has some important issues. The first problem with this mechanism is that we cannot compare $\mathbf{TS}_3$ with the energy cost of forming $\mathbf{Int}_1$ since the latter requires a multiconfigurational description of the wavefunction (that is, a state which is part closed-shell singlet and open-shell singlet).

The other problem is that while the energies of $\mathbf{TS}_3$ are in good agreement with the experimental trends observed, the energy barriers of said transition states are inverted for complexes **1** and **2**, compared to the experimental results. For this mechanism to properly describe the trends found experimentally, **2** must never form the distorted triplet state, as optimization of the Franck-Condon geometry might indicate. However, as we mentioned before there are no indications as to whether the distorted triplet geometry of **2**

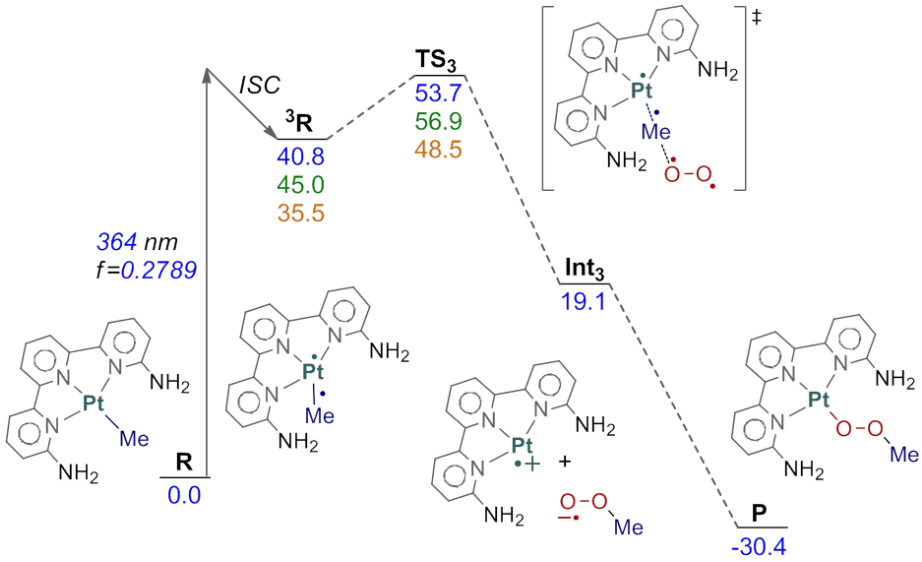

Figure 3.21: Free energy profile for the direct methylperoxo formation. Energies in kcal.mol^{-1} for **1** (blue), **2** (green) and **4** (orange).

is inhibited, or whether formation of $\mathbf{Int}_1$ has a higher energy cost than $\mathbf{TS}_3$. Therefore, methyl migration remains the most plausible mechanism according to our calculations.

Conclusion

We have studied the mechanism for the light-driven insertion of dioxygen into the Pt(II)-Me bond of planar [Pt(terpyridine)Me]$^+$ complexes using ground state DFT and TD-DFT methods. The generation of singlet oxygen was rationalized on the basis of the photochemical behavior of the complex upon absorption of visible light, as the relaxation of the triplet state that follows the excitation leads to the formation of a vacant site in the Pt(II) coordination sphere. The resulting excited complex has one unpaired electron in the Pt and the other in the anti-bonding Pt-Me σ orbital, thus the approach of dioxygen involves the stepwise closing of two open-shell singlets that results in the η^2-O_2 closed-shell intermediate $\mathbf{Int}_1$. The formation of the methylperoxo product was shown to depend on the competition between the migration of methyl from Pt to oxygen and photophysical decay to the reactants via intersystem crossing to the triplet state from which ground state dioxygen readily dissociates. This computational mechanism was tested and confirmed by reproducing the reactivity of other Pt(II)Me complexes studied experimentally.

The strong dependence of the reaction on the terpyridine substituents shown experimentally was explained as the capability of said substituents to facilitate the configuration necessary for methyl migration. In this regard, substituents that can form hydrogen bonds with the η^2-O_2 ligand assist the migration by stabilizing the transition state ($\mathbf{TS}_1$) *vs* intersystem crossing (**MECP**) to the ground state. On the other hand, substituents that cause steric hindrance to the η^2-O_2 ligand react via a different path ($\mathbf{TS}_2$), in which

an arm of the terpyridine ligand dissociates to allow oxygen to rearrange, thus enabling the migration. This path is only competitive in the case of hindering substituents, in which **MECP** is also high in energy.

In addition, we carried out calculations on the preliminary mechanism proposed by Britovsek *et al.* This mechanism consisted in the formation of a dimer which can absorb visible light to yield a Pt(III)$\cdots$Pt(III) complex where dioxygen can coordinate, and later rearrange to yield the methylperoxo product. Our calculations found that the bimolecular mechanism follows a very similar path to our unimolecular model, where the second complex plays no apparent role in the reaction once the triplet state complex is formed.

Finally, we studied an alternative mechanism which takes place in the open-shell singlet surface. In this mechanism, ground state dioxygen attacks the weakly bonded methyl ligand in the triplet state complex to generate two charged fragments: methylperoxo radical and tricoordinated cationic Pt(II) complex, which readily combine to form the methylperoxo product. According to straightforward energy barrier comparison, this mechanism shows an incorrect trend compared to experiments.

Chapter 4

Photocatalyzed Reactions

Part I - C-H Arylation of Amines

The direct arylation of α-amine sp^3 C-H bonds is a process of significant synthetic potential, as it leads to the formation of α-aryl amine products of industrial importance.[150, 151, 152] Many strategies have been developed for this reaction involving transition metal catalysts containing Cu,[153] Pd,[154], Fe,[155] and Ru.[156] Moreover, several photochemical methods were designed as well, although most required high energy light and where prone to undesired byproducts. [157, 158, 159] One of the strategies frequently used to avoid the high energy light problem is to rely on a photosensitizer to induce the reaction.[160] The use of organometallic photosensitizers to induce carbon-carbon bond formation has been a common strategy in recent years for the controlled synthesis of organic molecules.[2] In particular, cyclometallated octahedral complexes of

Ru and Ir are frequently used to induce single electron transfer (SET) and catalyze a myriad of industrially relevant processes.[161] However, the efficiency of photoredox catalyzed reactions is often reduced by the need to use sacrificial quenching agents to restore the photosensitizer to its original form.[1, 162]

In 2011, MacMillan *et al.* developed a strategy for the photoredox catalyzed α-arylation of amines which does not use a sacrificial quenching agent (Figure 4.1).[163] This strategy took advantage of the high reduction potential of excited $Ir^{III}(ppy)_3$ which can induce SET to an electron-deficient arene. The resulting Ir^{IV} displays high oxidation potential and takes an electron from the tertiary amine via a second SET. Finally, both radicals form the sp^2-sp^3 C-C bond and yield the desired α-aryl amine.

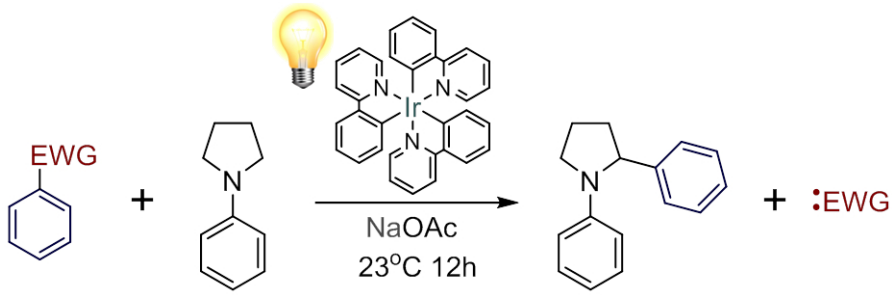

Figure 4.1: General reaction scheme of the C-H arylation.

We set out to study the reaction mechanism to test if an entirely computational approach could reproduce experimental results in a reaction involving non-conventional aspects such as excited states, outer-sphere electron transfer, or free radical chemistry. To this end we used a combination of DFT methods and kinetic simulations to account for non-trivial kinetics. We chose N-phenylpyrrolidine as the amine (**1**) and 1,4-dicyanobenzene as

electron efficient arene (**a**) to build our working model (96% yield, 12h), and later tested the model by changing the arene to *para*-cyanopyridine (**b** 72% yield, 12h) and *ortho*-cyanopyridine (**c** 26% yield 24h). Geometry optimizations and frequency calculations were carried out using the M06 functional,[42] with the LANL2DZ basis set with ECP and polarization "f" type function (coeff.=0.938) for Ir and 6-31+G(d) for light atoms.[145, 116, 117] Solvent contributions of N,N-dimethylacetamide (DMA ϵ=w37.781) were added via the SMD model as implemented in Gaussian09,[53] and potential energies were corrected using the 6-311+G(d,p) basis set for light atoms.[116, 117] Singlet electron transfer barriers were estimated using the method described in chapter 2. Finally, kinetic simulations were carried out using the Acuchem software.[119]

Reaction Mechanism

MacMillan *et al.* proposed a mechanism (figure 4.2 where EWG stands for electron-withdrawing group, in this case cyanide) which started with photoinduced electron transfer (PET). That is, light absorption by the photosensitizer (**3**) to form the triplet state excited complex **4** and subsequent SET to (**2**) to form the anionic radical **5** and the cationic complex (**Ir(6**). This first step is followed by SET from the amine (**1**) quenching agent to restore the photocatalyst and form the cationic amine radical **7**, which can transfer a proton to the base (OAc) to from a neutral radical (**8**). Then, both radicals can form the C-C bond and generate an sp^3 intermediate (**9**) that can lose a cyanide group to yield the aryl amine product **10**. We used this mechanism as the basis for our calculations.

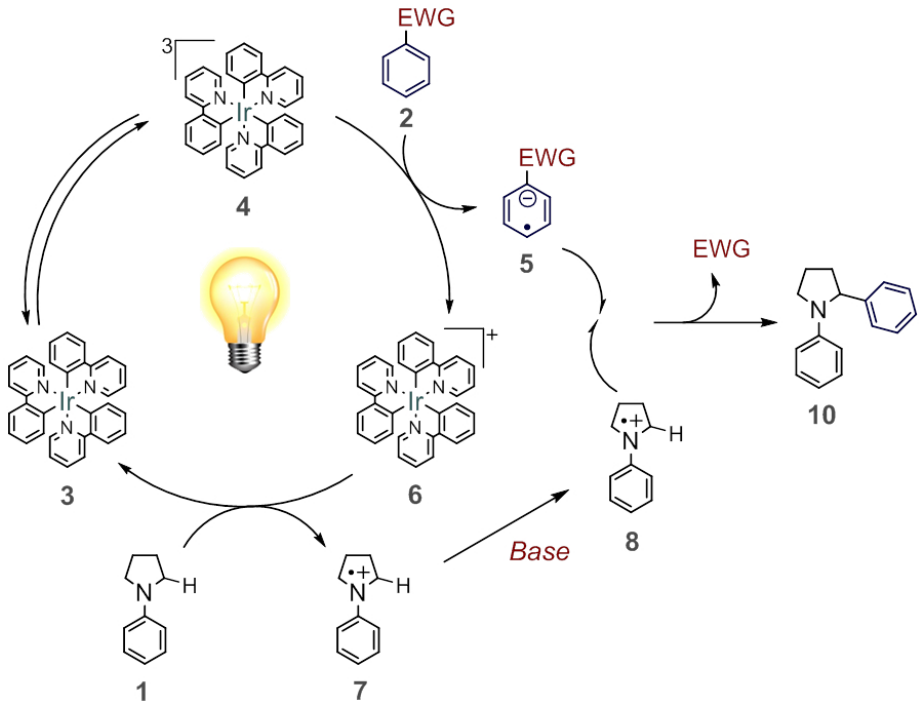

Figure 4.2: Preliminary reaction mechanism.

The photochemical behavior of $Ir(ppy)_3$ has been widely studied both theoretically and experimentally,[164, 165, 166, 167] and it is established that the complex displays a MLCT band (λ_max = 519 nm in CH_2Cl_2) followed by intersystem crossing to a triplet state where one unpaired electron is in the metal center and the other in the π ligand system. We carried out a TD-DFT calculation of **3**, and correctly reproduced the MLCT band at 540 nm in DMA. Relaxation of the triplet state **4** showed that both SOMOs correctly correspond to the MLCT transition shown in figure figure 4.3. Delocalization of the electron in the π ligand system is likely to take place in one of the ppy ligands. However, the corresponding KSMO (figure 4.3-b) is fully delocalized across the ligand system. Still, the

contribution of the metal has virtually vanished in comparison to the other KSMO (figure 4.3-a).

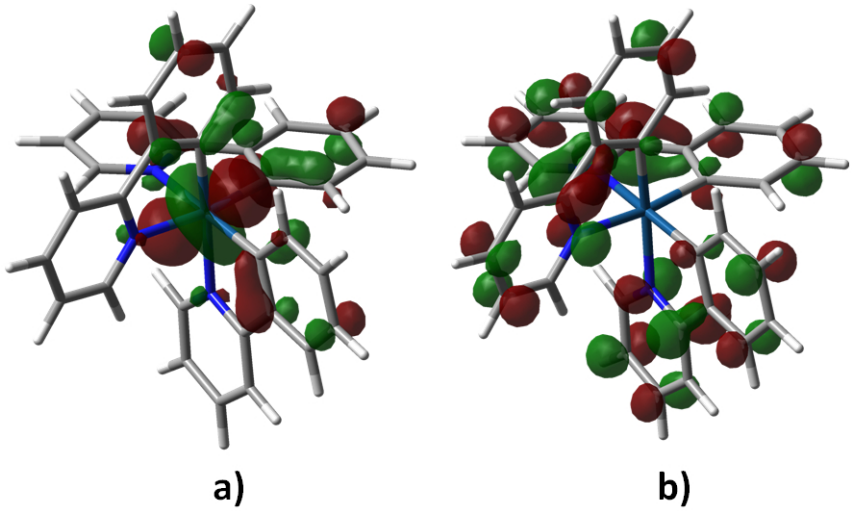

Figure 4.3: HOMO and LUMO of **3**.

Calculations on the preliminary mechanism found low energy barriers and favorable energies for all steps. Figure 4.4 shows the free energy profile for the process. **4** was selected as the referential zero to facilitate the interpretation of energy differences, as all steps following the formation of **4** involve thermal activation and can be compared directly. The energy profile shows only low barriers as indicative of a fast thermal process after PET.

The first electron transfer (from **4** to **2**) is followed by the second transfer from **1** to the cationic **6**, both with low energy barriers (6.4 and 7.1 kcal.mol^{-1}, for $\mathbf{ET}_1$ and $\mathbf{ET}_2$, respectively). However, in addition to $\mathbf{ET}_2$, **6** can also take the electron from the recently formed radical anion **5** and restore the ground state reactants ($\mathbf{ET}_3$). The barrier for the back SET to restore reactants is very low (2.2 kcal.mol^{-1}).

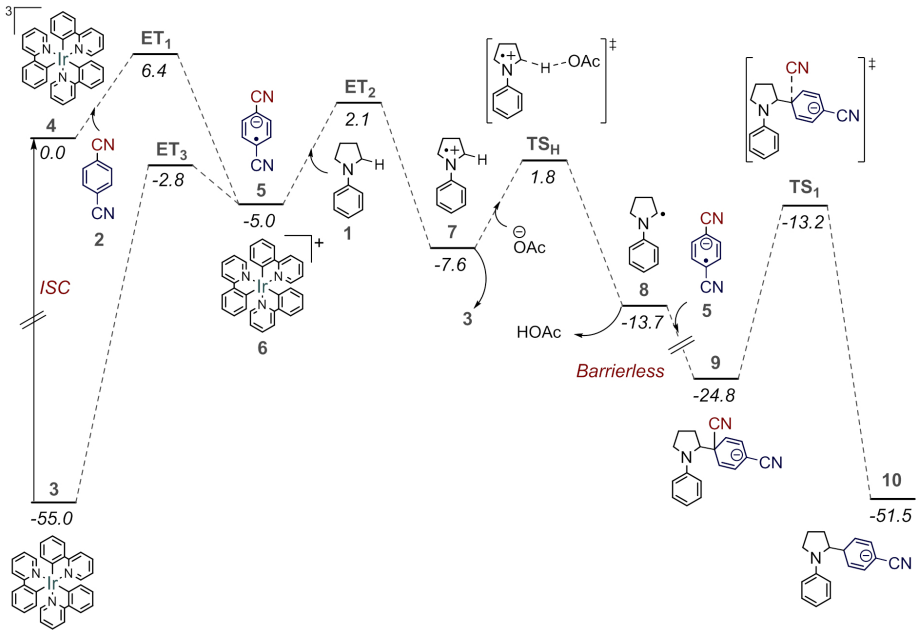

Figure 4.4: Free energy profile of the reaction with 1,4-dicyanobenzene (**a**). Energies in kcal.mol^{-1}.

According to Marcus theory, the more favorable a process the lower the ET barrier, within a certain limit.[84] In the case of $\mathbf{ET}_3$, reactants are 50.0 kcal.mol^{-1} below **5**, hence the barrier is significantly lower than $\mathbf{ET}_2$ ($\Delta G^{\ddagger}_{\mathbf{ET}_3} = 2.2$ kcal.mol^{-1}). On the other hand, he concentration of **5** is much smaller than that of **1**, so the deactivation pathway does not necessarily prevent the formation of the amine radical **7**. However, as **1** is consumed, the low energy barrier of $\mathbf{ET}_3$ has an impact on the yield of the reaction. Considerations on whether **5** is formed near the complex **6** after $\mathbf{ET}_1$ concern the pre-exponential part of the rate equation, and are therefore not taken into account at this point. This point is discussed in more detail when we look at other substrates.

After the formation of **7**, fast deprotonation by acetate leads

to the neutral radical **8**, in which the α-carbon has a vacancy to form C-C bond with **5**. DFT methods cannot calculate the transition state for the closing of two open shells, due to the presence of multiple electronic configurations involved. However, his step is expected to be near barrierless, with diffusion-driven kinetics as radical combination usually is.[120] Finally, the energy barrier of cyanide dissociation is 11.6 kcal.mol^{-1}, and constitutes the highest energy cost in the thermal part of the mechanism.

It may seem surprising that such a long reaction time is required for a system involving barriers which are so low. But one must take into account the overall efficiency of the electron transfer processes in the early stages of the reaction. The competition between the forward productive path through $\mathbf{ET}_2$ and the backward unproductive path via $\mathbf{ET}_3$ is very much in favor of the unproductive path, in particular by 4.9 kcal.mol^{-1}. This means that only a very small fraction of the photons absorbed will yield an efficient reaction. As 3 is a very efficient photosensitizer, this is consistent with the observation of long reaction times. The main validation of our model will come in any case from its treatment of modifications in the reactant.

Reaction with Cyanopyridines

We carried out calculations on arenes **b** and **c** (72% yield in 12h, and 26% yield in 24h). Figure 4.5 shows the energy profile for both pyridines. The overall picture is similar to that for dicyanobenzene (**a**), thus in principle compatible with experiments, as the reaction proceeds for the three systems. But the calculations do not seem, at first sight, to reproduce the reported reactivity trends. The bar-

rier from **9** to $\mathbf{TS}_1$, which was the highest for system **a**, is lower for systems **b** and **c**, which are less reactive. Even if this step is not the highest energy barrier for either pyridine, the formation of **9** is irreversible for all substrates, so the yields cannot be rationalized by looking at $\mathbf{TS}_1$. The energies of $\mathbf{ET}_1$ do follow the correct trend shown by experiments. However, this barrier is still easily surmountable for all three arenes, so there is no evidence that this step alone accounts for the difference in yield. Neither do the barriers for $\mathbf{ET}_2$ and $\mathbf{ET}_3$, as they are the same for all arenes. Therefore, a direct comparison of energy barriers from any reference point fails to account for the difference in yields found experimentally.

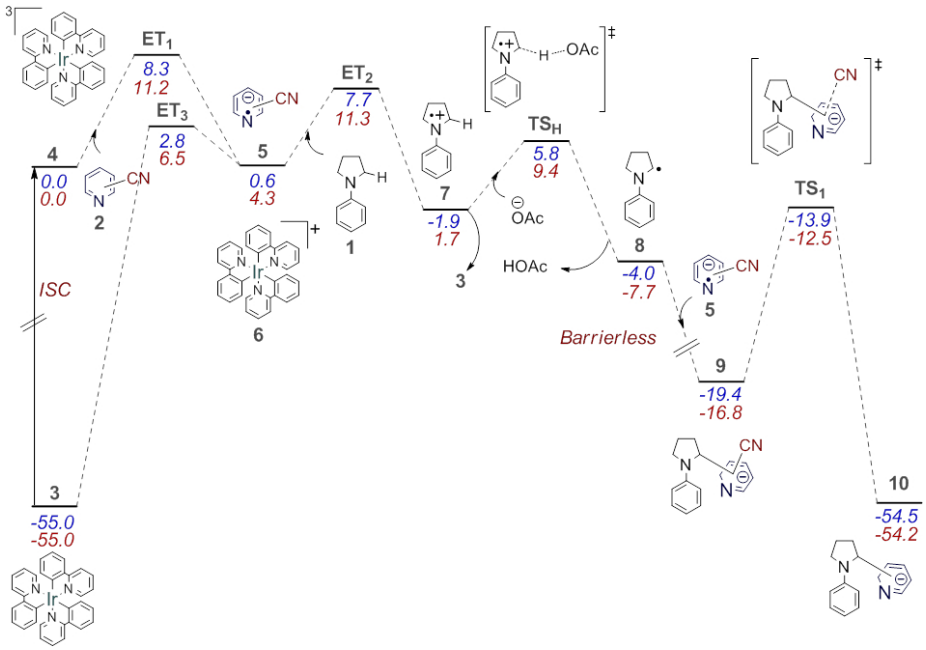

Figure 4.5: Free energy profile of the reaction with *para*-cyanopyridine (**b** blue) and *ortho*-cyanopyridine (**c** red). Energies in kcal.mol^{-1}.

Kinetic Simulations

As previously mentioned, in order to gain a full picture of the reaction mechanism and the origin of different reactivity observed for very similar substrates, several additional factors beyond energy barriers need to be considered. These factors include the deactivation of the cycle via $\mathbf{ET}_3$, and the large difference in concentrations between competing intermediates in the cycle. Thus, in order to confirm that our mechanistic model correctly accounts for the differences in yield, we built a microkinetic model based on the reaction steps presented in the energy profiles. Rate constants were calculated using Eyring's equation for the steps presented below:

1. $\mathbf{3} \overset{K_\nu}{\rightleftharpoons} \mathbf{4}$
2. $\mathbf{4} + \mathbf{2} \xrightarrow{k_1} \mathbf{5} + \mathbf{6}$
3. $\mathbf{6} + \mathbf{5} \xrightarrow{k_{-1}} \mathbf{3} + \mathbf{2}$
4. $\mathbf{6} + \mathbf{1} \xrightarrow{k_2} \mathbf{3} + \mathbf{7}$
5. $\mathbf{7} \underset{\text{base}}{\overset{k_H}{\rightleftharpoons}} \mathbf{8}$
6. $\mathbf{8} + \mathbf{5} \xrightarrow{k_3} \mathbf{9}$
7. $\mathbf{9} \xrightarrow{k_4} \mathbf{10}$

There are many processes that influence the formation of the triplet state complex **4**, including nonradiative and radiative decay (this complex displays both fluorescence and phosphorescence), as well as intersystem crossing.[165] A proper quantitative description of these photophysical transformations is well beyond the scope of

our study. Therefore, we took advantage of the fact that K_ν is the same value for all arenes and decided to perform a comparative kinetic study. That is, to adjust the value of K_ν to reproduce the yield of **b** in the experimental time (12h), and use the adjusted value of K_ν to obtain the theoretical yield of the other two arenes. This adjusted value of K_ν was used to see if the yields of **a** and **c** were reproduced with a small error. If so, then our model accurately describes the kinetics of the reaction.

The rate constant for the barrierless C-C bond formation (k_3) was assumed as diffusion-controlled so we used the value for the combination of free radicals in solution ($k_3 = 1x10^{10}$) and this value was used for all substrates, as they are similar in both size and charge. Finally, the pre-exponential part of the SET rate constants is much smaller than that of Eyring's equation for bimolecular processes. However, any error on the pre-exponential term affects the rate constant linearly, hence it is already considered in the adjustment of K_ν and gets canceled out as the yields are being compared with each other.

Table 4.1 shows the calculated yields for all arenes using a value of 8.8x10^{-3} M^{-1} s^{-1} for K_ν. Calculated yields are in qualitative agreement with experimental results, confirming our mechanism as a plausible pathway for the reaction. However, quantitative agreement is not very good, considering we are comparing relative yields and the approximations made are common to all arenes. The overall error in energy for the **c** simulation is $\approx +1.5$ kcal.mol^{-1}, which suggests that the formation of **5** for the pyridines is not as disfavoured as our calculations predict, and the agreement can be improved.

The most striking difference in the behavior of the substrates,

Table 4.1: Experimental and calculated yields for **a**, **b** and **c** using 8.8×10^{-3}mol.s^{-1}.L^{-1} as k_ν.

Arene	Exp. yield (%)	Calc. yield (%)	Time (h)
a	96	100[a]	12
b	72	72[b]	12
c	26	2	24

[a] At 9 hours; [b] Adjusted to fit Exp.

and the likely cause of their difference in reactivity, is the relative stability of their anionic forms (*i.e.*, their reduction potentials). The electron transfer from **4** to **2** is exoergic for substrate **a** (-5.0 kcal.mol^{-1}), nearly isoergic for substrate **b** (0.6 kcal.mol^{-1}), and endoergic for **c** (2.8 kcal.mol^{-1}). This difference may be attributed to their relative capacity to stabilize an extra electron in the π system.

Role of the Counterion

To address the error in energy for the formation of **5** we looked at the possible ion pairs that could be formed in the medium to stabilize the anion. The counterion of the base (Na^+) can interact favourably with **5** in the case of the pyridines (**5**b$\cdots Na^+$ is favoured by 1.4 kcal.mol^{-1} and **5**c$\cdots Na^+$ by 0.8 over the dissociated ions).

This is not true for **a** as the impact of adding the cation is diminished by the presence of two cyanide groups that can stabilize the negative charge (**5**a$\cdots Na^+$ is 1.0 kcal.mol^{-1} above dissociated ions), hence electrostatic interaction is not enough to compensate for the entropic penalty of bringing the ions together. Figure 4.6 shows the free energy profile for the Na-assisted reaction for both pyridines.

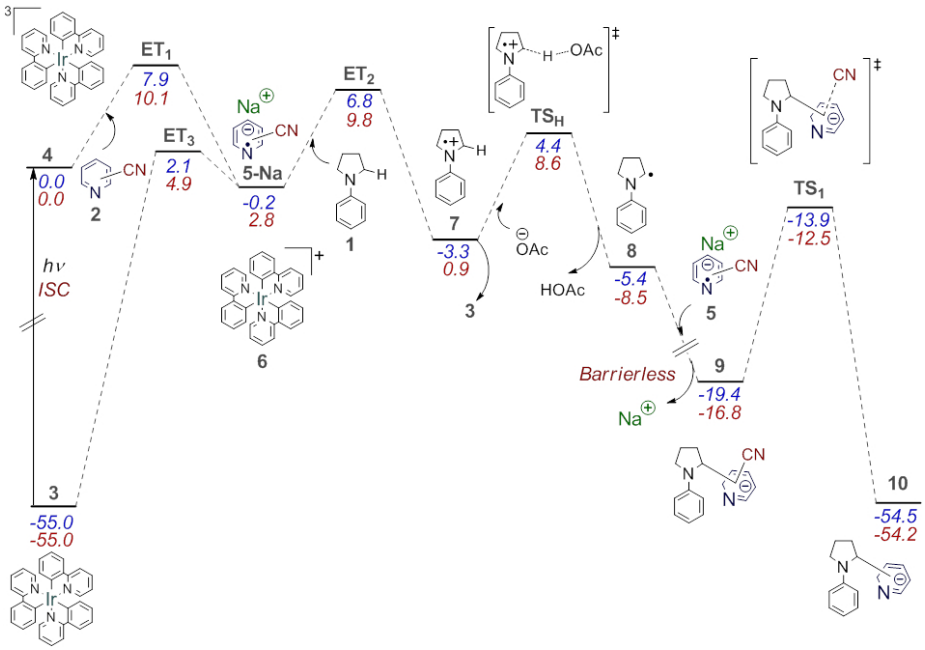

Figure 4.6: Free energy profile of the reaction assisted by Na^+ with *para*-cyanopyridine (**b** blue) and *ortho*-cyanopyridine (**c** red). Energies in kcal.mol^{-1}.

When the energy of **5** is corrected to account for the ion pairs, the energy of $\mathbf{ET}_1$ changes to 7.9 and 10.1 kcal.mol^{-1} for **b** and **c**, respectively. Therefore, the value of K_ν was readjusted to 5.5^{-3} M^{-1} s^{-1}, and the new kinetic model was evaluated. The results are collected in table 4.2. Entries 1-3 show a significant improvement in the quantitative agreement for substrates **a** and **c**, as the largest overall error is now $\approx$ 0.4 kcal.mol^{-1}.

Table 4.2: Calculated yields for **a**, **b** and **c** using 5.5 $\times$ 10^{-3}mol.s^{-1}.L^{-1} as k_ν.

Entry	Substrate/cation	Time(h)	Calc. yield (%)	Exp. yield (%)
1	**a**	12	98	96
2	**b**/Na	12	72[a]	72
3	**c**/Na	24	10	26
4	**a**/Li	11[b]	100	
5	**b**/Li	11[b]	100	
6	**c**/Li	10[b]	100	
7	**b**/Li	8[c]	71	
8	**c**/Li	1[c]	26	

[a] Adjusted to fit Exp. [b] Time to reach 100% yield. [c] Time to reach the yield experimentally obtained.

After observing the impact Na^+ had on the yield, we wondered whether another cation could further stabilize **5** and increase the yield of the reaction. This cation would have to be more polarizing than Na^+ (*i.e.*, form an interaction with **5** with more covalent character, resulting in a stronger ion pair). To this end, we tested the smaller Li^+ cation to see if we could predict higher yields than those obtained experimentally. Predictably, the ion pair between **5** and Li^+ was more favorable than the dissociated ions for all substrates (-9.8 kcal.mol^{-1} for **a**, -15.0 kcal.mol^{-1} for **b**, and -10.6 kcal.mol^{-1}

for **c**). For this simulation we used the same K_ν value used for the Na^+ simulations (5.5×10^{-3}mol.s^{-1}.L^{-1}). Figure 4.7 shows the free energy profile for the Li-assisted reaction of substrates **b** and **c**.

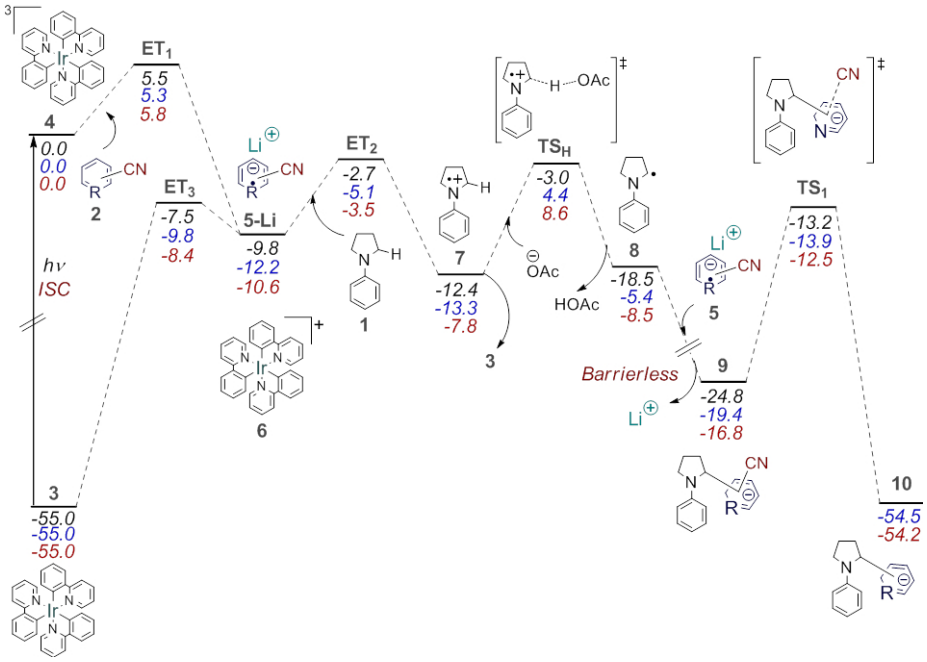

Figure 4.7: Free energy profile of the reaction assisted by Li^+ with *para*-cyanopyridine (**b** blue) and *ortho*-cyanopyridine (**c** red). Energies in kcal.mol^{-1}.

Table 4.2 entries 4-8 show the predicted reaction times to reach 100% yield, evidencing the cation effect for all arenes. The effect is more pronounced for arenes **b** and **c**, especially for **c** where not only the reaction reaches 100% but it does so less than half the time used experimentally. Therefore, our results predict that using LiOAc as the base and **3** as the photocatalyst would significantly increase the arylation rate of **c** under reaction conditions.

Remarkably, there was an optimization of the system in the ex-

perimental work, but this behavior was not detected. By checking the Supporting Information in the publication we see that MacMillan *et al.* did optimize the cation of the base and tested LiOAc. However, this stage of the optimization was done with $Ir(ppy)_2(dtbpy)^+$ (**11**) as the photocatalyst instead of **3** (86% yield with both LiOAc and NaOAc as base at 12 h). We checked the validity of our model by evaluating what would happen with system **11** upon replacement of Na^+ by Li^+.

During electron transfer, a positive charge is generated in the photocatalyst and a negative one is generated in the arene. Here the cation approaches the arene to stabilize the resulting anion. Unlike **3**, **11** is already cationic. Therefore, it will be more difficult to approach the countercation to a system having already an extra positive charge. And if the counterion never approaches the system there will be no effect of the Na^+/Li^+ replacement on the overall behavior. We evaluated the validity of this reasoning by computing the energy of a triple adduct photocatalyst-arene-cation *vs* the energy of the photocatalyst-arene ion pair with the cation at infinite distance, ad checking if this energy is different for both photocatalysts. For reasons of computational cost, these calculations were carried out using the 6-31G* basis set for light atoms. Table 4.3 collects the results for this comparison. The energies show that not only **3** favours the triple adduct, but also that it shows greater stabilization from the Li^+ adduct, supporting our prediction. On the other hand, **11** does not favour the triple adduct with either cation, thus explaining the identical yields obtained experimentally.

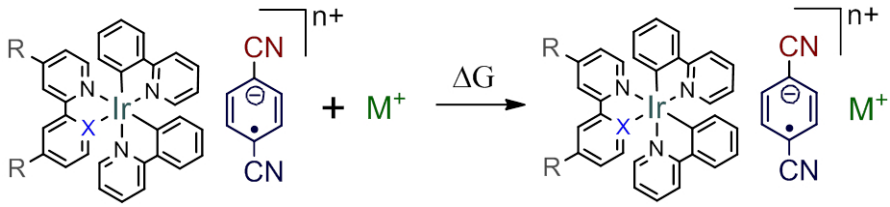

Table 4.3: Energy of the photocatalyst-**5**-cation adduct *vs* dissociated cation. Energies in kcal.mol^{-1}.

Photocatalyst	R/X/n	M	ΔG
3	H/C/0	Na	-7.9
3	H/C/0	Li	-8.6
11	t-Bu/N/1	Na	+5.0
11	t-Bu/N/1	Li	+6.2

Alternative Mechanisms

The computed mechanism assumes the sequential formation of two free radicals, so the first radical must be unreactive enough to allow the formation of the second radical. Moreover, both radicals are in very low concentration, making the process much slower than their barrierless combination suggests. Therefore, it was plausible to think that **5** could instead directly interact with **1** which is in much larger concentration to form the C-C bond, and later transfer an electron to **6** to close the photoredox cycle. The difficulty in such a process is that **1** has no vacant site in the α-carbon as it is saturated. Therefore, proton abstraction needs to be involved in the radical combination whether before, or concerted.

Figure 4.8 shows the possible direct attack pathways for the C-C bond formation. Proton abstraction by the base before $\mathbf{ET}_2$ is quite high in energy (56.3 kcal.mol^{-1}), even a concerted path in which C-C bond is formed and/or cyanide is released results in a

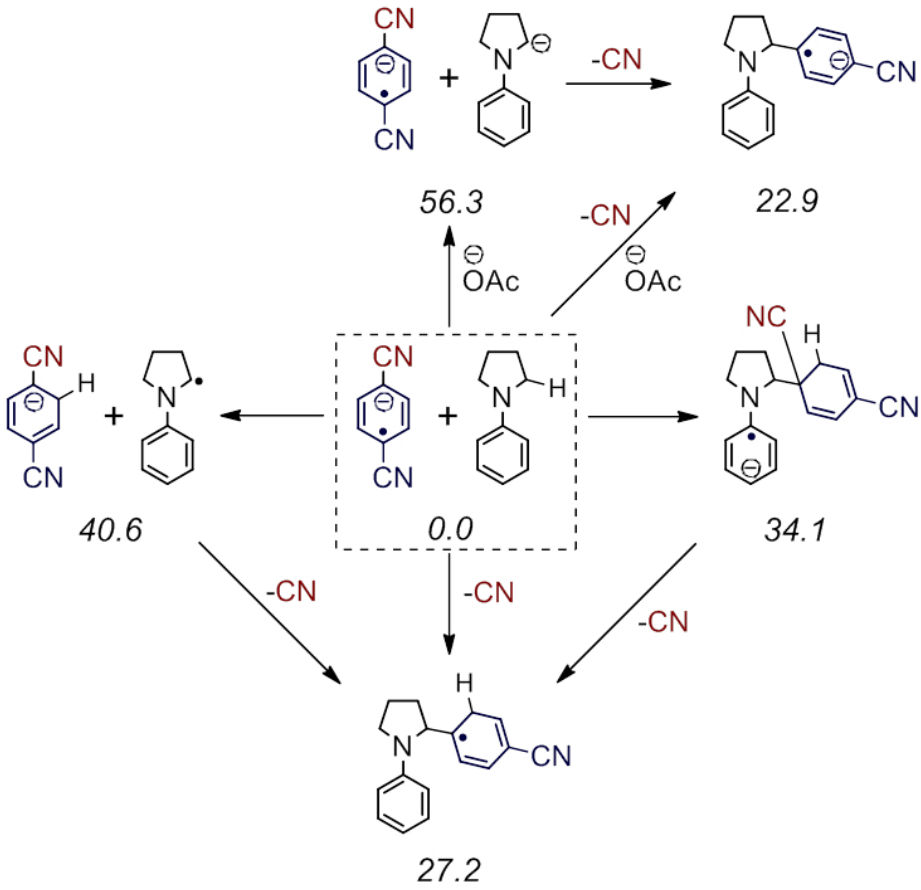

Figure 4.8: Alternative pathways for the C-C bond formation. Energies in kcal.mol^{-1}.

high energy intermediate (22.9 kcal.mol^{-1}). Proton transfer to **5** is lower in energy than to the base but still too high to be plausible (40.6 kcal.mol^{-1}). Again, even a process with a concerted C-C bond formation and/or cyanide release forms a high energy intermediate (27.2 kcal.mol^{-1}). Finally, an alternative pathway was considered in which the proton could be transferred concertedly to the aromatic ring in **5** during C-C bond formation, but this also resulted in a high energy intermediate (34.1 kcal.mol^{-1}). Therefore, the most plausible mechanism remains the formation of both radicals and later radical combination.

Note on Singlet Electron Transfer Barrier

Since a significant portion of the results obtained for this reaction was based on our description of SET barriers, we decided to test the performance of this approach. This was a challenge because we lack experimental data on outer-sphere electron transfer rate constants in homogeneous phase, involving DFT-friendly electronic states. However, we used the electron transfer activation energies only to compare the rates of similar substrates in identical concentrations, thus eliminating the dependence on the pre-exponential term, which is often problematic from a theoretical perspective.[168, 169, 170]

As explained in chapter 2, the activation energy term depends only on the energy difference between products and reactants which DFT methods can reproduce to a sufficient degree, and the reorganization energy. Here the only problem may come from the continuous description of the solvent reorganization energy. Therefore, we carried out a simple test to verify that these energies are consistent.

Figure 4.9 shows the Marcus diagram of the reductive quenching step ($\mathbf{ET}_2$).

According to Marcus theory, the solvent reorganization energy is the same regardless of which energy difference is used ($E_{a-b} = E_{c-d}$ since it is a thermodynamic parameter). Moreover, this solvent reorganization energy has to be identical whether it is calculated using the reactants or the products geometry. We found λ_s values of $\approx$ 38.6 kcal.mol^{-1} for all reference points as shown in figure 4.9, evidencing the ability of this approach to provide physically meaningful information for the purpose of our study. In addition, Nelson *et al.* carried out rate constant calculations on SET processes using a similar approximation to the reorganization energy.[97, 98] In their studies, the authors used this scheme to correctly reproduce experimental rate constants for bimolecular SET processes, confirming the validity of this approximation to λ_s.

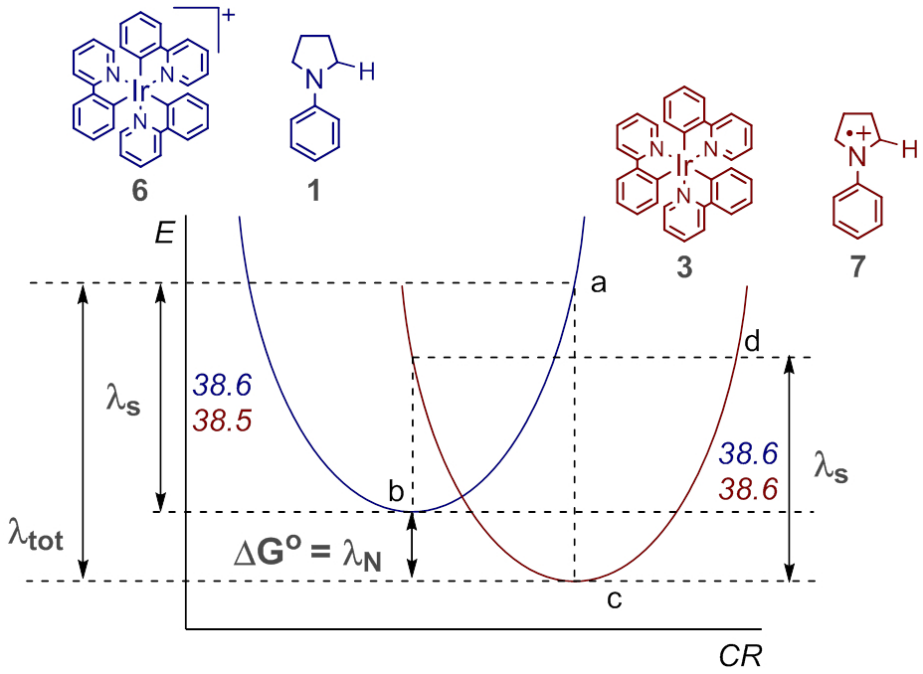

Figure 4.9: Calculation of the solvent reorganization energy λ_s as E_{a-b} and E_{c-d}, using the reactant geometries (blue) and the product geometries (red). Energies in kcal.mol^{-1}.

Reductive Quencher Agent Sampling

According to our mechanism, $\mathbf{ET}_2$ competes with the low barrier deactivation quenching $\mathbf{ET}_3$, but this step depends on the concentration of two photogenerated intermediates (**5** and **6**) which makes it less competitive in the early stages of the reaction. However, there are other species in the medium that could act as reductive quenchers and lower the efficiency of the reaction. Thus, we computed the barrier and energy difference for the SET between **6** and all these other possible quenching agents. The results are collected

in table 4.4.

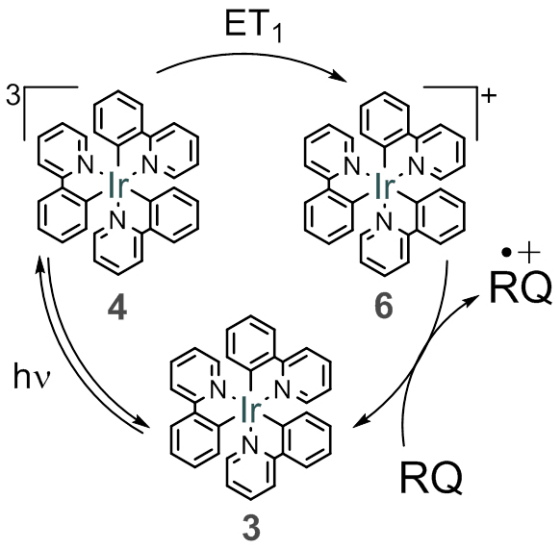

Table 4.4: Energy difference and barrier for SET by all reductive quenchers (RQ). Energies in kcal.mol^{-1}.

RQ	ΔG	$\Delta G^{\ddagger}$
1	-2.6	7.1
5-a	-50.0	2.2
5-b	-55.6	2.3
5-c	-59.3	2.2
DMA	27.4	33.8
OAc	1.7	11.9

The solvent (DMA) is in much higher concentration than **1**, however the barrier is too high (33.8 kcal.mol^{-1}) so the solvent accounts for virtually no deactivation. Aside from **1** and **5**, the only quenching agent that may have an impact is the acetate (OAc) which is in comparable concentration to **1**. However, the barrier for SET to the base is 4.8 kcal.mol^{-1} higher which makes it virtually noncompetitive. Thus, we can say that the only significant deactivation

pathway (other than decay of the excited complex **4**) is the SET from **5** to restore the reactants.

Conclusion

We have computed a plausible mechanism for the photocatalyzed α-arylation of amines using $Ir(ppy)_3$ as the photosensitizer. Our computational model successfully reproduced the relative experimental yields of three different arene substrates with an error of less than 0.4 kcal.mol^{-1}. The mechanism consists in a) light absorption by the photocatalyst and intersystem crossing to form the triplet complex **4**, b) single electron transfer (SET) to the arene to form the radical anionic arene **5** and the cationic complex **6**, c) SET from the amine **1** to **6** to restore the ground state catalyst and generate the amine cationic radical **7**, d) proton abstraction by acetate to form the neutral amine radical **8**, e) radical-radical coupling between **5** and **8** to form intermediate **9**, and f) dissociation of cyanide to yield the α-arylated product **10**.

According to our calculations, the arylation yield depends on a three-pronged competition between the first photoinduced electron transfer ($\mathbf{ET}_1$) to form the anionic radical **5**, the second electron transfer to from the amine radical **7** and restore the catalyst ($\mathbf{ET}_2$), and the deactivation path where **5** gives the electron back to from the ground state catalyst **3** ($\mathbf{ET}_3$). The competition between these steps is also influenced by the large differences in concentration between the species involved. In this sense, $\mathbf{ET}_2$ constitutes a higher energy barrier than $\mathbf{ET}_3$, but it involves the amine reactant **1**, while $\mathbf{ET}_3$ involves **5** which is a transient intermediate in much lower concentration.

Whereas the mechanism does not follow a straightforward dependence on one energy barrier, a microkinetic model was necessary

to obtain qualitative and quantitative information on the reactivity of different arenes. In this regard, the role of the counterion of the base (Na^+) proved to be crucial to obtain the correct relative yields and explain the reactivity of cyanopyridines towards arylation. Moreover, the counterion effect was further explored by computing the mechanism with a more polarizing cation (Li^+), and the results predict an improvement in the arylation yield for all substrates, especially those who were less reactive under experimental conditions, opening the way for more efficient synthetic strategies.

Part II - Trichloromethylation of Acylpyridines

Trichloromethyl groups are known to contribute to the pharmacological properties of several natural products.[171, 172, 173] Therefore, significant efforts have been put into strategies for stereoselective insertion of this group into organic molecules involving both stoichiometric,[174, 175] and catalytic approaches (the latter mainly with Ru[176, 177] and Ti[178, 179] catalysts). However, effective approaches for enantioselective addition of this unit have been limited. Many of the strategies used involve redox-mediated radical addition, thus presenting an opportunity for a photocatalytic approach. Photoredox catalysis enables the generation of highly reactive radicals under mild conditions,[180] but the low activation energy of follow up reactions constitutes a challenge for controlling asymmetric processes. To overcome this obstacle, strategies have been developed in which two catalysts work in tandem for a single reaction.[181] In this approach, photosensitizers capable of inducing electron transfer are combined with asymmetric co-catalysts which are mostly chiral organocatalysts that act as both the chiral center and the Lewis acid site.[13, 182, 183, 184] However, a more desirable approach is to employ a single catalyst which can perform both as the photosensitizer and the asymmetric catalyst.

Earlier work towards this goal involved high energy UV light in combination with Lewis acid and hydrogen bonding interactions to perform enantioselective catalysis.[161, 185, 186] Most current visible-light photosensitizers however, are cyclometallated

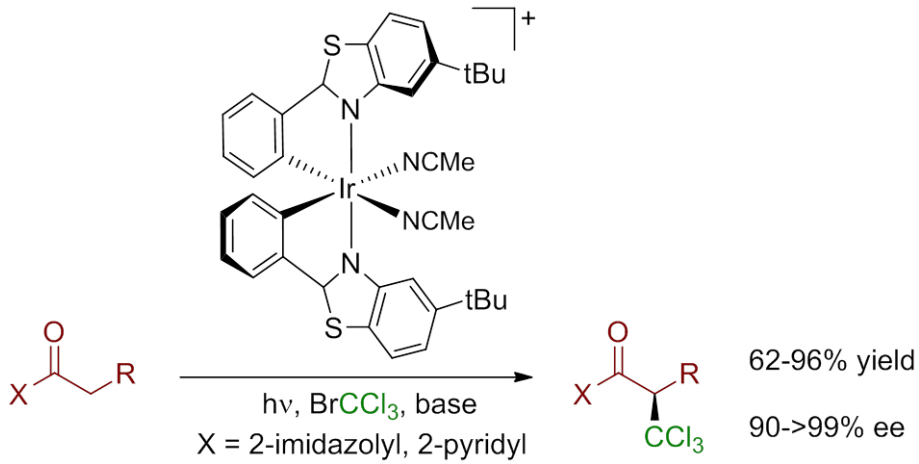

Figure 4.10: General reaction scheme of the trichloromethylation.

Ir or Ru transition metal complexes,[187, 188] and it is widely known that chiral metal complexes can catalyze asymmetric transformations.[189] With this in mind, Meggers *et al.*[190] developed a system capable of photoinducing single electron transfer and enable enantioselective trichloromethylation of 2-acyl imidazoles and 2-acylpyridines (Figure 4.10). Here a chiral Λ-iridium complex acts as both the photosensitizer and the asymmetric catalyst.[191] The complex (**I**) is an octahedral iridium centre with two bidentate achiral ligands in a left-handed propeller-type arrangement, which is the origin of chirality in the system.[192]

Computational chemistry is an established and valuable tool for the mechanistic study of processes in asymmetric catalysis.[193, 194, 195, 61, 196] Therefore, we decided to study this reaction using DFT methods to try to reproduce experimental enantiomeric excess, and to elucidate the factors that affect enantioselectivity and attempt to predict a system which might produce better enantioselectivity. We chose 1-(pyridin-2-yl)propan-1-one (**1**) as the substrate, which forms

the trichloromethyl-substituted pyridine (**3**) with 67% yield and 95% enantiomeric excess. The full energy profile was calculated using a model system for the photocatalyst, in which *tert*-butyl groups were replaced by methyl. Geometry optimizations, frequency calculations and TD-DFT calculations on the model system were carried out at the ω-B97x-D level of theory,[47] with the LANL2DZ basis set with polarization "f" type function (coeff.=0.938) for Ir and 6-31+G(d) for light atoms (BS).[145, 116, 117] Solvent contributions of methanol (DMA ϵ=32.613) were added via the SMD model as implemented in Gaussian09,[53] and single electron transfer barriers were estimated using the method described in chapter 2. Enantiomeric excess calculations on the real system and on hypothetical systems were carried out at the ONIOM(ω-B97x-D:BS/UFF) as implemented in Gaussian 09. Single point free energies were calculated at the ω-B97x-D:BS level in methanol. Low frequencies were converted to 100 cm^{-1} following recent suggestions in the bibliography.[197, 198]

Reaction Mechanism

The mechanism proposed by Meggers *et al.*, like most mechanisms involving photoredox catalysis, consisted of two cycles (Figure 4.11). A "light" cycle which is the photoredox cycle, and a "Dark" cycle which is the catalytic cycle. In the dark cycle, the substrate **1** coordinates to the catalyst **I** by replacing the two labile acetonitrile groups; in this new complex **4** the 1-(pyridin-2-yl)propan-1-one ligand can lose a proton to become an anionic ligand. This unsaturation makes the π system in the ligand become fully delocalized.

As a consequence, intermediate **5** is now similar in electronic structure to $Ir(ppy)_3$ in that it contains a *fac*-polypyridil-type ligand that enables photocatalytic activity.

Here the radical CCl_3, which was generated by photoinduced electron transfer (SET) from the light cycle, can form the C-C bond with the α-carbon to the carbonyl in enantioselective fashion, to generate radical intermediate **6**. This complex transfers an electron to complete the light cycle resulting in the cationic intermediate **7**, from which the product **3** can dissociate to regenerate the resting state **2**.

The light cycle starts with the cyclometallated intermediate **5**, which can absorb visible light to form the triplet state complex **8**. This excited complex transfers an electron to CCl_3Br to generate the CCl_3, the cationic complex **9** and bromide. Finally, **9** can take an electron from **6** to restore the photosensitizer **5** and start the cycle again. In addition to the cycles described above, the authors also proposed that direct electron transfer from **6** to CCl_3Br can also take place. This constitutes a *propagation* pathway which would account for the quantum yield of ≈ 5 observed experimentally. We carried out calculations on this mechanism and the results are collected in figure 4.12.

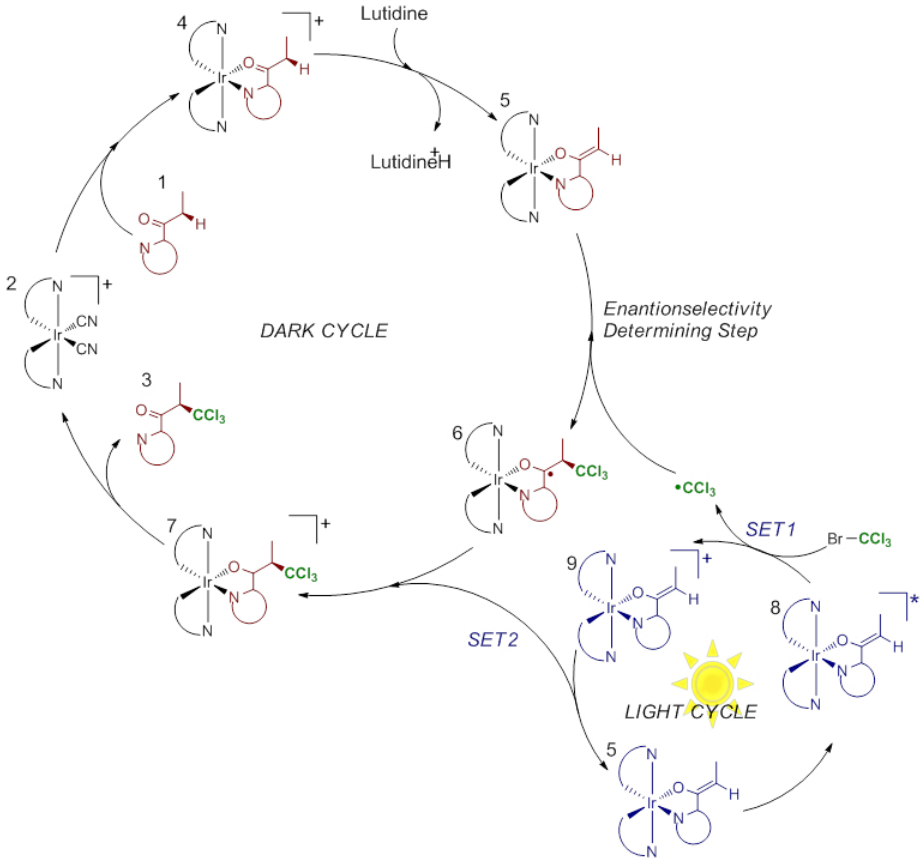

Figure 4.11: Preliminary reaction mechanism of the trichloromethylation.

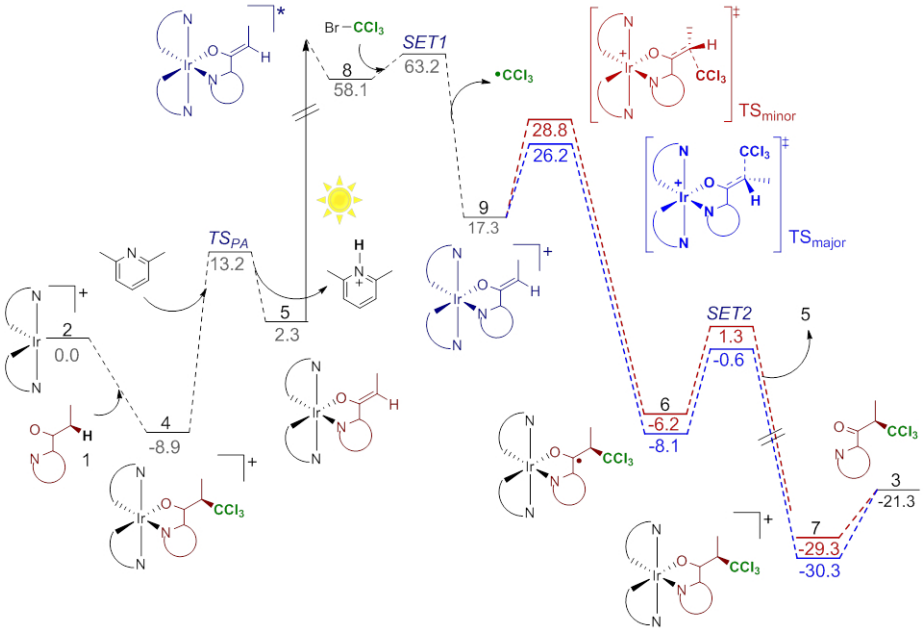

Figure 4.12: Free energy profile of the trichloromethylation mechanism with the model catalyst. Energies in kcal.mol^{-1}.

The symmetry of the catalyst causes the intermediates before C-C bond formation to have only one possible conformation, significantly reducing the degrees of freedom in the mechanism. For simplicity purposes, the cycle was represented with the free catalyst as the referential zero, without the acetonitrile ligands present in the precursor (Figure 4.12). Coordination of **1** predictably stabilizes the free catalyst (by 8.9 kcal^{-1}). Proton abstraction from 4 to 5 by lutidine is clearly endoergic (11.2 kcal.mol^{-1}) indicating the photosensitizer would prefer to be in the protonated inactive form. More serious is the fact that the barrier for deprotonation through $\mathbf{TS}_{PA}$ is 22.1 kcal.mol^{-1}, in the limits of what can be considered for the experimental conditions. Excitation of **5** forms the triplet state complex **8** at 58.1 kcal.mol^{-1} above reactants which can rapidly

transfer an electron to CCl_3Br (barrier of 5.1 kcal.mol^{-1}) to generate the strongly favoured cationic complex **9** and the CCl_3 radical at 17.3 kcal.mol^{-1}.

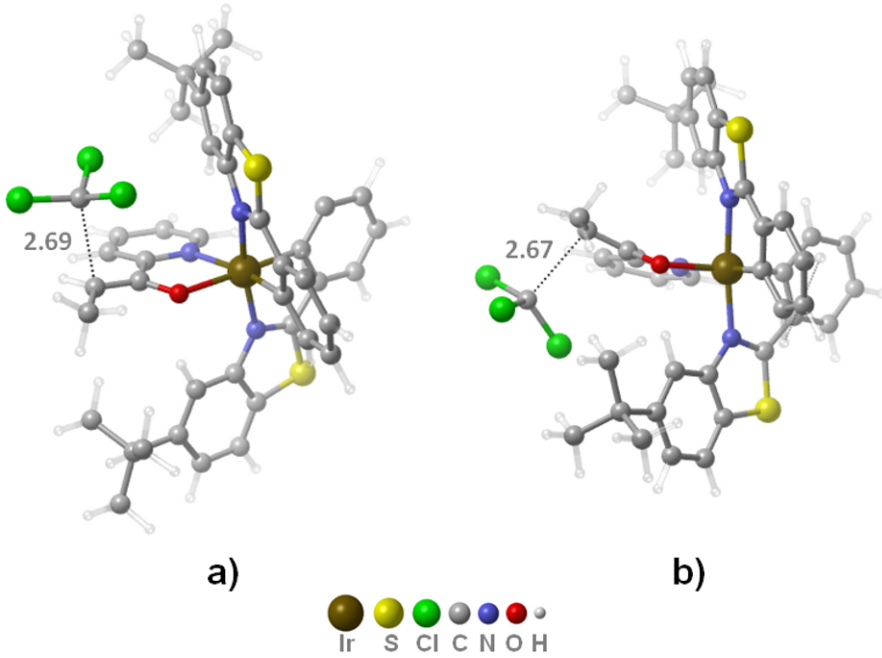

Figure 4.13: Optimized geometries of the transition states leading to major (a) and minor (b) products. Distances in Å.

We found two transition states corresponding to the C-C bond formation step (Figure 4.13) with low energy barriers of 8.9 and 11.5 kcal.mol^{-1}, for the formation of the major and minor product, respectively. The calculated enantiomeric excess (ee) of the model system is 96%, which is in close agreement with the experimental ee of 95%. Calculations indicate that enantioselectivity is caused by steric hindrance of the chiral ligand in one of the two attack conformations. The approach of the CCl_3 radical is unhindered when the *arm* of the ligand points away from the acetyl group of the

substrate, in the direction of the attack (TS_{major} figure 4.13-a), and hindered in the opposite case (TS_{minor} figure 4.13-b).

Enantioselective C-C bond formation generates intermediate **6**, which can transfer an electron back to the **9** cation (**SET2**)to restore the photosensitizer **5** and form the cationic trichloromethylated complex **7**, where the product **3** can easily dissociate and regenerate the catalyst. **SET2** has an energy barrier of 7.4 kcal.mol^{-1}, and the dissociation of **3** has an energy cost of 9.0 kcal.mol^{-1}. Thus, the process is downhill after the formation of the C-C bond.

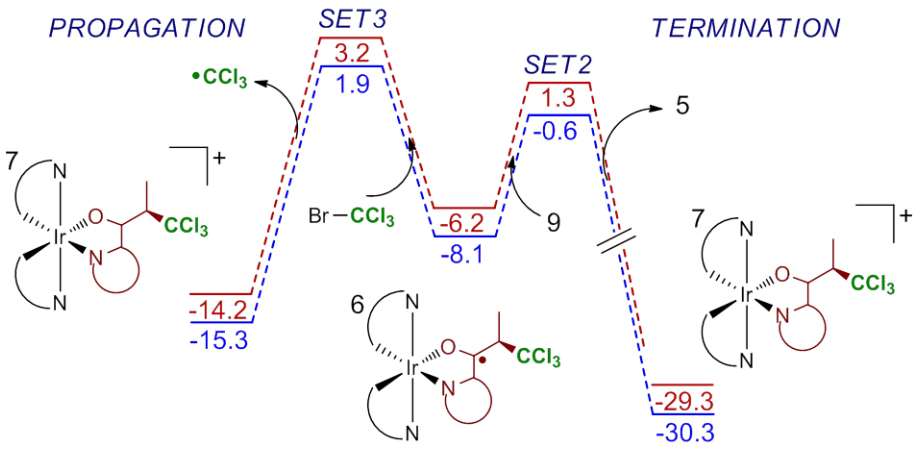

Figure 4.14: Free energy profile showing the propagation/termination competition. Energies in kcal.mol^{-1}.

In addition to the photoinduced electron transfer from **5** to CCl_3Br, trichloromethyl radical can also be formed via electron transfer from complex **6** (**SET3**) in a *propagation* path that generates the radical species without photons being involved. The energy barrier of **SET3** is 9.5 kcal.mol^{-1} (9.4 for the minor product), which is higher than that of **SET2** (Figure 4.14). The raw numbers in figure 4.14 would suggest the termination pathway through

SET$_2$ to dominate. However as shown in chapter 3, the competition of these two steps is severely affected by the concentration of the species involved. In this case, **9** is a transient species formed by light absorption, thus in much lower concentration than CCl_3Br, which is a reactant. Therefore, initially propagation is more competitive than termination, which accounts for the quantum yield of 5 observed experimentally.

Sampling of Photoinduced SET

According to the proposed mechanism, photoinduced electron transfer step takes place after the light-driven generation of the triplet complex **8**, upon deprotonation by lutidine. However, not only this step is endoergic but it also has a rather high energy barrier. This implies that only a portion of the small complex is deprotonated at any time, which in turn makes light absorption (and hence the generation of CCl_3 radical) a slower process than for other photoredox processes (e.g. Part I of this chapter). Therefore, we studied the light absorption of all species that preclude the formation of **5** to determine if there is a plausible photosensitizer which is lower in energy in the cycle.

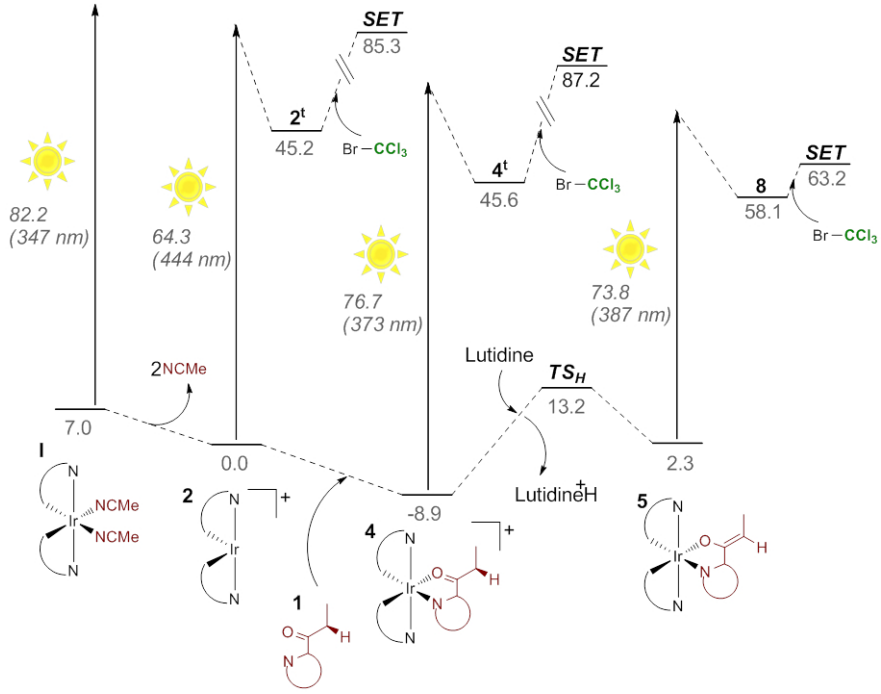

Figure 4.15: Light absorption and electron transfer for different intermediates. Free energies in kcal.mol^{-1}.

Figure 4.15 shows the absorption energies and SET energy barriers for all stationary points up to **5**. The catalyst **I** shows one significant MLCT absorption band at 347 nm (f=0.2912). This strong band is in agreement with the maximum absorption observed for the catalyst experimentally.[199] However, the barrierless dissociation of the acetonitrile ligands leads to the formation of the lower energy complex **2**, indicating that the catalyst is entirely in the dissociated form. Apart form the strong band at $\approx$ 450 nm, the absorption of **2** shows a new MLCT band at 444 nm (f=0.0596) whose corresponding triplet complex $\mathbf{2}^t$ relaxes to 45.2 kcal.mol^{-1}. This complex however, does not transfer an electron to CCl_3Br as the barrier for SET is prohibitive (40.1 kcal.mol^{-1}).

Photoinduced electron transfer from **4** shows a similar pattern. The incorporation of a third bidentate electron-delocalizing ligand causes the appearance of a stronger MLCT band at 373 nm (f=0.1704). However, SET to form the CCl_3 radical has a barrier of 41.6 kcal.mol^{-1}, indicating this complex is not the photosensitizer either. Finally, complex **5** has a fully delocalized ligand system, which shifts the MLCT band to 387 nm (f=0.1482).

While higher in energy than the other complexes, **5** can act as the photosensitizer as the triplet state form **8** shows a low SET barrier (5.1 kcal.mol^{-1}) towards the formation of the CCl_3 radical. Thus, our calculations show that the photosensitizer is indeed complex **5** despite the fact that it is not favored over complex **4** and that the barrier for the deprotonation is quite high. It is worth noting however, that SET results in a barrierless dissociation of CCl_3Br. Therefore, back SET is not a problem for the overall efficiency of the process. In addition, the only path affected by the energy cost of forming **5** is the termination pathway, as propagation directly generates the CCl_3 radical.

Enantioselectivity with Different Catalysts

After locating the selectivity determining step for the model system (**b**), we optimized the corresponding transition states using the real system (by replacing the methyl groups in the ligand for *tert*-butyl). The calculated ee for the real system (**c**) is 99.1%, which is still in good agreement with experimental results (calculated ee represents an error in the energy difference of 0.7 kcal.mol^{-1}). Figure 4.16 shows the energy profile with the real system. There are some

differences between the real catalyst and the model system. First, coordination of the reactant is not strongly favored as in the case of **b**. In addition, deprotonation has a lower energy barrier, and is not endoergic. This is because the system is more constrained, and the protonated substrate contains an sp^3 carbon that increases steric repulsion with the ligand. As a result, the energy of **4** and **6** increases with respect to intermediates with only sp^2 carbons like **5**. This also has the interesting side effect of significantly lowering the barrier for deprotonation through $\mathbf{TS}_{PA}$, which is only 15.3 kcal.mol^{-1} for the real system, thus fully affordable.

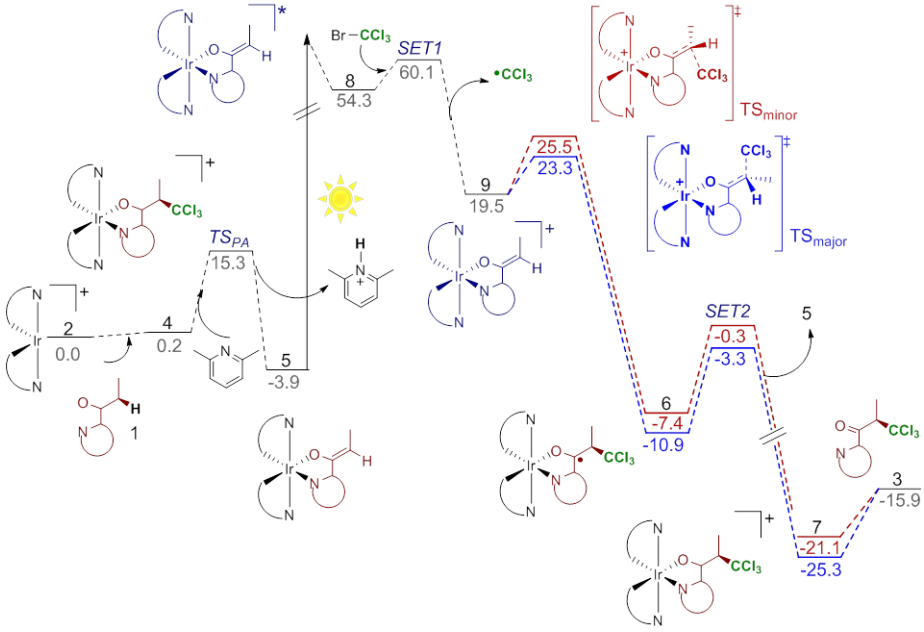

Figure 4.16: Free energy profile of the trichloromethylation mechanism with the real catalyst. Energies in kcal.mol^{-1}.

The nature of the substituents in the catalyst has an effect on the calculated ee. In light of this fact, we decided to study the effect

of the R group (*i.e.*, the substituent in the ligand) on the predicted enantioselectivity. To this end we calculated TS_{major} and TS_{minor} by with different R groups, varying in bulkiness.

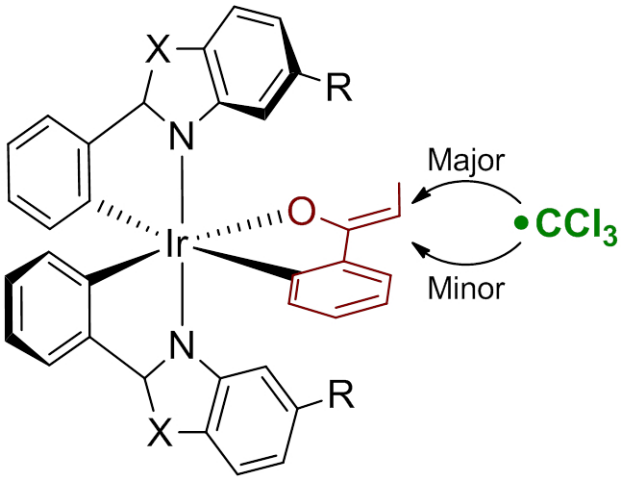

Table 4.5: Transition state energies and ee calculated for different catalysts. Free energies in kcal.mol^{-1}. Dihedral angle (D) between the substrate plane and the N-Ir-N axis in **5**.

Catalyst	-R/X	D(ϕ)	$\Delta G^{\ddagger}_{major}$	$\Delta G^{\ddagger}_{minor}$	ee(%)[exp]
a	-H/S	99	7.7	9.6	91
b	-methyl/S	99	6.8	9.2	96
c	-*tert*-butyl/S	101	8.6	12.0	99.1[95]
d	-adamantyl/S	103	9.9	12.4	97
e	-*tert*-butyl/CHCH	105	8.8	9.3	33

Apart from methyl (**b**) and *tert*-butyl (**c**), we calculated the ee using a hypothetical photocatalyst with adamantyl groups as substituents (**d**) and one without substituents (**a**). In addition, we calculated a catalyst in which the sulfur is replaced by C=C to increase the hindering effect of the ligand while maintaining aromaticity (**e**). The idea was to sample a range of substituents with

increasing hindering effect and determine whether enantioselectivity could be improved.

The results are collected in table 4.5. Predictably, catalysts with smaller substituents such as **a** showed lower enantioselectivity towards trichloromethylation than the experimental catalyst **c** (91% *vs* 99.1%), as the approach of the CCl_3 radical is less hindered by the absence of a bulky substituent. Catalyst **b** follows the same trend (96%), showing higher enantioselectivity than **a** but lower than **c**. However, a catalyst with a larger substituent like **d** rather than increasing enantioselectivity, shows a lower ee (97%). This unexpected loss of enantioselectivity is even more apparent for catalyst **e**, where it virtually disappears (33%). These results indicate that the relation between the bulkiness of the substituent and enantiomeric excess is not straightforward.

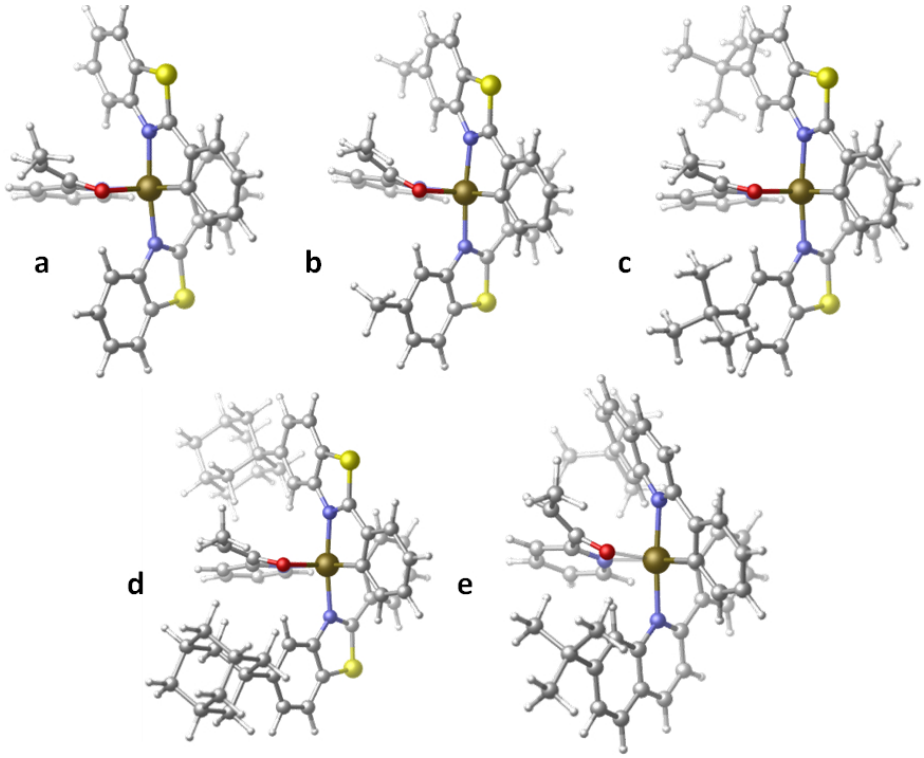

Figure 4.17: Optimized geometry of **5** for all catalysts.

Figure 4.17 shows the optimized geometry of **5** for all catalysts studied. Both catalysts **d** and **c** show that the ligand is too bulky to allow the formation of the sp^3 trichloromethylated product in either enantiomer. Thus, in addition to hindering the approach of CCl_3 radical, the substituent can also affect the formation of the trichloromethylated product, in that it imposes constraints on the system which hinders the rearrangement of the substrate from sp^2 to sp^3 to allow the C-C bond formation. This effect can be illustrated by looking at the dihedral angle formed between the plane of the substrate molecule and the N-Ir-N axis (90 degrees for a perfect octahedron) as it increases with the size of the substituent.

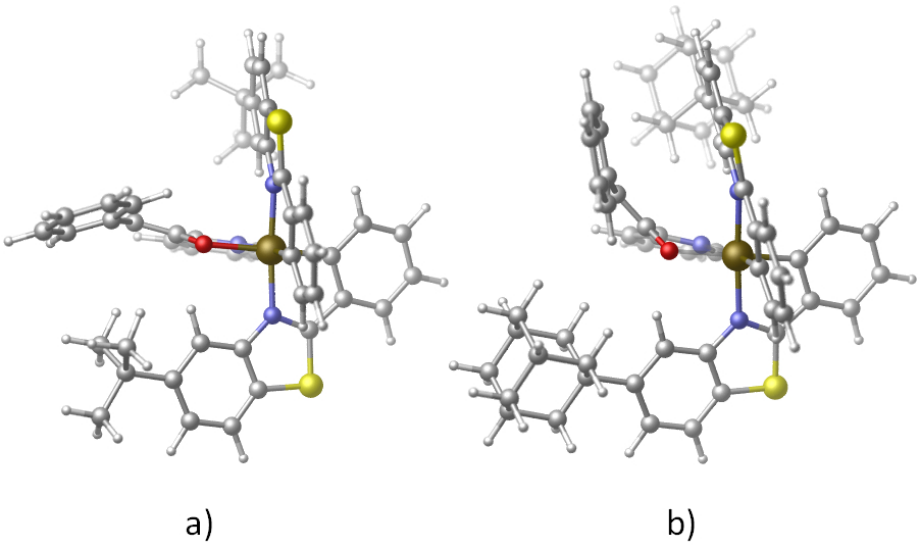

Figure 4.18: Optimized geometry of **5** with catalysts **c** and **d** when the substrate has a phenyl group.

In the case of **c**, the substituent can rotate and leave enough room for the substrate to occupy. However, both **d** and **e** catalysts are too constrained to leave room for the newly formed sp^3 group. In fact, when the methyl group in the substrate is replaced by phenyl (which can rotate to avoid hindrance from the substituent), catalyst **c** shows slightly higher enantioselectivity, correctly producing experimental results (99.6%) vs 99.4%). Furthermore, **d** shows an increase in ee from 97% with methyl to 98.5% with phenyl. However, the effect is less pronounced as the adamantyl group is still significantly more bulky and still imposes a distortion of the system (figure 4.18). This greater enantioselectivity is due to the planarity of the phenyl group which imposes lesser constraints on the product formation, while the approach of CCL_3 radical remains hindered in TS_{minor}.

The competition between steric hindrance towards the approach

of the CCl_3 radical (which only affects TS_{minor}) and distortion of the octahedral geometry for the rearrangement of the substrate during C-C bond formation (which affects both TS_{major} and TS_{minor}) constitutes the origin of enantioselectivity for the system. For the catalysts and substrates studied computationally, the combination of **c** and the phenyl substituted substrate show the best performance as they can minimize the effect of the substituent on the product formation while maximizing the hindering effect on the approach of CCl_3 radical in TS_{minor}.

Conclusion

We carried out calculations on the reaction mechanism of the trichloromethylation of 2-acylpyridines, and correctly reproduced experimental enantioselectivity. The reaction consists of two cycles. A dark cycle which involves the coordination and later deprotonation of the substrate to the catalyst complex, followed by asymmetric formation of a C-C bond with the CCl_3 radical to generate a radical intermediate that can lose an electron to release the trichloromethylated product; and a light cycle which consists in the excitation of the photosensitizer leading to the generation of the CCl_3 radical by outer-sphere electron transfer. This results in a cationic complex that can take an electron from the dark cycle to restore the photosensitizer.

The photosensitizer was identified as the complex resulting from deprotonation of the substrate, despite the fact that deprotonation has a high energy barrier and the resulting complex is in equilibrium with the protonated one. In addition to the photoredox-driven generation of the CCl_3 radical, direct electron transfer from the intermediate after the C-C bond formation can also form CCl_3, explaining the experimental quantum yield of 5.

Experimental ee was correctly reproduced for substrates with methyl (99.1% vs 95%) and phenyl groups (99.6% vs 99.4%). Enantioselectivity was studied for both substrates and several different catalysts were sampled to determine its origin. Two competing steric factors involving the substituents in the symmetric ligand were found to be determinant: One is steric hindrance towards the approach of the CCl_3 radical, which only affects the formation of the minor prod-

uct, and the other is the constraint imposed by the ligand towards the rearrangement of the substrate from sp^2 to sp^3 during C-C bond formation, which affects both the major and minor products. Maximizing the former while minimizing the latter yields the optimal enantioselectivity. In our study, this is achieved by the -*tert*-butyl substituted catalyst which shows the highest theoretical ee (99.6%). These results are important for the design of future asymmetric catalytic reactions and the challenging task of optimizing enantioselectivity in chemically relevant processes.

Chapter 5

Conclusions

To summarize, we hope to have shown that the mechanism of relevant reactions activated by irradiation of light in solution can be studied successfully using a combination of ground-state DFT calculations, TD-DFT calculations, and kinetic models. In most of these cases a comprehensive treatment of the excited states involved was beyond our capabilities, as TD-DFT is only reliable when analyzing vertical excitations. Yet, useful information can be obtained, and a mostly complete picture of the mechanism can be computed, using mainly ground-state DFT, in combination with kinetic models when concentrations were relevant.

In the reactions studied in this work we have identified the structural factors that determine reactivity, as well as the experimental quantum yields. In the cases where more than one product was possible we elucidated the origin of selectivity. Finally, in those where

excited state properties were relevant to determine reactivity, vertical excitations from TD-DFT calculations were used to determine their absorption behavior in the energy range of the irradiation used experimentally.

Concerning the specific reactions covered in this thesis, an in-depth discussion on the conclusions has been covered in their respective chapters. In this section only the main points will be summarize. Regarding the perfluoroalkylation of arylacetates:

- The quantum yield larger than one (3.8) was rationalized on the basis of the competition between the combination of the radicals formed photochemically, and the chain propagation caused by the single electron transfer from the perfluoroalkylated intermediate, to generate the alkyl radical.

- Origin of selectivity towards the *para*- and *ortho*- homolytic aromatic substitution (HAS), rather than the α-carbonyl attack, was identified as the distortion of the planar system during C-C bond formation, which is minimal for HAS and considerably greater for the α-carbonyl product.

- The different reactivity observed for substrates with similar electron-withdrawing groups was found to depend on the distortion of the planar π system caused by steric repulsion from the substituents.

On the dioxygen insertion into the Pt(II)-Me bond:

- Singlet oxygen was found to be generated by the light-driven formation of a disubstituted terpyridine complex, where the Pt(II)-Me bond has been weakened and a vacancy has been created for oxygen to occupy.

- Methyl migration to form the methylperoxo complex competes with photochemical deactivation via intersystem crossing. This competition was found to be affected by the substituents in the terpyridine ligand.

- Substituents that form hydrogen bonds with dioxygen undergo direct migration, while substituents that cause steric repulsion force the ligand to dissociate one branch to enable migration.

- The mechanism was found to be unimolecular rather than bimolecular, as originally proposed based on experimental observations.

Concerning the C-H arylation of amines:

- The reaction yield depends on the competition after photoinduced electron transfer to form the arene radical anion, between back electron transfer to restore the ground state photocatalyst, and electron transfer to form the amine radical that enables C-C bond formation.

- The choice of the cation accompanying the base was found to have a large impact in the rate of the reaction when the substrate has a lower reduction potential. That is, more polarizing cations assist electron transfer by forming ion pairs with the resulting radical.

Finally, on the trichloromethylation of acylpyridines:

- Enantioselectivity was rationalized on the basis of steric repulsive effects from the ligand in the chiral photocatalyst. In

this regard, the bulkiness of the substituent hinders the approach of the CCl_3 radical in the transition state leading to one enantiomer.

- Sampling of hypothetical catalysts with varying size of the aforementioned substituents shows that for very large groups, the system becomes too distorted and the asymmetric driving effect is lessened.

Bibliography

[1] M. Oelgemller, *Chemical Reviews*, 2016, **116**, 9664–9682.

[2] D. M. Schultz and T. P. Yoon, *Science*, 2014, **343**, 985–993.

[3] Q. Fu in *Encyclopedia of Atmospheric Sciences*, ed. J. R. Holton; Academic Press, Oxford, 2003; pp. 1859 – 1863.

[4] M. B. Rubin and S. E. Braslavsky, *Photochemical and Photobiological Sciences*, 2010, **9**, 670674.

[5] D. Frackowiak, *Journal of Photochemistry and Photobiology B: Biology*, 1988, **2**, 399 – 402.

[6] A. Juris, V. Balzani, F. Barigelletti, S. Campagna, P. Belser, and A. von Zelewsky, *Coordination Chemistry Reviews*, 1988, **84**, 85 – 277.

[7] I. M. Dixon, J.-P. Collin, J.-P. Sauvage, L. Flamigni, S. Encinas, and F. Barigelletti, *Chemical Society Reviews*, 2000, **29**, 385–391.

[8] D. M. Arias-Rotondo and J. K. McCusker, *Chemical Society Reviews*, 2016, **45**, 5803–5820.

[9] M. A. Ischay, M. E. Anzovino, J. Du, and T. P. Yoon, *Journal of the American Chemical Society*, 2008, **130**, 12886–12887.

[10] J. Yang, D. F. Cauble, A. J. Berro, N. L. Bauld, and M. J. Krische, *The Journal of Organic Chemistry*, 2004, **69**, 7979–7984.

[11] T.-G. Baik, A. L. Luis, L.-C. Wang, and M. J. Krische, *Journal of the American Chemical Society*, 2001, **123**, 6716–6717.

[12] J. Yang, G. A. N. Felton, N. L. Bauld, and M. J. Krische, *Journal of the American Chemical Society*, 2004, **126**, 1634–1635.

[13] D. A. Nicewicz and D. W. C. MacMillan, *Science*, 2008, **322**, 77–80.

[14] N. Vignola and B. List, *Journal of the American Chemical Society*, 2004, **126**, 450–451.

[15] X. Dai, N. A. Strotman, and G. C. Fu, *Journal of the American Chemical Society*, 2008, **130**, 3302–3303.

[16] H. B. Gray and J. R. Winkler, *Annual Review of Biochemistry*, 1996, **65**, 537–561.

[17] K. Kalyanasundaram, *Coordination Chemistry Reviews*, 1982, **46**, 159 – 244.

[18] Y. You and W. Nam, *Chemical Society Reviews*, 2012, **41**, 7061–7084.

[19] T. Forster, *Discussions of the Faraday Society*, 1959, **27**, 7–17.

[20] D. L. Dexter, *The Journal of Chemical Physics*, 1953, **21**, 836–850.

[21] G. D. Scholes, *Annual Review of Physical Chemistry*, 2003, **54**, 57–87.

[22] M. Majek and A. Jacobi von Wangelin, *Accounts of Chemical Research*, 2016, **49**, 2316–2327.

[23] M. A. Cismesia and T. P. Yoon, *Chemical Science*, 2015, **6**, 5426–5434.

[24] A. Comas-Vives, C. González-Arellano, A. Corma, M. Iglesias, F. Sánchez, and G. Ujaque, *Journal of the American Chemical Society*, 2006, **128**, 4756–4765.

[25] J. Cid, H. Gulyas, J. J. Carbó, and E. Fernandez, *Chemical Society Reviews*, 2012, **41**, 3558–3570.

[26] T. Sperger, I. A. Sanhueza, I. Kalvet, and F. Schoenebeck, *Chemical Reviews*, 2015, **115**, 9532–9586.

[27] T. W. Schneider, M. Z. Ertem, J. T. Muckerman, and A. M. Angeles-Boza, *ACS Catalysis*, 2016, **6**, 5473–5481.

[28] S. Fischer, O. S. Bokareva, E. Barsch, S. I. Bokarev, O. Kuhn, and R. Ludwig, *ChemCatChem*, 2016, **8**, 404–411.

[29] T. B. Demissie, K. Ruud, and J. H. Hansen, *Organometallics*, 2015, **34**, 4218–4228.

[30] N. Cox, M. Retegan, F. Neese, D. A. Pantazis, A. Boussac, and W. Lubitz, *Science*, 2014, **345**, 804–808.

[31] J. R. Vance, A. Schfer, A. P. M. Robertson, K. Lee, J. Turner, G. R. Whittell, and I. Manners, *Journal of the American Chemical Society*, 2014, **136**, 3048–3064.

[32] L.-H. Liu, D. Wu, S.-H. Xia, and G. Cui, *Journal of Computational Chemistry*, 2016, **37**, 2212–2219.

[33] T. B. Demissie and J. H. Hansen, *The Journal of Organic Chemistry*, 2016, **81**, 7110–7120.

[34] X.-Q. Hu, X. Qi, J. R. Chen, Q.-Q. Zhao, L. Yan, and W.-J. Xiao, *The Journal of Organic Chemistry*, 2016, **7**, 11188–11200.

[35] K. L. Skubi, T. R. Blum, and T. P. Yoon, *Chemical Reviews*, 2016, **116**, 10035–10074.

[36] M. N. Hopkinson, A. Tlahuext-Aca, and F. Glorius, *Accounts of Chemical Research*, 2016, **49**, 2261–2272.

[37] D. C. Fabry and M. Rueping, *Accounts of Chemical Research*, 2016, **49**, 1969–1979.

[38] O. Gutierrez, J. C. Tellis, D. N. Primer, G. A. Molander, and M. C. Kozlowski, *Journal of the American Chemical Society*, 2015, **137**, 4896–4899.

[39] W. Koch and M. C. Holthausen, in *A Chemist's Guide to Density Functional Theory*, Wiley-VCH Verlag GmbH, 2001; pp. 41–64.

[40] P. Hohenberg and W. Kohn, *Physical Review*, 1964, **136**, B864–B871.

[41] W. Kohn and L. J. Sham, *Physical Review*, 1965, **140**, A1133–A1138.

[42] Y. Zhao and D. G. Truhlar, *Theoretical Chemistry Accounts*, 2008, **120**, 215–241.

[43] A. D. Becke and E. R. Johnson, *The Journal of Chemical Physics*, 2005, **123**, 154101.

[44] S. Grimme, J. Antony, T. Schwabe, and C. Muck-Lichtenfeld, *Organic Biomolecular Chemistry*, 2007, **5**, 741–758.

[45] S. Grimme, J. Antony, S. Ehrlich, and H. Krieg, *The Journal of Chemical Physics*, 2010, **132**, 154104.

[46] A. Dreuw, J. L. Weisman, and M. Head-Gordon, *The Journal of Chemical Physics*, 2003, **119**, 2943–2946.

[47] J.-D. Chai and M. Head-Gordon, *Physical Chemistry Chemical Physics*, 2008, **10**, 6615–6620.

[48] T. Yanai, D. P. Tew, and N. C. Handy, *Chemical Physics Letters*, 2004, **393**, 51 – 57.

[49] J. Tomasi, B. Mennucci, and R. Cammi, *Chemical Reviews*, 2005, **105**, 2999–3094.

[50] S. Miertu, E. Scrocco, and J. Tomasi, *Chemical Physics*, 1981, **55**, 117 – 129.

[51] J. L. Pascual-ahuir, E. Silla, and I. Tuon, *Journal of Computational Chemistry*, 1994, **15**, 1127–1138.

[52] G. Scalmani and M. J. Frisch, *The Journal of Chemical Physics*, 2010, **132**, 114110.

[53] A. V. Marenich, C. J. Cramer, and D. G. Truhlar, *The Journal of Physical Chemistry B*, 2009, **113**, 6378–6396.

[54] F. Maseras and K. Morokuma, *Journal of Computational Chemistry*, 1995, **16**, 1170–1179.

[55] M. J. Field, P. A. Bash, and M. Karplus, *Journal of Computational Chemistry*, 1990, **11**, 700–733.

[56] A. Warshel and M. Levitt, *Journal of Molecular Biology*, 1976, **103**, 227 – 249.

[57] S. Dapprich, I. Komromi, K. Byun, K. Morokuma, and M. J. Frisch, *Journal of Molecular Structure: {THEOCHEM}*, 1999, **461462**, 1 – 21.

[58] H. Hu and W. Yang, *Annual Review of Physical Chemistry*, 2008, **59**, 573–601.

[59] M. Svensson, S. Humbel, R. D. J. Froese, T. Matsubara, S. Sieber, and K. Morokuma, *The Journal of Physical Chemistry*, 1996, **100**, 19357–19363.

[60] C. Bo and F. Maseras, *Dalton Transactions*, 2008, pp. 2911–2919.

[61] J. Jover and F. Maseras, in *Computational Studies in Organometallic Chemistry*, ed. S. A. Macgregor and O. Eisenstein, Springer International Publishing, Cham, 2016; pp. 59–79.

[62] J. J. Carbó, F. Maseras, C. Bo, and P. W. N. M. van Leeuwen, *Journal of the American Chemical Society*, 2001, **123**, 7630–7637.

[63] L. W. Chung, W. M. C. Sameera, R. Ramozzi, A. J. Page, M. Hatanaka, G. P. Petrova, T. V. Harris, X. Li, Z. Ke, F. Liu, H.-B. Li, L. Ding, and K. Morokuma, *Chemical Reviews*, 2015, **115**, 5678–5796.

[64] R. Improta, F. Santoro, and L. Blancafort, *Chemical Reviews*, 2016, **116**, 3540–3593.

[65] M. Schreiber, M. R. Silva-Junior, S. P. A. Sauer, and W. Thiel, *The Journal of Chemical Physics*, 2008, **128**.

[66] K. Burke and E. K. U. Gross, in *Density Functionals: Theory and Applications: Proceedings of the Tenth Chris Engelbrecht Summer School in Theoretical Physics Held at Meerensee, near Cape Town South Africa, 19–29 January 1997*, ed. D. Joubert, Springer Berlin Heidelberg, Berlin, Heidelberg, 1998; pp. 116–146.

[67] F. Neese, *Coordination Chemistry Reviews*, 2009, **253**, 526 – 563.

[68] E. Runge and E. K. U. Gross, *Physical Review Letters*, 1984, **52**, 997–1000.

[69] C. A. Ullrich, in *Time-Dependent Density-Functional Theory: Concepts and Applications*, Oxford University Press, 2011; pp. 123–153.

[70] C. M. Marian, *Wiley Interdisciplinary Reviews: Computational Molecular Science*, 2012, **2**, 187–203.

[71] A. O. Lykhin, D. S. Kaliakin, G. E. dePolo, A. A. Kuzubov, and S. A. Varganov, *International Journal of Quantum Chemistry*, 2016, **116**, 750–761.

[72] J. N. Harvey, M. Aschi, H. Schwarz, and W. Koch, *Theoretical Chemistry Accounts*, 1998, **99**, 95–99.

[73] M. J. Bearpark, M. A. Robb, and H. B. Schlegel, *Chemical Physics Letters*, 1994, **223**, 269 – 274.

[74] G. A. Crosby and J. N. Demas, *The Journal of Physical Chemistry*, 1971, **75**, 991–1024.

[75] S. Dadashi-Silab, S. Doran, and Y. Yagci, *Chemical Reviews*, 2016, **116**, 10212–10275.

[76] C. Friedl, T. Renger, H. v. Berlepsch, K. Ludwig, M. Schmidt am Busch, and J. Megow, *The Journal of Physical Chemistry C*, 2016, **120**, 19416–19433.

[77] Q. K. Timerghazin, H. J. Carlson, C. Liang, R. E. Campbell, and A. Brown, *The Journal of Physical Chemistry B*, 2008, **112**, 2533–2541.

[78] S. Asperger, in *Chemical Kinetics and Inorganic Reaction Mechanisms*, Springer US, Boston, MA, 2003; pp. 3–103.

[79] E. Lifshittz and L. Pitaevski in *Statistical Physics;* Butterworth-Heinemann, Oxford, 1980; pp. 3–387.

[80] C. Goehry, M. Besora, and F. Maseras, *ACS Catalysis*, 2015, **5**, 2445–2451.

[81] H. Eyring, *The Journal of Chemical Physics*, 1935, **3**, 107–115.

[82] W. Braun, J. T. Herron, and D. K. Kahaner, *International Journal of Chemical Kinetics*, 1988, **20**, 51–62.

[83] C. Costentin, M. Robert, and J.-M. Saveant, *Physical Chemistry Chemical Physics*, 2010, **12**, 13061–13069.

[84] R. A. Marcus, *The Journal of Chemical Physics*, 1956, **24**, 966–978.

[85] R. A. Marcus, *Angewandte Chemie International Edition in English*, 1993, **32**, 1111–1121.

[86] M. Kuss-Petermann and O. S. Wenger, *Angewandte Chemie International Edition*, 2016, **55**, 815–819.

[87] S. Murata and M. Tachiya, *The Journal of Physical Chemistry*, 1996, **100**, 4064–4070.

[88] B. S. Brunschwig, S. Ehrenson, and N. Sutin, *Journal of the American Chemical Society*, 1984, **106**, 6858–6859.

[89] D. Escudero, *Accounts of Chemical Research*, 2016, **49**, 1816–1824.

[90] C. Narth, N. Gillet, F. Cailliez, B. Lvy, and A. de la Lande, *Accounts of Chemical Research*, 2015, **48**, 1090–1097.

[91] N. Agnihotri, *Journal of Photochemistry and Photobiology C: Photochemistry Reviews*, 2014, **18**, 18 – 31.

[92] S. Difley, L.-P. Wang, S. Yeganeh, S. R. Yost, and T. V. Voorhis, *Accounts of Chemical Research*, 2010, **43**, 995–1004.

[93] A. Migliore, S. Corni, R. Di Felice, and E. Molinari, *The Journal of Chemical Physics*, 2006, **124**.

[94] M. D. Newton, *Chemical Reviews*, 1991, **91**, 767–792.

[95] S.-J. Lee, H.-C. Chen, Z.-Q. You, K.-L. Liu, T. J. Chow, I.-C. Chen, and C.-P. Hsu, *Molecular Physics*, 2010, **108**, 2775–2789.

[96] R. Vazquez-Duhalt, S. A. Aguila, A. A. Arrocha, and M. Ayala, *ChemElectroChem*, 2014, **1**, 496–513.

[97] D. Moia, V. Vaissier, I. Lopez-Duarte, T. Torres, M. K. Nazeeruddin, B. C. O'Regan, J. Nelson, and P. R. F. Barnes, *Chemical Science*, 2014, **5**, 281–290.

[98] V. Vaissier, P. Barnes, J. Kirkpatrick, and J. Nelson, *Physical Chemistry Chemical Physics*, 2013, **15**, 4804–4814.

[99] K. Müller, C. Faeh, and F. Diederich, *Science*, 2007, **317**, 1881–1886.

[100] S. Purser, P. R. Moore, S. Swallow, and V. Gouverneur, *Chemical Society Review*, 2008, **37**, 320–330.

[101] O. A. Tomashenko and V. V. Grushin, *Chemical Reviews*, 2011, **111**, 4475–4521.

[102] A. S. K. Takeru Fuyura and T. Ritter, *Nature*, 2011, **473**, 470–477.

[103] E. J. Cho, T. D. Senecal, T. Kinzel, Y. Zhang, D. A. Watson, and S. L. Buchwald, *Science*, 2010, **328**, 1679–1681.

[104] X. Wang, L. Truesdale, and J.-Q. Yu, *Journal of the American Chemical Society*, 2010, **132**, 3648–3649.

[105] J. William R. Dolbier, *Chemical Reviews*, 1996, **96**, 1557–1584.

[106] A. Studer, *Angewandte Chemie International Edition*, 2012, **51**, 8950–8958.

[107] E. Meja and A. Togni, *ACS Catalysis*, 2012, **2**, 521–527.

[108] G. V. D. Tiers, *Journal of the American Chemical Society*, 1960, **82**, 5513–5513.

[109] B. R. Langlois, E. Laurent, and N. Roidot, *Tetrahedron Letters*, 1991, **32**, 7525 – 7528.

[110] D. A. Nagib and D. W. C. Macmillan, *Nature*, 2011, **480**, 224–228.

[111] M. Nappi, G. Bergonzini, and P. Melchiorre, *Angewandte Chemie International Edition*, 2014, **53**, 4921–4925.

[112] R. S. Mulliken, *The Journal of Physical Chemistry*, 1952, **56**, 801–822.

[113] R. Foster, *The Journal of Physical Chemistry*, 1980, **84**, 2135–2141.

[114] M. J. Frisch, G. W. Trucks, H. B. Schlegel, G. E. Scuseria, M. A. Robb, J. R. Cheeseman, G. Scalmani, V. Barone, B. Mennucci, G. A. Petersson, H. Nakatsuji, M. Caricato,

X. Li, H. P. Hratchian, A. F. Izmaylov, J. Bloino, G. Zheng, J. L. Sonnenberg, M. Hada, M. Ehara, K. Toyota, R. Fukuda, J. Hasegawa, M. Ishida, T. Nakajima, Y. Honda, O. Kitao, H. Nakai, T. Vreven, J. A. Montgomery, J. E. Peralta, F. Ogliaro, M. Bearpark, J. J. Heyd, E. Brothers, K. N. Kudin, V. N. Staroverov, R. Kobayashi, J. Normand, K. Raghavachari, A. Rendell, J. C. Burant, S. S. Iyengar, J. Tomasi, M. Cossi, N. Rega, J. M. Millam, M. Klene, J. E. Knox, J. B. Cross, V. Bakken, C. Adamo, J. Jaramillo, R. Gomperts, R. E. Stratmann, O. Yazyev, A. J. Austin, R. Cammi, C. Pomelli, J. W. Ochterski, R. L. Martin, K. Morokuma, V. G. Zakrzewski, G. A. Voth, P. Salvador, J. J. Dannenberg, S. Dapprich, A. D. Daniels, Farkas, J. B. Foresman, J. V. Ortiz, J. Cioslowski, and D. J. Fox, Gaussian 09, Revision B.01, 2009.

[115] A. Bergner, M. Dolg, W. Kchle, H. Stoll, and H. Preuss, *Molecular Physics*, 1993, **80**, 1431–1441.

[116] W. J. Hehre, R. Ditchfield, and J. A. Pople, *The Journal of Chemical Physics*, 1972, **56**, 2257–2261.

[117] R. Ditchfield, W. J. Hehre, and J. A. Pople, *The Journal of Chemical Physics*, 1971, **54**, 724–728.

[118] C. E. Check, T. O. Faust, J. M. Bailey, B. J. Wright, T. M. Gilbert, and L. S. Sunderlin, *The Journal of Physical Chemistry A*, 2001, **105**, 8111–8116.

[119] W. Braun, J. T. Herron, and D. K. Kahaner, *International Journal of Chemical Kinetics*, 1988, **20**, 51–62.

[120] L. Wojnrovits and E. Takcs, *Radiation Physics and Chemistry*, 2013, **87**, 82 – 87.

[121] D. Balcells and F. Maseras, *New Journal of Chemistry*, 2007, **31**, 333–343.

[122] H. Fischer, *Chemical Reviews*, 2001, **101**, 3581–3610.

[123] L. E. Rush, P. G. Pringle, and J. N. Harvey, *Angewandte Chemie International Edition*, 2014, **53**, 8672–8676.

[124] K. Morokuma, *The Journal of Chemical Physics*, 1971, **55**, 1236–1244.

[125] T. Ziegler and A. Rauk, *Theoretica chimica acta*, 1977, **46**, 1–10.

[126] M. v. Hopffgarten and G. Frenking, *Wiley Interdisciplinary Reviews: Computational Molecular Science*, 2012, **2**, 43–62.

[127] R. H. Crabtree, *Journal of Chemical Society, Dalton Transactions*, 2001, pp. 2437–2450.

[128] S. S. Stahl, J. A. Labinger, and J. E. Bercaw, *Angewandte Chemie*, 1998, **110**, 2298–2311.

[129] M. Lersch and M. Tilset, *Chemical Reviews*, 2005, **105**, 2471–2526.

[130] S. R. Neufeldt and M. S. Sanford, *Accounts of Chemical Research*, 2012, **45**, 936–946.

[131] L. Boisvert and K. I. Goldberg, *Accounts of Chemical Research*, 2012, **45**, 899–910.

[132] T. W. Lyons and M. S. Sanford, *Chemical Reviews*, 2010, **110**, 1147–1169.

[133] G. Bandoli, P. A. Caputo, F. P. Intini, M. F. Sivo, and G. Natile, *Journal of the American Chemical Society*, 1997, **119**, 10370–10376.

[134] D. C. Powers and T. Ritter, *Nature Chemistry*, 2009, **1**, 302–309.

[135] N. R. Deprez and M. S. Sanford, *Journal of the American Chemical Society*, 2009, **131**, 11234–11241.

[136] K. J. Bonnington, M. C. Jennings, and R. J. Puddephatt, *Organometallics*, 2008, **27**, 6521–6530.

[137] Y. Ye, N. D. Ball, J. W. Kampf, and M. S. Sanford, *Journal of the American Chemical Society*, 2010, **132**, 14682–14687.

[138] C. R. Landis, C. M. Morales, and S. S. Stahl, *Journal of the American Chemical Society*, 2004, **126**, 16302–16303.

[139] A. R. Petersen, R. A. Taylor, I. Vicente-Hernndez, P. R. Mallender, H. Olley, A. J. P. White, and G. J. P. Britovsek, *Journal of the American Chemical Society*, 2014, **136**, 14089–14099.

[140] R. Taylor, D. Law, G. Sunley, A. White, and G. Britovsek, *Angewandte Chemie International Edition*, 2009, **48**, 5900–5903.

[141] D. Zhang, L.-Z. Wu, Q.-Z. Yang, X.-H. Li, L.-P. Zhang, and C.-H. Tung, *Organic Letters*, 2003, **5**, 3221–3224.

[142] M. Selke and C. S. Foote, *Journal of the American Chemical Society*, 1993, **115**, 1166–1167.

[143] J. M. Praetorius, D. P. Allen, R. Wang, J. D. Webb, F. Grein, P. Kennepohl, and C. M. Crudden, *Journal of the American Chemical Society*, 2008, **130**, 3724–3725.

[144] G. Scalmani, M. J. Frisch, B. Mennucci, J. Tomasi, R. Cammi, and V. Barone, *The Journal of Chemical Physics*, 2006, **124**, 74504–74513.

[145] P. J. Hay and W. R. Wadt, *The Journal of Chemical Physics*, 1985, **82**, 299–310.

[146] M. R. R. Prabhath, J. Romanova, R. J. Curry, S. R. P. Silva, and P. D. Jarowski, *Angewandte Chemie International Edition*, 2015, **54**, 7949–7953.

[147] W. H. Lam, E. S.-H. Lam, and V. W.-W. Yam, *Journal of the American Chemical Society*, 2013, **135**, 15135–15143.

[148] X.-H. Li, L.-Z. Wu, L.-P. Zhang, C.-H. Tung, and C.-M. Che, *Chemical Communications*, 2001, pp. 2280–2281.

[149] F. Wilkinson, W. P. Helman, and A. B. Ross, *Journal of Physical and Chemical Reference Data*, 1995, **24**, 663–677.

[150] K. W. Bentley, *Natural Product Reports*, 2004, **21**, 395–424.

[151] K. W. Bentley, *Natural Product Reports*, 2005, **22**, 249–268.

[152] M. Somei and F. Yamada, *Natural Product Reports*, 2005, **22**, 73–103.

[153] Z. Li and C.-J. Li, *Journal of the American Chemical Society*, 2005, **127**, 6968–6969.

[154] K. R. Campos, A. Klapars, J. H. Waldman, P. G. Dormer, and C.-y. Chen, *Journal of the American Chemical Society*, 2006, **128**, 3538–3539.

[155] M. Ohta, M. Quick, J. Yamaguchi, B. Wnsch, and K. Itami, *Chemistry An Asian Journal*, 2009, **4**, 1416–1419.

[156] S. J. Pastine, D. V. Gribkov, and D. Sames, *Journal of the American Chemical Society*, 2006, **128**, 14220–14221.

[157] J. Cossy and D. Belotti, *Tetrahedron Letters*, 2006, **62**, 6459 – 6470.

[158] O. Mamoru, M. Kentaro, and T. Kazuo, *Bulletin of the Chemical Society of Japan*, 1980, **53**, 1683–1688.

[159] X. Zhang, S.-R. Yeh, S. Hong, M. Freccero, A. Albini, D. E. Falvey, and P. S. Mariano, *Journal of the American Chemical Society*, 1994, **116**, 4211–4220.

[160] J. M. R. Narayanam and C. R. J. Stephenson, *Chemical Society Reviews*, 2011, **40**, 102–113.

[161] A. Bauer, F. Westkamper, S. Grimme, and T. Bach, *Nature*, 2005, **436**, 1139–1140.

[162] N. A. Romero and D. A. Nicewicz, *Chemical Reviews*, 2016, **116**, 10075–10166.

[163] A. McNally, C. K. Prier, and D. W. C. MacMillan, *Science*, 2011, **334**, 1114–1117.

[164] T. Hofbeck and H. Yersin, *Inorganic Chemistry*, 2010, **49**, 9290–9299.

[165] T. Sajoto, P. I. Djurovich, A. B. Tamayo, J. Oxgaard, W. A. Goddard, and M. E. Thompson, *Journal of the American Chemical Society*, 2009, **131**, 9813–9822.

[166] W. Finkenzeller and H. Yersin, *Chemical Physics Letters*, 2003, **377**, 299–305.

[167] P. J. Hay, *The Journal of Physical Chemistry A*, 2002, **106**, 1634–1641.

[168] R. R. Nazmutdinov, M. D. Bronshtein, T. T. Zinkicheva, N. S. Hansen, J. Zhang, and J. Ulstrup, *Inorganic Chemistry*, 2016, **55**, 9335–9345.

[169] A. Goto, S. Sanada, L. Lei, and K. Hori, *Macromolecules*, 2016, **49**, 2511–2517.

[170] M. Bietti, G. A. DiLabio, O. Lanzalunga, and M. Salamone, *The Journal of Organic Chemistry*, 2010, **75**, 5875–5881.

[171] J. Orjala and W. H. Gerwick, *Journal of Natural Products*, 1996, **59**, 427–430.

[172] M. D. Unson, C. B. Rose, D. J. Faulkner, L. S. Brinen, J. R. Steiner, and J. Clardy, *The Journal of Organic Chemistry*, 1993, **58**, 6336–6343.

[173] W. Hofheinz and W. E. Oberhnsli, *Helvetica Chimica Acta*, 1977, **60**, 660–669.

[174] G. Helmchen and G. Wegner, *Tetrahedron Letters*, 1985, **26**, 6047 – 6050.

[175] S. E. Brantley and T. F. Molinski, *Organic Letters*, 1999, **1**, 2165–2167.

[176] S. Beaumont, E. A. Ilardi, L. R. Monroe, and A. Zakarian, *Journal of the American Chemical Society*, 2010, **132**, 1482–1483.

[177] Z. Gu and A. Zakarian, *Angewandte Chemie International Edition*, 2010, **49**, 9702–9705.

[178] Z. Gu, A. T. Herrmann, and A. Zakarian, *Angewandte Chemie International Edition*, 2011, **50**, 7136–7139.

[179] T. Amatov and U. Jahn, *Angewandte Chemie International Edition*, 2011, **50**, 4542–4544.

[180] M. Schmittel and A. Burghart, *Angewandte Chemie International Edition in English*, 1997, **36**, 2550–2589.

[181] M. N. Hopkinson, B. Sahoo, J.-L. Li, and F. Glorius, *Chemistry A European Journal*, 2014, **20**, 3874–3886.

[182] M. Neumann, S. Fldner, B. Knig, and K. Zeitler, *Angewandte Chemie International Edition*, 2011, **50**, 951–954.

[183] D. A. DiRocco and T. Rovis, *Journal of the American Chemical Society*, 2012, **134**, 8094–8097.

[184] J. Du, K. L. Skubi, D. M. Schultz, and T. P. Yoon, *Science*, 2014, **344**, 392–396.

[185] C. Mller, A. Bauer, and T. Bach, *Angewandte Chemie International Edition*, 2009, **48**, 6640–6642.

[186] R. Brimioulle and T. Bach, *Science*, 2013, **342**, 840–843.

[187] K. Zeitler, *Angewandte Chemie International Edition*, 2009, **48**, 9785–9789.

[188] C. K. Prier, D. A. Rankic, and D. W. C. MacMillan, *Chemical Reviews*, 2013, **113**, 5322–5363.

[189] P. Walsh and M. Kozlowski, *Fundamentals of Asymmetric Catalysis*, University Science Books, 2009.

[190] H. Huo, C. Wang, K. Harms, and E. Meggers, *Journal of the American Chemical Society*, 2015, **137**, 9551–9554.

[191] H. Huo, C. Fu, K. Harms, and E. Meggers, *Journal of the American Chemical Society*, 2014, **136**, 2990–2993.

[192] E. B. Bauer, *Chemical Society Reviews*, 2012, **41**, 3153–3167.

[193] D. M. Walden, O. M. Ogba, R. C. Johnston, and P. H.-Y. Cheong, *Accounts of Chemical Research*, 2016, **49**, 1279–1291.

[194] Q. Peng and R. S. Paton, *Accounts of Chemical Research*, 2016, **49**, 1042–1051.

[195] C. Liu, M. Besora, and F. Maseras, *Chemistry An Asian Journal*, 2016, **11**, 411–416.

[196] D. Balcells and F. Maseras, *New Journal of Chemistry*, 2007, **31**, 333–343.

[197] S. Grimme, *Chemistry – A European Journal*, 2012, **18**, 9955–9964.

[198] R. F. Ribeiro, A. V. Marenich, C. J. Cramer, and D. G. Truhlar, *The Journal of Physical Chemistry B*, 2011, **115**, 14556–14562.

[199] H. Huo, X. Shen, C. Wang, L. Zhang, P. Rose, L.-A. Chen, K. Harms, M. Marsch, G. Hilt, and E. Meggers, *Nature*, 2014, **515**, 100–103.

UNIVERSITAT ROVIRA I VIRGILI
A COMPUTATIONAL APPROACH TO THE MECHANISM OF LIGHT-DRIVEN REACTIONS IN SOLUTION
Victor Miguel Fernández Alvarez

UNIVERSITAT
ROVIRA i VIRGILI